AD-A156 937 INTERFEROMETRIC MEARUREMENTS OF ANOMALOUS DISPERSION IN 1/2
HYDROGEN FLUORIDE(U) AIR FORCE INST OF TECH
WRIGHT-PATTERSON AFB OH J M RABINS MAY 85
UNCLASSIFIED AFIT/CI/NR-85-3D F/G 7/4 NL

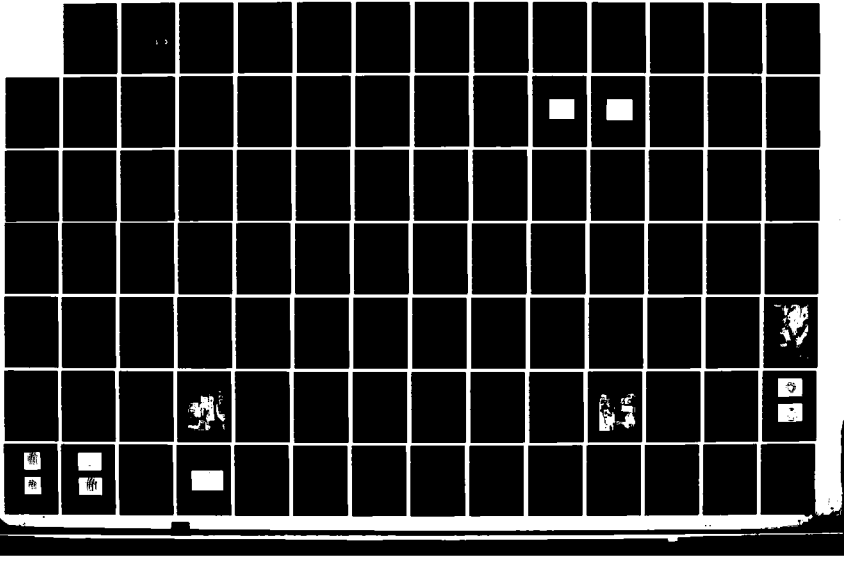

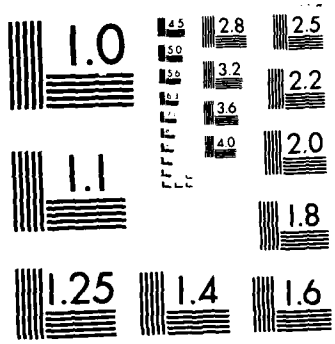

MICROCOPY RESOLUTION TEST CHART
NATIONAL BUREAU OF STANDARDS 1963 A

AD-A156 937

INTERFEROMETRIC MEASUREMENTS OF ANOMALOUS DISPERSION IN HYDROGEN FLUORIDE

BY

JOHN MICHAEL RABINS

B.S., United States Air Force Academy, 1973

M.S., Air Force Institute of Technology, 1978

DTIC
ELECTE
JUL 15 1985
S D
G

DISSERTATION

Submitted in Partial Fulfillment of the
Requirements for the Degree of

Doctor of Philosophy in Physics

The University of New Mexico
Albuquerque, New Mexico

May, 1985

DISTRIBUTION STATEMENT A
Approved for public release;
Distribution Unlimited

DTIC FILE COPY

85 06 24 095

UNCLASS

SECURITY CLASSIFICATION OF THIS PAGE (When Data Entered)

REPORT DOCUMENTATION PAGE	READ INSTRUCTIONS BEFORE COMPLETING FORM
1. REPORT NUMBER AFIT/CI/NR 85-30 AD-A156937	2 GOVT ACCESSION NO. 3 RECIPIENT'S CATALOG NUMBER
4. TITLE (and Subtitle) Interferometric Measurements Of Anomalous Dispersion In Hydrogen Fluoride	5 TYPE OF REPORT & PERIOD COVERED THESIS/DISSERTATION 6 PERFORMING ORG. REPORT NUMBER
7. AUTHOR(s) John Michael Rabins	8. CONTRACT OR GRANT NUMBER(s)
9. PERFORMING ORGANIZATION NAME AND ADDRESS AFIT STUDENT AT: The University of New Mexico	10. PROGRAM ELEMENT, PROJECT, TASK AREA & WORK UNIT NUMBERS
11. CONTROLLING OFFICE NAME AND ADDRESS AFIT/NR WPAFB OH 45433	12. REPORT DATE May 1985 13. NUMBER OF PAGES 118
14. MONITORING AGENCY NAME & ADDRESS(if different from Controlling Office)	15. SECURITY CLASS. (of this report) UNCLASS 15a. DECLASSIFICATION/DOWNGRADING SCHEDULE

16. DISTRIBUTION STATEMENT (of this Report)

APPROVED FOR PUBLIC RELEASE; DISTRIBUTION UNLIMITED

17. DISTRIBUTION STATEMENT (of the abstract entered in Block 20, if different from Report)

18. SUPPLEMENTARY NOTES

APPROVED FOR PUBLIC RELEASE: IAW AFR 190-1

14 May 85

LYNN E. WOLAVER
Dean for Research and
Professional Development
AFIT, Wright-Patterson AFB OH

19. KEY WORDS (Continue on reverse side if necessary and identify by block number)

20. ABSTRACT (Continue on reverse side if necessary and identify by block number)

ATTACHED

DD FORM 1 JAN 73 1473 EDITION OF 1 NOV 65 IS OBSOLETE

UNCLASS

SECURITY CLASSIFICATION OF THIS PAGE (When Data Entered)

INTERFEROMETRIC MEASUREMENTS OF ANOMALOUS DISPERSION IN HYDROGEN FLUORIDE

JOHN MICHAEL RABINS

B.S., Physics, United States Air Force Academy, 1973
M.S., Engineering Physics, Air Force Institute of Technology, 1978
Ph.D., Physics, University of New Mexico, 1985

Quantitative measurements of unsaturated anomalous dispersion of the $P_1(4)$ and $P_1(6)$ vibration-rotation transitions of hydrogen fluoride (HF) in absorption are reported. Contained also are measurements of the partially-saturated $P_1(4)$ transition. All measurements were obtained with an interferometric approach at pressures less than ten torr. A Fabry-Perot interferometer was used to spatially resolve the axial modes of an HF probe laser. A Michelson interferometer, one leg of which contained an HF absorption cell, imposed lines of constant phase. Fringe shifts were recorded and used to determine the refractive index change between axial mode frequencies. The unsaturated results compare favorably with computer-generated theoretical curves which account for proper amounts of pressure and Doppler broadening. A simple rate-equation model for the saturated results is proposed as an initial step in understanding the complex pressure-dependent relaxation processes occuring in this particular gas. The experimental results indicate a combined state-altering and velocity-changing collision rate of ~~11~~ 10^6/sec-torr, a value lying between the total line-broadening rate and the gas kinetic (hard sphere) rate.

INTERFEROMETRIC MEASUREMENTS OF ANOMALOUS DISPERSION IN HYDROGEN FLUORIDE

BY

JOHN MICHAEL RABINS

MAJOR, USAF

1985

118 PAGES

Ph.D.

UNIVERSITY OF NEW MEXICO

Accession For
NTIS GRA&I
DTIC TAB
Unannounced
Justification
By
Distribution/
Availability Codes
Dist | Avail and/or Special
A/1

John Michael Rabins

Candidate

Physics and Astronomy

Department

This dissertation is approved, and it is acceptable in quality and form for publication on microfilm:

Approved by the Dissertation Committee:

John C. Bellum, Chairperson

David Drummond

James G. Small

Michael Jarlik

Accepted:

Dean, Graduate School

Date

To the Lord

He reminds me often of the truth of Ecclesiastes 3:11, the foolishness of man's wisdom, and His incredible love for us, anyway.

ACKNOWLEDGMENTS

This project was accomplished with the help of a great many people. In particular, I am indebted to my advisor, Dr. David Drummond, for his expert guidance and dedication to the work. He has the gift of patience, and continued to believe in me even when I didn't. I am also grateful to those individuals at the Air Force Weapons Laboratory who gave freely of their time and energy. Tsgt Jim Blickem and Sgt Les Gragg participated in every phase of the experiment and were always there when needed. Mr. Don Vonderhaar, Lt John Coffey, Mr. Roman "Marty" Martinez, MSgt Ray Ruane, Mr. Tom Breece, Lt Nan Founds, Mr. Doug Buffett, Mr. Bruce Hayes, Mr. Norm Belt, and Mr. Harry Sauerhoff were instrumental in assembling the laser and vacuum pump facilities. Mr. Ken Bosserman machined many parts for me, and Mr. Willy Kunzler coated optics. Mr. Art Goodman and Mr. Ernie Flores did much of the photography and graphics work. Finally, I would like to thank Mr. Nick Pchelkin and Mr. Orlando Bettis for their technical assistance, and Ms. Jeanne Williams for typing the manuscript.

INTERFEROMETRIC MEASUREMENTS OF ANOMALOUS DISPERSION IN HYDROGEN FLUORIDE

BY

JOHN MICHAEL RABINS

ABSTRACT OF DISSERTATION

Submitted in Partial Fulfillment of the
Requirements for the Degree of

Doctor of Philosophy in Physics

The University of New Mexico
Albuquerque, New Mexico

May, 1985

INTERFEROMETRIC MEASUREMENTS OF ANOMALOUS DISPERSION IN HYDROGEN FLUORIDE

JOHN MICHAEL RABINS

B.S., Physics, United States Air Force Academy, 1973
M.S., Engineering Physics, Air Force Institute of Technology, 1978
Ph.D., Physics, University of New Mexico, 1985

Quantitative measurements of unsaturated anomalous dispersion of the $P_1(4)$ and $P_1(6)$ vibration-rotation transitions of hydrogen fluoride (HF) in absorption are reported. Contained also are measurements of the partially-saturated $P_1(4)$ transition. All measurements were obtained with an interferometric approach at pressures less than ten torr. A Fabry-Perot interferometer was used to spatially resolve the axial modes of an HF probe laser. A Michelson interferometer, one leg of which contained an HF absorption cell, imposed lines of constant phase. Fringe shifts were recorded and used to determine the refractive index change between axial mode frequencies. The unsaturated results compare favorably with computer-generated theoretical curves which account for proper amounts of pressure and Doppler broadening. A simple rate-equation model for the saturated results is proposed as an initial step in understanding the complex pressure-dependent relaxation processes occuring in this particular gas. The experimental results indicate a combined state-altering and velocity-changing collision rate of 11×10^6/sec-torr, a value lying between the total line-broadening rate and the gas kinetic (hard sphere) rate.

TABLE OF CONTENTS

		Page
	LIST OF ILLUSTRATIONS	x
	LIST OF TABLES	xiii
1.	INTRODUCTION	1
2.	THEORETICAL CONSIDERATIONS	9
	The Concept of Absorption	9
	The Einstein Theory of Radiation	9
	The Classical Electron Oscillator	15
	The Absorption Coefficient	17
	Broadening Mechanisms and the Absorption Coefficient	17
	Correcting the Population Density	22
	Saturation and the Absorption Coefficient	24
	The Index of Refraction	30
	The Effect of Broadening on the Refractive Index	32
3.	MODELING THE THEORY BY COMPUTER	35
	Calculating k_0	35
	Modeling the Unsaturated Absorption Coefficient	36
	Modeling the Saturated Absorption Coefficient	39
	Modeling the Index of Refraction	42
	The Index Difference Between Modes	43
4.	EXPERIMENTAL APPARATUS	50
	The Laser	50
	Experimental Layout for Unsaturated Measurements	55
	Experimental Layout for Saturated Measurements	61
	Fringe Visualization Technique	64
5.	EXPERIMENTAL RESULTS	69
	Data Reduction	69

TABLE OF CONTENTS--Continued.

	Page
Determining the Mode Spacing	71
Calculating the Mode Pulling	71
Measuring Mode Spacing From the Fabry-Perot Pattern	82
Measuring Mode Spacing by Beats	87
Determining the Saturation Intensity	87
6. DISCUSSION	92
Experimental Limitations	93
CONCLUSION	99
APPENDIX A: COMPUTER PRINTOUT	100
APPENDIX B: FABRY-PEROT INTERFEROMETER MOUNT	111
APPENDIX C: TABULAR DATA	114
REFERENCES	116

LIST OF ILLUSTRATIONS

Figure		Page
1	Typical Anomalous Dispersion Curve for Gain Medium	2
2	Spatially Resolved Axial Modes	7
3	Superimposed Fabry-Perot and Michelson Interference Patterns	8
4	Intensity Profile	10
5	An Absorption Line	11
6	Typical Rotational-Vibrational Spectrum for Diatomic Molecule	23
7	A Simple Saturation Model	25
8	Absorption Line Response to a Saturating Signal	28
9	The Broadened Absorption Curve	34
10	Computer-Generated Absorption Profile.....	38
11	Computer Model for Saturated Absorption Line	40
12	Computer-Generated Index of Refraction for Pure Doppler Broadening	44
13	Computer-Generated Index of Refraction for Combined Broadening	45
14	Saturated Absorption and Index of Refraction Curves for 75 cm Cavity ($K = \pi\Delta\nu_H = 113\times10^6$/sec-torr).....	46
15	Saturated Absorption and Index of Refraction Curves for 75 cm Cavity ($K = \pi\Delta\nu_H/10 = 11\times10^6$/sec-torr).....	47
16	Saturated Absorption and Index of Refraction Curves for 75 cm Cavity (K = Gas Kinetic = 3×10^6/sec-torr).....	48
17	Theoretical Doppler and Combined Broadening Curves for 47.3 cm Cavity	49

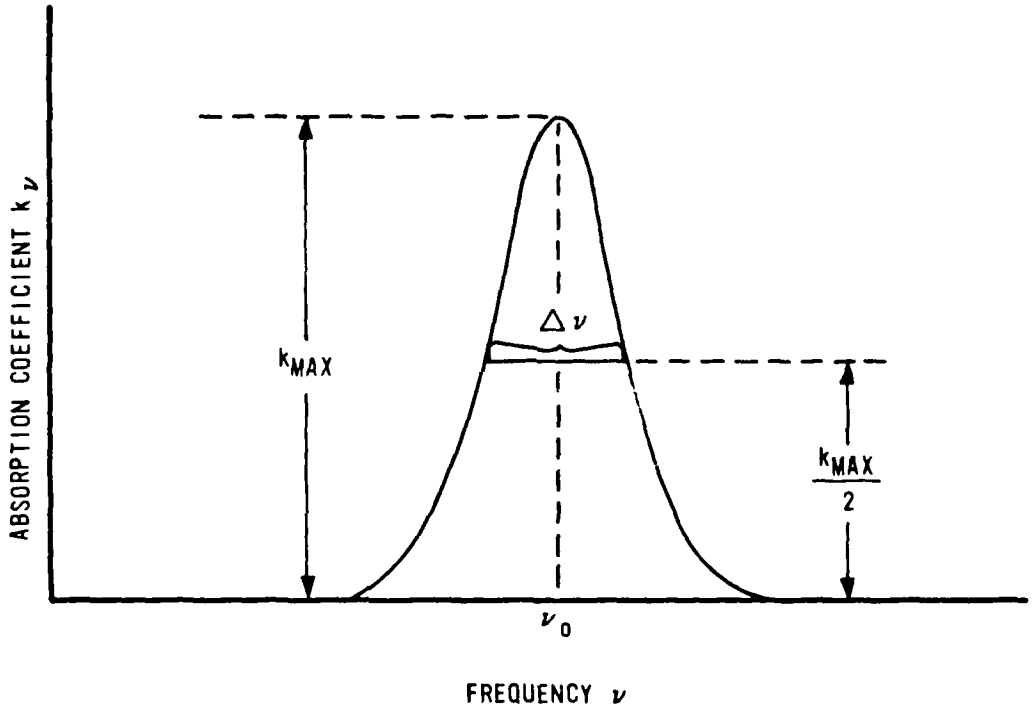

Figure 5. An Absorption Line

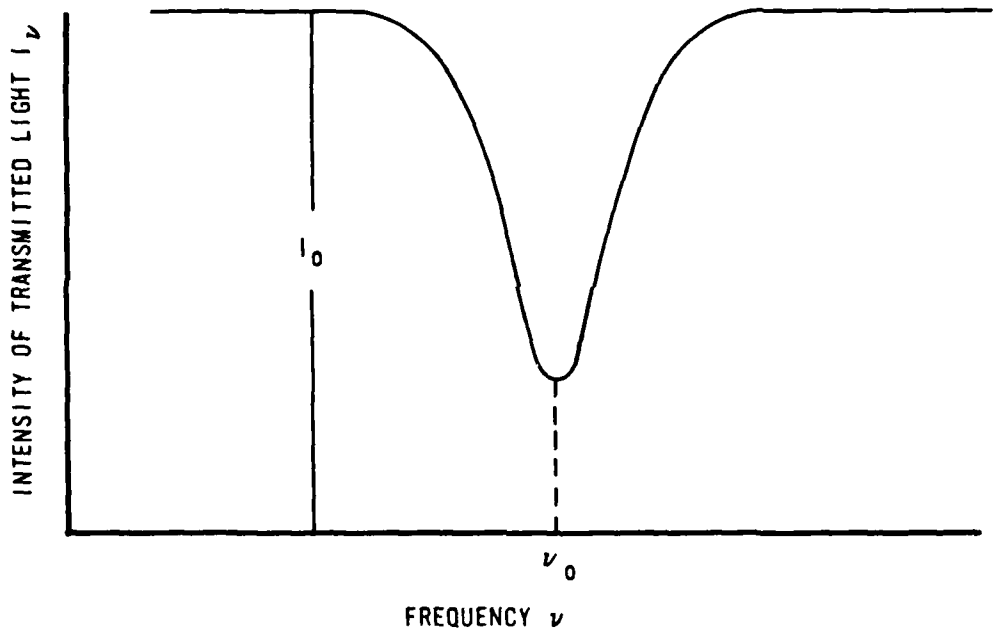

Figure 4. Intensity Profile

CHAPTER 2

THEORETICAL CONSIDERATIONS

The Concept of Absorption

An absorption line at frequency ν_0 exists when a curve such as that pictured in Fig. 4 results from an actual absorption measurement, which is made by recording the intensity of light transmitted through a known thickness x of material while monitoring the frequency of the incident light (whose intensity remains constant). The absorption coefficient k_ν is then defined by

$$I_\nu = I_0 e^{-k_\nu x}, \tag{2.1}$$

where I_ν and I_0 are respectively the transmitted and incident intensities. Typically k_ν is measured in cm^{-1} while x is measured in cm. From Eq. (2.1) we may obtain k_ν, which graphs like the curve shown in Fig. 5. The quantity $\Delta\nu$ (typically called the halfwidth or linewidth) represents the width of the curve at its half peak value. Generally the absorption coefficient is represented as a function of k_{max} and $\Delta\nu$, and depends primarily on the nature of the gas molecules, their motion, and their mutual interaction (Mitchell and Zemansky, 1971).

The Einstein Theory of Radiation

We first picture a box containing two-level molecules and isotropic radiation (of intensity I_ν and frequency in the range ν to

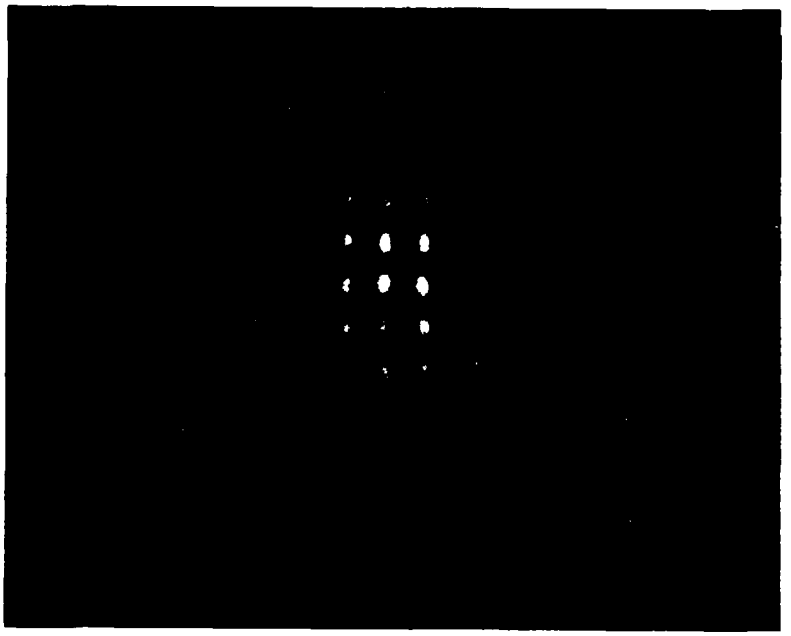

Figure 3. Superimposed Fabry-Perot and Michelson Interference Patterns

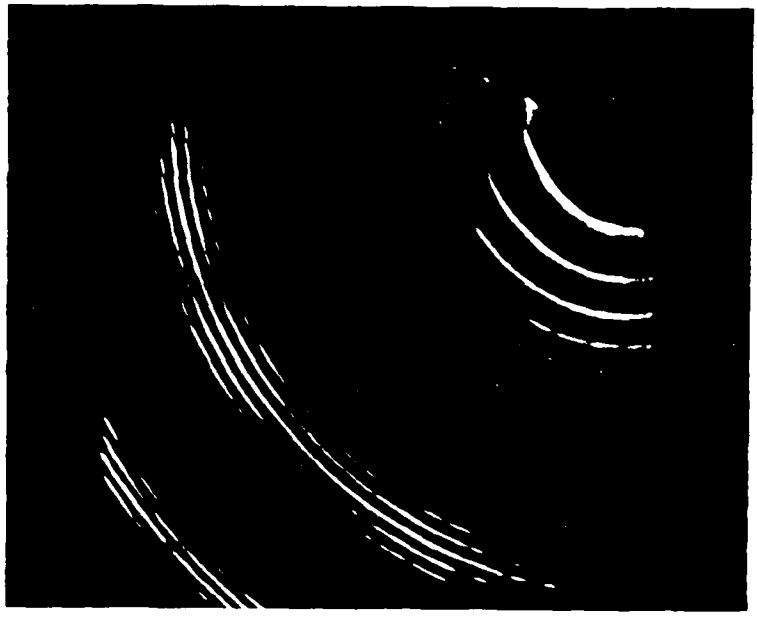

Figure 2. Spatially Resolved Axial Modes

headaches connected with random noise. Thus, ideally, at any instant of time, the only variable experienced by any frequency data point (in this case an axial mode) is the difference in refractive index. Also, the number of points on the dispersion curve that can be sampled at any instant is limited only by the number of axial modes generated by the probe laser.

Initially we tried to see anomalous dispersion in neon on the visible transition. The Fabry-Perot pattern (Fig. 2) showed about five axial modes from a Spectra Physics Model 124 laser. The Michelson interferometer imposed lines of constant phase, as seen in Fig. 3. Since neon lases between two excited states, we used a capacitative discharge to populate the lower lasing level. The discharge generated observable absorption for a time on the order of a millisecond, but also, unfortunately, caused two problems beyond our ability to solve easily. First, it created uneven spatial heating of the gas, causing beam steering. Second, the noise of the discharge light completely masked the crossed-interference pattern from view.

We thus abandoned neon and proceeded with HF, a gas with lasing transitions to the ground vibrational state. While we had a different set of problems to contend with (see Chaps. 4 and 6), we nevertheless showed the technique to work in absorption, even under saturation. There is no reason that it cannot be used successfully for a saturated gain medium as well. In principle, this technique offers perhaps the only available method for viewing the time-evolution of the refractive index in a pulsed laser.

report that, "it proved impossible to extract meaningful dispersion profiles as a function of frequency from the relatively high noise produced by the amplifier medium (Gross and Coffer, 1983)."

Drummond (1982) measured the refractive index of HF with a similar arrangement. Using an incandescent light, a quarter-meter monochromator, and a Mach-Zehnder interferometer (one leg of which contained a gas cell), he measured the fringe shifts due to changes in gas pressure. He was thus able to construct some of the most accurate experimental dispersion profiles available for HF between 2.5 μm and 2.9 μm. The resolution was not fine enough, though, to give meaningful data over the linewidth of an absorption line.

Of course, the linewidth of a transition is precisely where the axial laser modes fall. This paper describes a new technique in which saturated anomalous dispersion in absorption has been measured. It has the potential of measuring saturated anomalous dispersion in a gain medium as well. While somewhat similar to the Aerospace technique described above (we use a Michelson interferometer instead of a Mach-Zehnder), it differs in two significant regards. First, the HF laser cavity is made long enough to allow more than one axial mode to oscillate, thereby eliminating the need to scan through the gain. Second, these axial modes are separated <u>spatially</u> by a Fabry-Perot interferometer, enabling us to view them all at one instant of time. Therein lies an obvious advantage over the other techniques used to date. Whereas they all have employed a time-resolution format, we do not. By resolving spatially, this technique eliminates some of the

able to determine experimentally the anomalous dispersion profile in order to provide answers for some of the far-reaching questions.

There have been a number of successful attempts to see anomalous dispersion experimentally. Since the variation of refractive index can be calculated from the gain profile, measuring the gain profile with a probe laser provides an indirect measurement. Direct measurements have been made by:

1. Observing the mode-pulling effect and beat signal between two axial modes (Chodzko, Chang, and Mirels, 1978; Wang, 1976; Wang and Varwig, 1979a,b).

2. Measuring the beam steering that results from anomalous dispersion with a sensitive wavefront sensor, a Brewster's angle absorption cell, and a frequency-stable, frequency-scannable HF chemical laser (Wang and Varwig, 1981).

3. Interferometric techniques which are described below.

A group at Aerospace Corporation (Gross, et al., 1979) has measured anomalous dispersion in absorption with a Mach-Zehnder interferometer illuminated by a single-line, single-mode, frequency-scanned CW HF probe laser. The absorbing gas, contained in an absorption cell, was placed in one arm of the interferometer. As the probe laser was scanned in frequency across the transition, the interferometric fringes shifted their positions in proportion to the change in the refractive index. The anomalous dispersion could then be determined. Their ultimate goal of measuring anomalous dispersion in a saturated gain medium could not be met with this technique, however. In fact, they

Complicating matters is the fact that a medium subjected to a high-intensity laser beam will saturate in a manner dependent on many factors. These include the intensity and frequency of the saturating beam as well as the various collision and relaxation processes within the medium. For a predominantly Doppler-broadened medium, the laser beam will burn a hole into the gain profile at its own frequency but will leave the refractive index value there essentially unaltered. If there are many axial modes, as is true for the long cavities of high-power HF chemical lasers, the complex interaction of the modes with the gain will naturally affect the entire curve, and the entire gain curve can be depressed by saturation fairly uniformly, or homogeneously, even when pressure broadening is not significant. This kind of gain reduction implies a flattening of the refractive index curve, and we can thus see how, in a well-saturated HF laser, phase distortions might be unimportant (Gross, et al., 1979).

The general theory of saturated anomalous dispersion has been addressed by a number of authors (including Bennett, Jr., 1962a,b; Siegman, 1971). Booth and Troup (1969) have presented a nice treatment of the wavefront distortion caused by non-uniform saturated anomalous dispersion in laser amplifiers. They looked at a homogeneously broadened transition with a Lorentz line shape. Little theory exists, however, for the complex saturation processes in a continuous-wave (CW) chemical laser (Mirels, 1979, offers one such theory for an HF laser). It is even more difficult to get a theoretical grasp of the changing anomalous dispersion in a pulsed laser. Thus, it is important to be

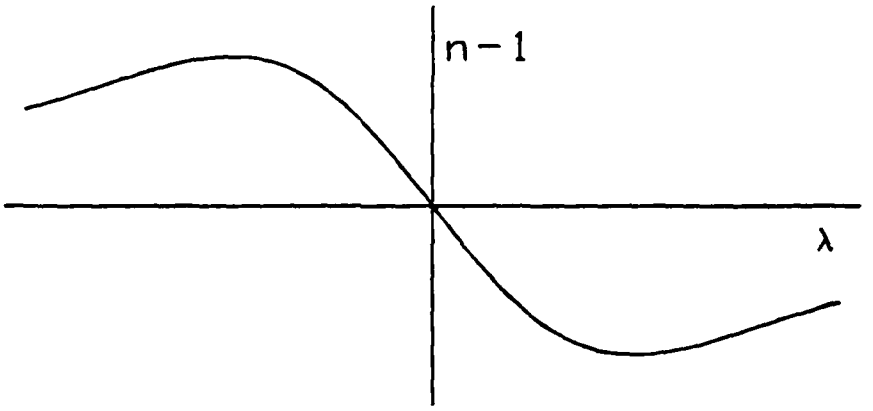

Figure 1. Typical Anomalous Dispersion Curve for Gain Medium

CHAPTER 1

INTRODUCTION

The refractive index of the gain medium is an important consideration in designing a gas laser with good beam quality. Temporal and spatial inhomogeneities of the medium can affect the wave fronts and, if serious enough, destroy the coherence of the beam. Even with perfect temporal and spatial uniformity, however, there exists around a lasing line an anomalous dispersion that places an ultimate limit on beam quality.

Figure 1 shows a typical anomalous dispersion profile for an unsaturated gain medium. As can be seen, the refractive index falls precipitously through the emission line. If we neglect saturation effects, this variation in index is large enough in a typical laser to destroy the coherence between axial modes of a single transition in just one round trip through the cavity. As an example, let us take a hydrogen fluoride (HF) laser of wavelength 2.7 μm, with a 10 cm gain-medium length (ℓ), and with two axial modes which "see" a difference in refractive index (Δn) of 10^{-5}. Then, the phase change between the two modes in one round trip is

$$\Delta\phi = \frac{2\pi}{\lambda}(2\ell)\Delta n \cong 1.5\pi \ , \tag{1.1}$$

or three-quarters of a wave.

LIST OF TABLES

Table		Page
1	Calculated k_0' Values	36
2	Laser Lines and Powers	54
3	Theoretical Mode-Pulling Corrections	82
4	Fabry-Perot Mode-Spacing Measurements	86

LIST OF ILLUSTRATIONS--Continued.

Figure		Page
37	Theoretical and Experimental Saturated Results for $P_1(4)$ Line, 75 cm Cavity	79
38	Fabry-Perot Pattern	83
39	Fabry-Perot Interferometer	84
40	Spectrum Analyzer Calibration	88
41	Beat Measurements for $P_1(4)$ Line	89
42	Intensity Profiles for $P_1(4)$ Line	91
43	Improperly Coated Fabry-Perot Plates	96
44	Close-up Photograph of Fabry-Perot Mount	112
45	Blueprint of Fabry-Perot Mount	113

LIST OF ILLUSTRATIONS--Continued.

Figure		Page
18	Laser Cavity with Zero-Order Grating Coupler	51
19	The Laser	52
20	Optical Diagnostics for Unsaturated Measurements	56
21	Optical Diagnostics Diagram for Unsaturated Measurements ..	57
22	Relative Orientation of Brewster Windows and Michelson Beam Splitter	59
23	Gas Cell Construction	60
24	Optical Diagnostics Diagram for Saturated Measurements	62
25	Optical Diagnostics for Saturated Measurements	63
26	Axially-Symmetric View of Combined Interference Pattern ...	66
27	Off-Axis View of Combined Interference Pattern	67
28	Modes of Unequal Intensity	68
29	Data Point Prepared for Measuring Fringe Shift	70
30	Theoretical and Experimental Unsaturated Results for $P_1(4)$ Line, 47.3 cm Cavity	72
31	Theoretical and Experimental Unsaturated Results for $P_1(4)$ Line, 75 cm Cavity	73
32	Theoretical and Experimental Unsaturated Results for $P_1(4)$ Line, 87 cm Cavity	74
33	Theoretical and Experimental Unsaturated Results for $P_1(6)$ Line, 47.3 cm Cavity	75
34	Theoretical and Experimental Unsaturated Results for $P_1(6)$ Line, 75 cm Cavity	76
35	Theoretical and Experimental Unsaturated Results for $P_1(6)$ Line, 87 cm Cavity	77
36	Theoretical and Experimental Saturated Results for $P_1(4)$ Line, 47.3 cm Cavity.....	78

$\nu + d\nu$) which is capable of causing molecular transitions between the ground state 1 and the excited state 2. We can then define the Einstein A and B coefficients as follows:

$B_{12}I_\nu$ is the probability per second that a molecule in state 1, exposed to isotropic radiation of intensity I_ν and frequency in the range ν to $\nu + d\nu$, will absorb a photon of energy $h\nu$ and make a transition to state 2.

A_{21} is the probability per second that an excited molecule will spontaneously emit (in any direction) a photon of energy $h\nu$ and make a transition to the ground state.

$B_{21}I_\nu$ is the probability per second that an excited molecule will undergo transition to state 1 when exposed to isotropic radiation of intensity I_ν and frequency between ν and $\nu + d\nu$, thereby emitting a photon of energy $h\nu$ in the same direction as the incoming photon.

By considering a state of thermodynamic equilibrium, Einstein derived the functional relationships

$$\frac{A_{21}}{B_{12}} = \frac{2h\nu^3}{c^2}\frac{g_1}{g_2}, \tag{2.2}$$

$$\frac{B_{21}}{B_{12}} = \frac{g_1}{g_2}, \tag{2.3}$$

where g_1 and g_2 are the statistical weights (degeneracies) of the two states. Also,

$$A_{21} = \frac{1}{\tau} \quad , \tag{2.4}$$

where τ is a measure of the lifetime of the atom in the excited state.

It should be noted that this section parallels the treatment given by Mitchell and Zemansky (1971). Hence, the B coefficients are defined in terms of intensity, as compared with the original B coefficients which were defined in terms of energy density. The relation between the two is

$$B(\text{density}) = \frac{c}{4\pi} B(\text{intensity}) \quad . \tag{2.5}$$

Now we consider a parallel beam of light of intensity I_ν and frequency in the range ν to $\nu + d\nu$ traversing a layer of molecules bounded by x and x + dx. Suppose there are N molecules/cm^3 in level 1, of which δN_ν are capable of absorbing light in the frequency range ν to $\nu + d\nu$, and N' molecules/cm^3 in level 2, of which $\delta N'_\nu$ are capable of emitting light in this range. Then the decrease in beam energy is

$$-d[I_\nu \delta\nu] = \delta N_\nu dx \, h\nu B_{12} \frac{I_\nu}{4\pi} - \delta N' dx \, h\nu B_{21} \frac{I_\nu}{4\pi} \quad , \tag{2.6}$$

where we have ignored the comparatively small contribution offered by the noncoherent spontaneous emission (Lengyel, 1971). If we rewrite the last equation as

$$-\frac{1}{I_\nu}\frac{dI_\nu}{dx}\,\delta\nu = \frac{h\nu}{4\pi}\,(B_{12}\delta N_\nu - B_{21}\delta N'_\nu)\ , \tag{2.7}$$

we see immediately that the left-hand side is simply $k_\nu\delta\nu$ as defined by Eq. (2.1). Integrating over all frequencies, while treating ν as constant over the region of significant absorption, yields

$$\int_0^\infty k_\nu d\nu = \frac{h\nu_0}{4\pi}\,(B_{12}N - B_{21}N')\ , \tag{2.8}$$

where ν_0 is the center-line frequency. Finally, using the Einstein relations, Eqs. (2.2), (2.3), and (2.4), gives

$$\int_0^\infty k_\nu d\nu = \frac{\lambda_0^2 g_2}{8\pi g_1}\,NA\left(1 - \frac{g_1}{g_2}\frac{N'}{N}\right)\ , \tag{2.9}$$

where we have replaced A_{21} by A. For gases in which the upper-level population is small compared with the lower, i.e., $N'/N \ll 1$, we may write Eq. (2.9) as

$$\int_0^\infty k_\nu d\nu = \frac{\lambda_0^2 g_2}{8\pi g_1}\,NA\ . \tag{2.10}$$

This very important equation tells us that, regardless of the processes contributing to the formation of an absorption line, the total integrated absorption remains constant for a fixed number density N.

The Classical Electron Oscillator

We take a simple gas model in which there is negligible interaction between molecules and assume a driving electromagnetic field induces a dipole moment in each gas molecule by virtue of electron displacement, but leaves the nuclear position essentially unaffected. Thus, each molecule can be thought of as an electron on a spring with an equation of motion (in one dimension)

$$\ddot{x} + \gamma\dot{x} + \omega_0^2 x = -\frac{e}{m} E_0 e^{-i\omega t} , \tag{2.11}$$

where ω_0 represents the natural resonance frequency and the damping term $\gamma\dot{x}$ arises because of radiation damping. γ represents the natural radiative damping rate and is proportional to the inverse of the excited state's lifetime. For justification of the simple form of the damping term, the reader is referred to the treatment given by Jackson (1975) or Marion (1965).

The solution to Eq. (2.11) is

$$x = \frac{(-e/m)E_0}{(\omega_0^2 - \omega^2) - i\gamma\omega} e^{-i\omega t} , \tag{2.12}$$

and so the dipole moment resulting from the displacement of each electron is

$$p = -ex = \frac{(e^2/m)}{(\omega_0^2 - \omega^2) - i\gamma\omega} E_0 e^{-i\omega t} . \tag{2.13}$$

If N represents the molecular number density, then the total dipole moment per unit volume (polarization) is simply

$$\mathbf{P} = N\mathbf{p} = \frac{N(e^2/m)}{(\omega_0^2 - \omega^2) - i\gamma\omega} E_0 e^{-i\omega t} \quad . \tag{2.14}$$

But

$$\mathbf{P} = \hat{\chi}_e \mathbf{E}, \tag{2.15}$$

where $\hat{\chi}_e$ is the complex electric susceptibility, and the dielectric constant is

$$\hat{\varepsilon} = 1 + 4\pi\hat{\chi}_e. \tag{2.16}$$

Thus

$$\hat{\varepsilon} = 1 + 4\pi \frac{N(e^2/m)}{(\omega_0^2 - \omega^2) - i\gamma\omega} \quad . \tag{2.17}$$

Since the dielectric constant for a gas is close to one, we may write

$$\sqrt{\hat{\varepsilon}} \cong 1 + 2\pi \frac{N(e^2/m)}{(\omega_0^2 - \omega^2) - i\gamma\omega} \quad . \tag{2.18}$$

This equation may be separated into real and imaginary parts, yielding

$$\sqrt{\hat{\varepsilon}} \cong 1 + 2\pi \frac{(\omega_0^2 - \omega^2)N(e^2/m)}{(\omega_0^2 - \omega^2)^2 + \gamma^2\omega^2} + i2\pi \frac{N\gamma\omega(e^2/m)}{(\omega_0^2 - \omega^2)^2 + \gamma^2\omega^2} \quad . \tag{2.19}$$

The Absorption Coefficient

The absorption coefficient κ_ν is proportional to the imaginary part of Eq. (2.19), and since

$$\omega_0^2 - \omega^2 = (\omega_0 + \omega)(\omega_0 - \omega) \cong 2\omega(\omega_0 - \omega) \ , \tag{2.20}$$

we can write

$$k_\nu \propto \frac{\gamma\omega}{[2\omega(\omega_0 - \omega)]^2 + \gamma^2\omega^2} = \left(\frac{1}{\gamma\omega}\right) \frac{1}{1 + [2(\omega - \omega_0)/\gamma]^2} \ . \tag{2.21}$$

With the exception of the difference term, we may treat ω as constant throughout the absorption line. Hence,

$$k_\nu \propto \frac{1}{1 + [2(\omega - \omega_0)/\gamma]^2} = \frac{1}{1 + [2(\nu - \nu_0)/\Delta\nu_N]^2} \ , \tag{2.22}$$

where the natural width $\Delta\nu_N$ is related to the Einstein A coefficient by

$$\Delta\nu_N = \frac{1}{2\pi\tau} = \frac{A}{2\pi} \ . \tag{2.23}$$

Broadening Mechanisms and the Absorption Coefficient

So far we have been concerned only with natural broadening of the absorption line due to the finite radiative lifetime of the excited state. There are, however, other processes that contribute to the formation of the line, two of which are relevant to the problem at hand: Doppler broadening and pressure broadening. Doppler broadening arises from the random thermal motion of the gas molecules, which implies a

shift in the resonance frequency of each velocity group. Thus, the Doppler-broadened response is proportional to a Maxwellian (Gaussian) distribution, and if other broadening mechanisms are neglected, the absorption coefficient is given by the familiar expression

$$k_\nu = k_0 \, e^{-[2(\nu - \nu_0)\sqrt{\ln 2}/\Delta\nu_D]^2} \quad , \tag{2.24}$$

where $\Delta\nu_D$ is the Doppler linewidth, depending on the absolute temperature T and the molecular mass M according to

$$\Delta\nu_D = \frac{2\sqrt{2k\ln 2}}{c} \nu_0 \sqrt{\frac{T}{M}} \quad , \tag{2.25}$$

and k_ν represents the maximum absorption coefficient if only Doppler broadening exists. We can calculate k_0 by first integrating Eq. (2.24), getting

$$\int_0^\infty k_\nu \, d\nu = \frac{1}{2}\sqrt{\frac{\pi}{\ln 2}} \, k_0 \Delta\nu_D \quad . \tag{2.26}$$

But we know that

$$\int_0^\infty k_\nu \, d\nu = \frac{\lambda_0^2 g_2}{8\pi g_1} A N \quad . \tag{2.10}$$

So

$$k_0 = \frac{2}{\Delta\nu_D}\sqrt{\frac{\ln 2}{\pi}} \frac{\lambda_0^2 g_2}{8\pi g_1} A N \quad . \tag{2.27}$$

Pressure broadening of the absorption line stems from random collisions of radiating molecules which interrupt (or dephase) the resonant response. Lorentz treated the effect of collisions on the absorbing and emitting characteristics of the classical electron oscillator in a manner similar to that of radiation damping (Lorentz, 1915). He found the expression for the absorption coefficient of a gas with pure pressure broadening to be of the same form as Eq. (2.22), namely

$$k_\nu \propto \frac{1}{1 + [2(\nu - \nu_0)/\Delta\nu_p]^2} \quad , \tag{2.28}$$

where $\Delta\nu_p$ is the pressure-broadened linewidth, given by

$$\Delta\nu_p = \frac{1}{\pi}\left(\begin{array}{c}\text{number of broadening collisions} \\ \text{per second per absorbing molecule}\end{array}\right) \quad . \tag{2.29}$$

Pressure and lifetime broadening differ from Doppler broadening (and other inhomogeneous broadening mechanisms) in that each molecule contributes equally, or homogeneously, to the absorption curve. We may write the absorption coefficient for homogeneous broadening as

$$k_\nu \propto \frac{1}{1 + [2(\nu - \nu_0)/\Delta\nu_H]^2} \quad , \tag{2.30}$$

where the contributing homogeneous linewidths are summed to give $\Delta\nu_H$.

The pressure-broadened linewidth of the fundamental transition $(v = 1,J') \leftrightarrow (v = 0,J'')$ is given by

$$\Delta\nu_P = \frac{N\bar{v}}{\pi c} \sum_J \rho_J \sigma_J \quad , \tag{2.31}$$

where N is the density of perturbing molecules at one atmosphere pressure, $\bar{v}$ is the mean relative collision velocity, ρ_J is the population distribution of a perturbing molecule's rotational states, and σ_J is the collision cross section for each rotational state J of the perturbing molecule. The cross section σ_J is expressed in terms of the development of the interaction in time, and contains the details of the collision, such as the impact parameter and the interaction potential. For a gas in rotational equilibrium, the population distribution is given by

$$\rho_J = \frac{(2J + 1)e^{-E_J/kT}}{\sum_J (2J + 1)e^{-E_J/kT}} \quad . \tag{2.32}$$

Tsao and Curnette (1963) amplified upon a theory developed by Anderson (1949) for calculating σ_J. This theory involved detailed quantum-mechanical calculations of the probabilities of nonradiative transitions caused by the combined effects of all intermolecular forces in the system. There have been many calculations for the broadening of HF which incorporate this theory (Benedict, et al., 1956a,b; Emanuel, et al., 1971; Meredith, 1972; Meredith, 1973; Meredith and Smith, 1973). These calculations differed in the form used for the interaction potential and the collision trajectories. They nevertheless showed generally good agreement with experimental results for cases in which

long-range dipole-dipole forces are dominant, such as for HF self-broadening (Hough, 1977).

Since the three broadening mechanisms are independent of one another, the combined absorption coefficient of a gas can be calculated in one of two ways. First, we may consider every infinitesimal frequency band of the homogeneously broadened curve to be Doppler broadened. We do this by selecting some frequency band at a distance $\nu - \nu_0$ from the center of a pure homogeneously-broadened line. Then we represent the Doppler broadening of this band at a distance δ from $\nu - \nu_0$ and integrate over δ. Another way of saying the same thing is that we write the Lorentzian response of a single Doppler-shifted molecule, multiply by the number of molecules having that particular shift, and then sum over all possible shifts. The result is

$$k_\nu \propto \int_{-\infty}^{\infty} \frac{e^{-[2\delta\sqrt{\ln 2}/\Delta\nu_D]^2}}{1 + [2(\nu - \nu_0 - \delta)/\Delta\nu_H]^2} \, d\delta \, . \tag{2.33}$$

The second way of calculating the combined absorption coefficient is to consider every infinitesimal frequency band of the pure Doppler curve to be Lorentzian broadened, or

$$k_\nu \propto \int_{-\infty}^{\infty} \frac{e^{-[2(\nu - \nu_0 - \delta)\sqrt{\ln 2}/\Delta\nu_D]^2}}{1 + (2\delta/\Delta\nu_H)^2} \, d\delta \, . \tag{2.34}$$

The constant of proportionality is determined by Eqs. (2.10) and (2.26) to be $2k_0/\pi\Delta\nu_H$ for either representation of the absorption coefficient.

Correcting the Population Density

We know from Eq. (2.27) that k_0 involves N, the number density of the lower level. We must now reckon with the fact that HF is a diatomic molecule whose energy structure includes a tightly spaced [$0(10\ cm^{-1})$] rotational manifold within each vibrational level (see Fig. 6). So although essentially all of the total population is in the v = 0 vibrational level for a gas in thermal equilibrium at room temperature, the same cannot be said of the constituent rotational (J) levels. In fact, they are populated according to

$$N_J = \frac{N}{Q_r} (2J + 1) e^{-BJ(J + 1)hc/kT} , \tag{2.35}$$

where N now represents the total number density, (2J + 1) is the lower level degeneracy g_2, B is the rotational constant, and Q_r is the rotational state sum

$$Q_r = 1 + 3e^{-2Bhc/kT} + 5e^{-6Bhc/kT} + \ldots . \tag{2.36}$$

Thus k_0 should be written

$$k_0 = \frac{2}{\Delta\nu_D}\sqrt{\frac{\ln 2}{\pi}}\,\frac{\lambda_0^2 g_2}{8\pi g_1} N_J A \tag{2.37}$$

$$= \frac{\sqrt{\ln 2}}{4\pi^{3/2}}\,\frac{\lambda_0^2 g_2 NA}{\Delta\nu_D Q_r} e^{-BJ(J + 1)hc/kT} .$$

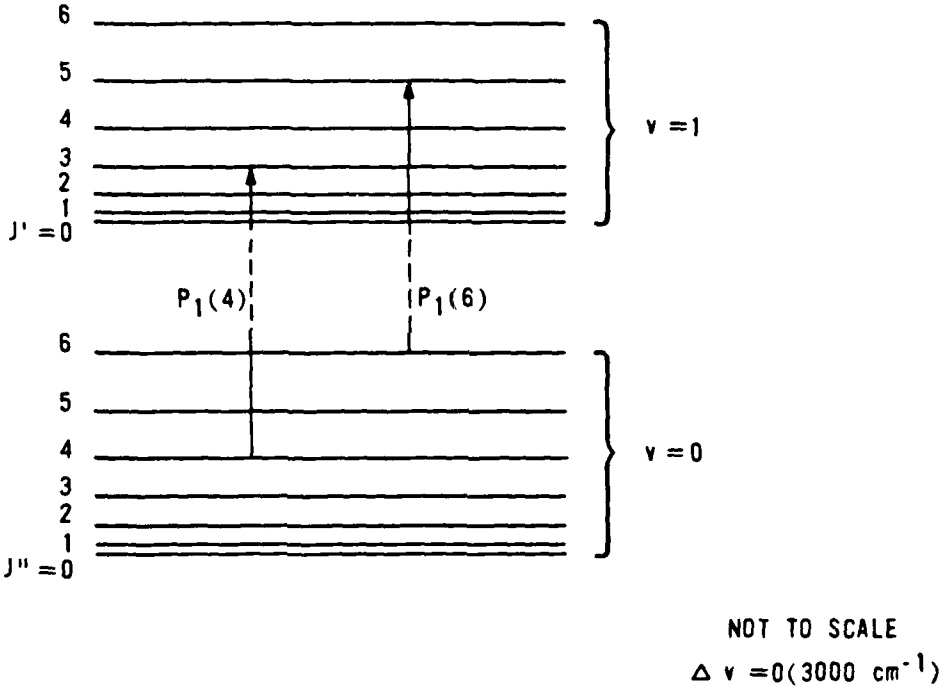

Figure 6. Typical Rotational-Vibrational Spectrum For Diatomic Molecule

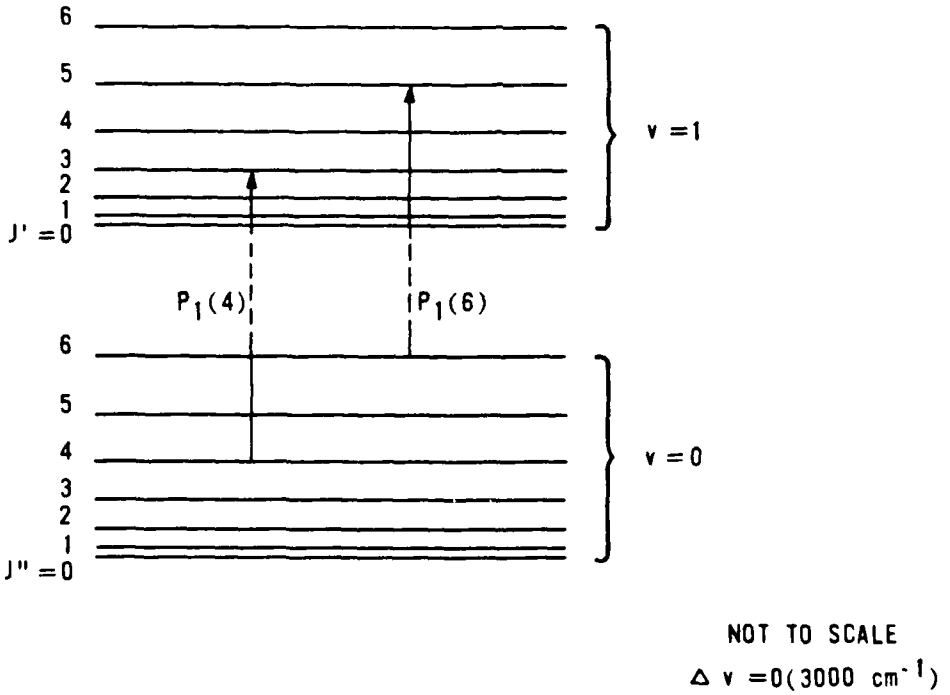

Figure 6. Typical Rotational-Vibrational Spectrum for Diatomic Molecule

Saturation and the Absorption Coefficient

The expression for the broadened absorption coefficient [Eq. (2.34)] contains k_0, the height of the pure Doppler curve at line center. Up to this point we have assumed negligible upper-level population, which is why k_0 contains the term N_J, the total lower-level population density. When the upper-level population cannot be ignored, however, as in the case of saturation, we must replace N_J by the more appropriate $N_L[1 - (g_L/g_U)(N_U/N_L)]$, where N_L and N_U are the respective population densities of the lower and upper states. To adequately model a system such as we have is an extremely complicated task, and beyond the scope of this investigation. The reason, of course, is the large number of cross-relaxational transitions that must be considered if accurate population densities are expected. What follows is a very simple model that serves as a logical beginning.

Consider a two-level system as shown in Fig. 7, where

$$\left.\begin{aligned} N_L^0 &= \text{number density in lower state with no flux,} \\ N_L &= \text{number density in lower state with flux,} \\ N_U &= \text{number density in upper state,} \\ \sigma_A &= \text{small-signal absorption cross section,} \\ \sigma_{SE} &= \text{small-signal stimulated emission cross section } [(g_L/g_U)\sigma_A], \text{ and} \\ K &= \text{state-altering and velocity-changing collision rate.} \end{aligned}\right\} \quad (2.38)$$

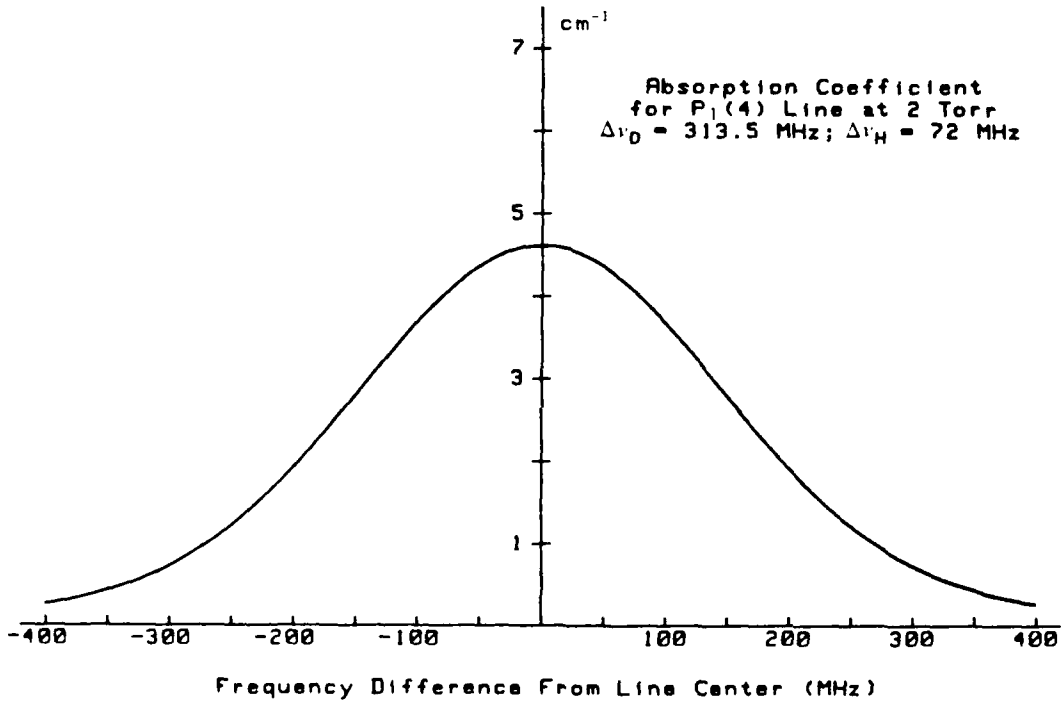

Figure 10. Computer-Generated Absorption Profile

$$k_\nu = \frac{2k_0}{\pi\Delta\nu_H} \sum_{-3000}^{3000} \frac{e^{-[2X\sqrt{\ln 2}/\Delta\nu_D]^2}}{1 + [2(V-X)/\Delta\nu_H]^2} \Delta X \quad , \tag{3.5}$$

where $V \equiv \nu - \nu_0$ represented the frequency distance from line center, and X was a variable distance from ν_0. We decided to use Eq. (2.34) instead of Eq. (2.33) for two reasons. First, it converged faster; about half the computer time was necessary. Second, saturation theory is more manageable when we build a Doppler curve with many Lorentzians, as opposed to the opposite case. We selected a step size ΔX of 5 MHz and a range of absorption values large enough to include over 98% of the theoretically predicted area under the curve. The range over which the sum was taken (3000 MHz on either side of line center) was made to match the range of absorption values.

A considerable body of experimental data exists regarding the widths of self-broadened lines in the v(1 - 0) band of HF (Meredith, 1972). Hough (1977) presents a graphic summary of these measured linewidths, in addition to the closely-matching theoretical values (see Chap. 2). It was from these measured values that we selected $\Delta\nu_H$ to be 36 MHz/torr for the $P_1(4)$ line and 14 MHz/torr for the $P_1(6)$ line.

Figure 10 is an example of an absorption profile generated with this program. Note that, even though only 400 MHz on each side of line center is displayed in the graph, a full 3000 MHz on each side was calculated and stored for later use in computing the index of refraction. We computed and stored absorption files for pressures ranging from .5 torr to 5 torr for the $P_1(4)$ line, and from .5 torr to 5 torr for the $P_1(6)$ line.

$$k_0 = 1.22\times10^{15} \frac{\lambda_0^2 p A g_2}{Q_r \Delta\nu_D} e^{-BJ(J+1)hc/kT} \quad . \tag{3.3}$$

We note that, at higher pressures (>10 torr), the presence of dimers would adversely affect the validity of the ideal gas law. For pressures below 5 torr, however, the dimer influence is small. Dividing by the pressure, we obtained the absorption per torr

$$k_0' = \frac{k_0}{P} = 1.22\times10^{15} \frac{\lambda_0^2 A g_2}{Q_r \Delta\nu_D} e^{-BJ(J+1)hc/kT} \quad . \tag{3.4}$$

Table 1 contains the calculated k_0' values for both the $P_1(4)$ and $P_1(6)$ lines at $T = 297^\circ K$, as well as values for the various components of Eq. (3.4). We used Herzberg's (1950) value for the rotational constant B and Emanuel's (1971) calculated A coefficients.

Table 1. Calculated k_0' Values

Line	λ_0 (μm)	$\Delta\nu_D$ (MHz)	A(sec^{-1})	Q_r	B(cm^{-1})	k_0'(cm^{-1}-$torr^{-1}$)
$P_1(4)$	2.64	313.58	116.00	10.20	20.94	2.83
$P_1(6)$	2.71	305.73	113.18	10.20	20.94	.50

Modeling the Unsaturated Absorption Coefficient

Now that we had found k_0, tailoring Eq. (3.1) to the computer was simply a matter of writing the integral as a truncated sum

CHAPTER 3

MODELING THE THEORY BY COMPUTER

We used a Hewlett Packard Series 200 (Model 16) Personal Computer and Model 7470A Plotter to numerically integrate and plot the theoretical expressions for the absorption coefficient

$$k_\nu = \frac{2k_0}{\pi\Delta\nu_H}\int_{-\infty}^{\infty}\frac{e^{-[2(\nu - \nu_0 - \delta)\sqrt{\ln 2}/\Delta\nu_D]^2}}{1 + (2\delta/\Delta\nu_H)^2}\,d\delta \qquad (3.1)$$

and the refractive index

$$n - 1 = \frac{\lambda_0}{4\pi}\int_0^{\infty}\frac{k_{\nu'}\,d\nu'}{\nu' - \nu}\,. \qquad (3.2)$$

Appendix A contains a listing of the computer programs.

Calculating k_0

Common to both expressions above (although buried in the second) is k_0, the peak absorption if Doppler broadening alone is present. We found this absorption coefficient by starting with

$$k_0 = \frac{\sqrt{\ln 2}\,\lambda_0^2 g_2 NA}{4\pi^{3/2}\Delta\nu_D Q_r}\,e^{-BJ(J+1)hc/kT}\,, \qquad (2.37)$$

and then writing this in terms of pressure (at $T = 297°K$) by using the ideal gas law, yielding

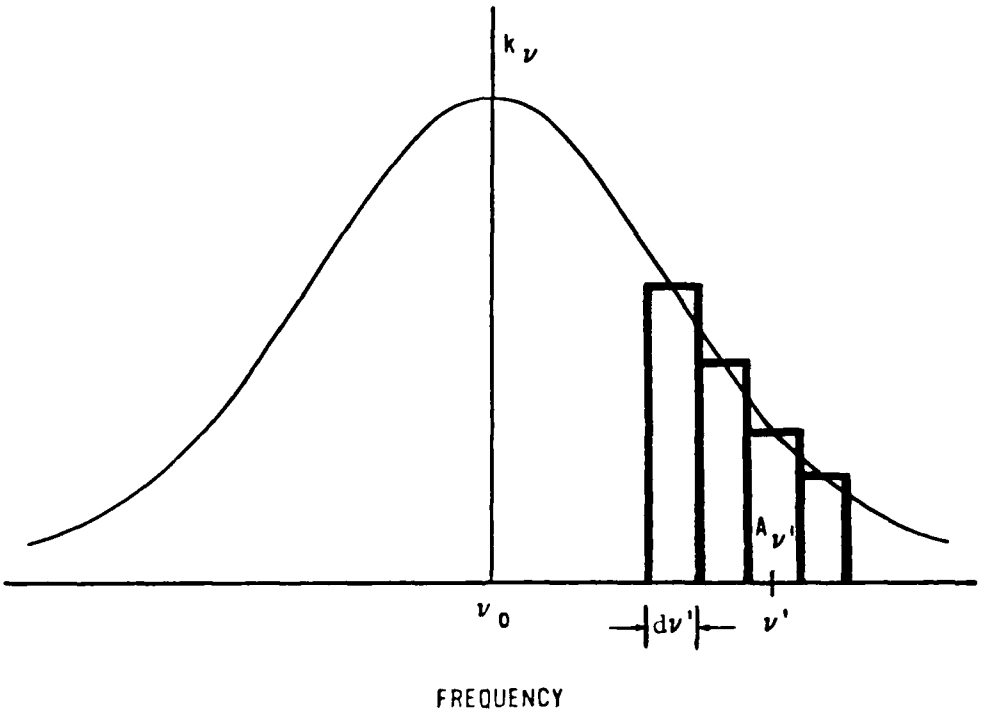

Figure 9. The Broadened Absorption Curve

$$n - 1 = \frac{\lambda_0}{4\pi} \int_0^\infty \frac{k_{\nu'} d\nu'}{\nu' - \nu} \, . \tag{2.59}$$

This expression can now be used to compute the broadened index curve.

The Effect of Broadening on the Refractive Index

Now we wish to account for the broadening of the absorption curve. To do so, we partition the absorption curve as shown in Fig. 9 and designate an A coefficient to each section according to

$$A_{\nu'} = A \frac{k_{\nu'} d\nu'}{\text{total area}} = A \frac{k_{\nu'} d\nu'}{\int_0^\infty k_\nu d\nu} \quad . \tag{2.56}$$

The index of refraction is constructed, then, by writing Eq. (2.55) as an integral over all ν'

$$n - 1 = \frac{N_J A}{32\pi^3 \int_0^\infty k_\nu d\nu} \frac{g_2}{g_1} \lambda_0^3 \int_0^\infty \frac{k_{\nu'} d\nu'}{\nu' - \nu} \, , \tag{2.57}$$

where we have removed the λ_0^3 term from the integral as essentially constant throughout the line. Using Eq. (2.26) for the area under the curve

$$\int_0^\infty k_\nu d\nu = \frac{1}{2}\sqrt{\frac{\pi}{\ln 2}}\, k_0 \Delta\nu_D \, , \tag{2.26}$$

we may write

$$n - 1 = \frac{N_J A \sqrt{\ln 2}}{16\pi^{3/2} k_0 \Delta\nu_D} \frac{g_2}{g_1} \lambda_0^3 \int_0^\infty \frac{k_{\nu'} d\nu'}{\nu' - \nu} \, , \tag{2.58}$$

which simplifies to

$$n - 1 = \frac{e^2}{2\pi mc^2} \sum_{j=0}^{\infty} \sum_{k=0}^{\infty} \frac{\lambda^2 \lambda_{kj}^2}{\lambda^2 - \lambda_{kj}^2} N_j f_{kj} \left[1 - \frac{N_k}{N_j} \frac{g_j}{g_k} \right] , \tag{2.53}$$

which was derived from Kramer's quantum-theoretical dispersion formula. Here, the sum is over all possible transitions $k \leftrightarrow j$, where k and j are the upper and lower states, respectively. g_k and g_j are the statistical weights and N_k and N_j are the number densities of the two states, while λ_{kj} is the wavelength emitted/absorbed by the transition. The oscillator strength f_{kj} can be thought of as a measure of the actual transitional response in relation to the response of a classical electron oscillator of the same frequency. It relates to the Einstein A coefficient by

$$f_{kj} = \frac{mc\lambda_{kj}^2}{8\pi^2 e^2} \frac{g_k}{g_j} A_{kj} \quad . \tag{2.54}$$

For wavelengths near an absorption line of a nonexcited gas at room temperature, we may ignore the contribution of all other absorption lines to the index and thus write

$$n - 1 = \frac{e^2 N_J f}{2\pi mc^2} \frac{\lambda^2 \lambda_0^2}{\lambda^2 - \lambda_0^2} , \tag{2.55}$$

where unnecessary subscripts have been dropped and λ_0 is the wavelength of the transition. With the exception of the oscillator strength, Eq. (2.55) is identical to Eq. (2.52).

$$\sigma_A = \frac{\frac{1}{2}\sqrt{\frac{\pi}{\ln 2}}\, k_0 \Delta\nu_D}{N_L^0 d\nu} \frac{1}{1 + [2(\nu - \nu_s)/\Delta\nu_H]^2} \quad . \tag{2.49}$$

The population dN_U and dN_L at frequency ν may now be found using Eqs. (2.41) and (2.42), after which, the effective k_0 value at ν, $k_0(\text{eff})$, follows from Eq. (2.45). This value is then used in Eq. (2.34).

The Index of Refraction

The real part of Eq. (2.19) represents the refractive index

$$n \cong 1 + 2\pi \frac{(\omega_0^2 - \omega^2) N_J (e^2/m)}{(\omega_0^2 - \omega^2)^2 + \gamma^2\omega^2} \quad . \tag{2.50}$$

Typically, the damping term in the denominator is small and, in the near infrared, may be neglected for frequencies on the order of 10 MHz or more from line center. Thus,

$$n \cong 1 + 2\pi \frac{N_J (e^2/m)}{\omega_0^2 - \omega^2} \quad , \tag{2.51}$$

or, in terms of wavelength,

$$n \cong 1 + \frac{N_J e^2}{2\pi m c^2} \frac{\lambda^2 \lambda_0^2}{\lambda^2 - \lambda_0^2} \quad . \tag{2.52}$$

This expession bears a strong resemblance to Ladenburg's (1928)

We may thus think of each velocity group as having an effective k_0 depending on the degree its Lorentzian saturates

$$k_0(\text{eff}) = k_0 \frac{dN_L[1 - (g_1/g_2)(dN_U/dN_L)]}{dN_L^0} , \tag{2.45}$$

where dN_L, dN_U, and dN_L^0 are differential population densities for the frequency band ν to $\nu + d\nu$. At frequency ν,

$$dN_L^0 = N_L^0 \frac{d\nu}{\int_0^\infty k_\nu d\nu} k_0 e^{-[2(\nu - \nu_0)\sqrt{\ln 2}/\Delta\nu_D]^2} . \tag{2.46}$$

The small-signal absorption at ν_s offered by the Lorentzian centered at ν is just

$$\alpha = \frac{k_0 e^{-[2(\nu - \nu_0)\sqrt{\ln 2}/\Delta\nu_D]^2}}{1 + [2(\nu - \nu_s)/\Delta\nu_H]^2} , \tag{2.47}$$

and the absorption cross section may be written

$$\sigma_A = \frac{\alpha}{dN_L^0} = \frac{\int_0^\infty k_\nu d\nu}{N_L^0 d\nu} \frac{1}{1 + [2(\nu - \nu_s)/\Delta\nu_H]^2} , \tag{2.48}$$

or

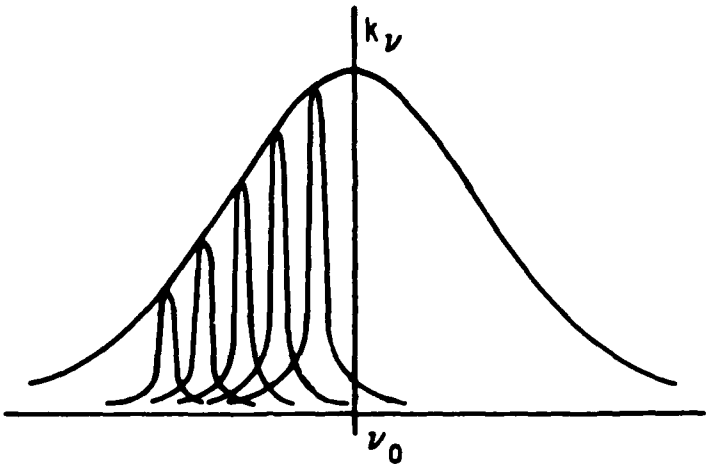

a.

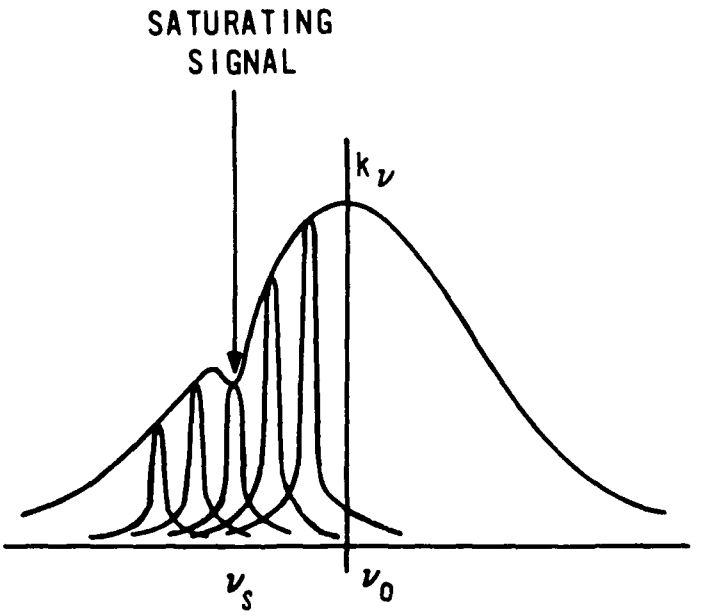

b.

Figure 8. Absorption Line Response to a Saturating Signal

a. Without Saturating Signal
b. With Saturating Signal

$$N_L = \frac{N_L^0[\sigma_{SE}/\sigma_A + Kh\nu/\sigma_A I]}{1 + \sigma_{SE}/\sigma_A + Kh\nu/\sigma_A I} = N_L^0 - N_U \quad . \tag{2.42}$$

These results make sense in the limits of very low intensity and very high intensity. For $\sigma_A I << Kh\nu$,

$$N_U \rightarrow \frac{N_L^0}{Kh\nu/\sigma_A I} = \frac{\sigma_A I}{Kh\nu} N_L^0 \quad . \tag{2.43}$$

The upper-level density is directly proportional to the intensity and inversely proportional to the collisional rate K. For $\sigma_A I >> Kh\nu$,

$$N_U \rightarrow \frac{N_L^0}{1 + \sigma_{SE}/\sigma_A} = \frac{1}{2} N_L^0 \tag{2.44}$$

if the levels have the same statistical weights.

Now consider Fig. 8a, in which we think of the broadened absorption line as being composed of many Lorentzian lines. Each Lorentzian may be thought to represent a particular velocity group (or population). A saturating signal at ν_s will interact strongly with those velocity groups having significant absorption at that frequency. Hence, for low pressures, at which the Lorentzian widths are small, each Lorentzian will depress according to the absorption it affords the saturating signal, and a hole will be burned in the overall response curve (Fig. 8b).

We represent the rate out of the lower state as $N_L \sigma_A I/h\nu$ for photon collisions and KN_L for molecular collisions, and the rate into the lower state as $N_U \sigma_{SE} I/h\nu$ for photon collisions and KN_L^0 for molecular collisions. We have assumed the lower-level activation rate to be unaffected by a small saturating signal, hence the N_L^0 term in the lower-level collision rate.

The rate into the upper state is $N_L \sigma_A I/h\nu$ for photon collisions and 0 for molecular collisions. Finally, the rate out of the upper state is written as $N_U \sigma_{SE} I/h\nu$ for photon collisions and KN_U for molecular collisions. Note that we assume the same collisional rate K for both levels.

In steady state, the rates into and out of the upper state are equal

$$N_L \sigma_A I/h\nu = N_U \sigma_{SE} I/h\nu + KN_U, \tag{2.39}$$

as are the rates into and out of the lower level

$$N_L \sigma_A I/h\nu + KN_L = N_U \sigma_{SE} I/h\nu + KN_L^0. \tag{2.40}$$

We may solve these two equations for N_U and N_L, yielding

$$N_U = \frac{N_L^0}{1 + \sigma_{SE}/\sigma_A + Kh\nu/\sigma_A I} \tag{2.41}$$

and

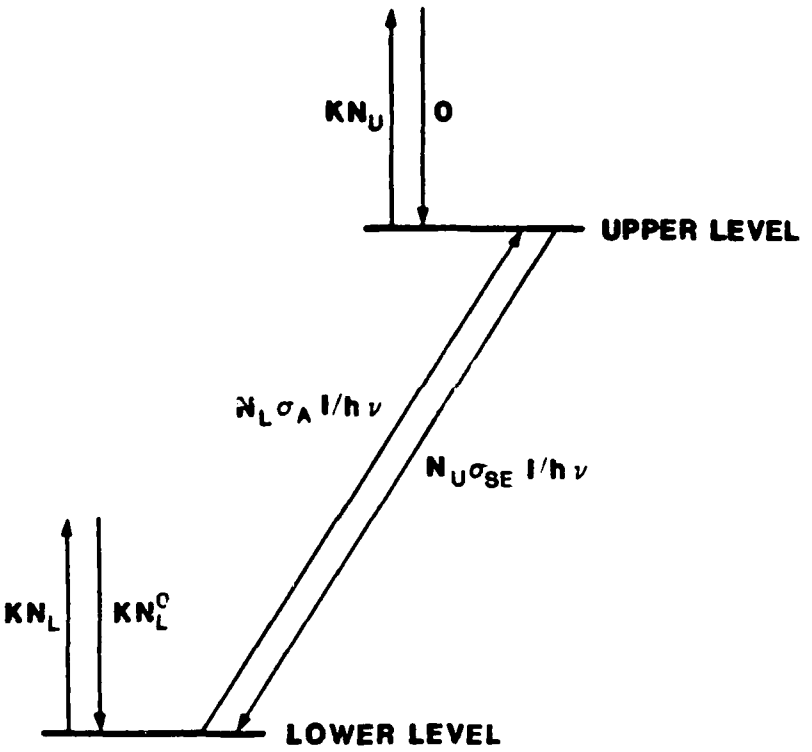

Figure 7. A Simple Saturation Model

Modeling the Saturated Absorption Coefficient

Equation (3.1) was used to model the saturated absorption line with one change: k_0 was replaced by a computed $k_0(\text{eff})$ for each frequency X. The step size ΔX again was 5 MHz. To compute $k_0(\text{eff})$ at a particular value of X we did the following (see Fig. 11):

1. First, we used Eq. (2.46) to determine the unsaturated population density corresponding to the velocity group centered at X

$$\Delta N_L^0 = N_L^0 \frac{k_0 e^{-[2X\sqrt{\ln 2}/\Delta\nu_D]^2}}{\frac{1}{2}\sqrt{\frac{\pi}{\ln 2}}\, k_0 \Delta\nu_D} \Delta X$$
$$= 5.63\times10^{13} p e^{-(.0053X)^2}, \tag{3.6}$$

where the appropriate parameters were substituted and the pressure p was measured in torr.

2. The small-signal absorption cross section (by that velocity group) for each mode was found according to

$$\alpha_{A1} = \frac{k_0 e^{-[2X\sqrt{\ln 2}/\Delta\nu_D]^2}}{1 + [2(X - S_1)/\Delta\nu_H]^2} \frac{1}{\Delta N_L^0}, \tag{3.7}$$

$$\alpha_{A2} = \frac{k_0 e^{-[2X\sqrt{\ln 2}/\Delta\nu_D]^2}}{1 + [2(X - S_2)/\Delta\nu_H]^2} \frac{1}{\Delta N_L^0}. \tag{3.8}$$

If each mode burned only one hole in the curve, then the total absorption cross section for the velocity group at X would be found by adding Eqs. (3.7) and (3.8)

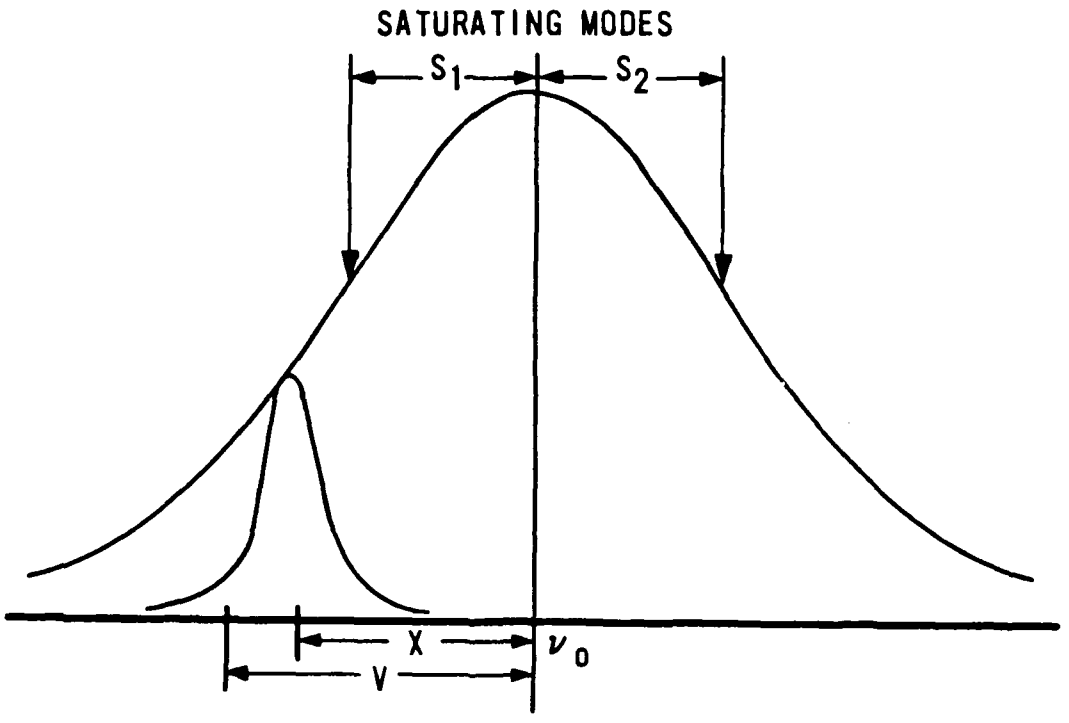

Figure 11. Computer Model for Saturated Absorption Line

$$\sigma_A = \sigma_{A1} + \sigma_{A2} \quad . \tag{3.9}$$

Since we saturated the transition in a Michelson interferometer, however, each mode affected two velocity groups. Thus, we wrote

$$\sigma_A = 2(\sigma_{A1} + \sigma_{A2}) \quad , \tag{3.10}$$

where we neglected the small amount of absorption on the first pass through the gas cell.

3. Then ΔN_U was determined from Eq. (2.41),

$$\Delta N_U = \frac{\Delta N_L^0}{1 + \sigma_{SE}/\sigma_A + Kh\nu/\sigma_A I} \quad , \tag{3.11}$$

where I represented the average intensity of the two modes. The modes were assumed to be of equal intensity.

We used three different values for K, the combined state-altering and velocity-changing collision rate. The first corresponded to the total line broadening, which, for the $P_1(4)$ line, is

$$K = \pi \Delta\nu_H \cong 113 \times 10^6/\text{sec-torr.} \tag{3.12}$$

We expected that this value might be high since it includes all phase-changing collisions. So we selected as our second value

$$K = \pi \Delta\nu_H/10 \cong 11 \times 10^6/\text{sec-torr.} \tag{3.13}$$

The third value for K was a gas kinetic (hard sphere) rate which was calculated as follows. The nuclear separation in the HF molecule was determined from the rotational constant to be .917 Å. This distance was added to the covalent radii of hydrogen (.32 Å) and fluorine (.72 Å) to give an approximate molecular diameter of 1.96 Å. This, then, yielded a cross section of

$$\sigma_0 = \pi d^2 = 1.2\times10^{-15}\ \text{cm}^2. \tag{3.14}$$

For an average relative velocity between molecules

$$\bar{v} = 7.5\times10^{4}\ \text{cm/sec}\ , \tag{3.15}$$

and number density per torr

$$N/p = 3.25\times10^{16}/\text{cm}^3\text{-torr}, \tag{3.16}$$

we found the gas kinetic collision rate to be

$$K = \bar{v}\sigma_0 N/p \cong 3\times10^{6}/\text{sec-torr}. \tag{3.17}$$

4. Finally, k_0 (eff) was found by using

$$k_0(\text{eff}) = k_0 \frac{\Delta N_L[1 - (g_1/g_u)(\Delta N_u/\Delta N_L)]}{\Delta N_L^0}\ . \tag{3.18}$$

Modeling the Index of Refraction

To determine the refractive index corresponding to a particular absorption profile, we rewrote the integral in Eq. (3.2) as a sum

$$n(V) - 1 = \frac{\lambda_0}{4\pi} \sum_{-3000}^{3000} \frac{k_X \Delta X}{X - V} \quad , \tag{3.19}$$

where V and X were defined as before. ΔX was set at 5 MHz.

For each pressure of interest, we computed two index of refraction curves. One was simply the curve obtained from an unsaturated Doppler-broadened line, where

$$k_X = k_0 e^{-[2X\sqrt{\ln 2}/\Delta\nu_D]^2} \quad . \tag{3.20}$$

The other was the curve derived from the files created with Eq. (3.12). A representative example of each is contained in Figs. 12 and 13. Figures 14-16 contain comparative absorption and dispersion profiles for the three different collision rates used in the saturation model.

The Index Difference Between Modes

The frequency difference between modes was determined to be 290 MHz, 190 MHz, and 160 MHz for the three different cavity lengths (see Chap. 5). So, to figure the difference in refractive index between two modes of equal intensity for the shortest cavity, for example, we simply doubled the index value at 145 MHz from line center. This was then plotted against pressure to give a curve such as that displayed in Fig. 17. The computed curves for the different transitions and cavity lengths are contained in Chap. 5 along with the experimental results.

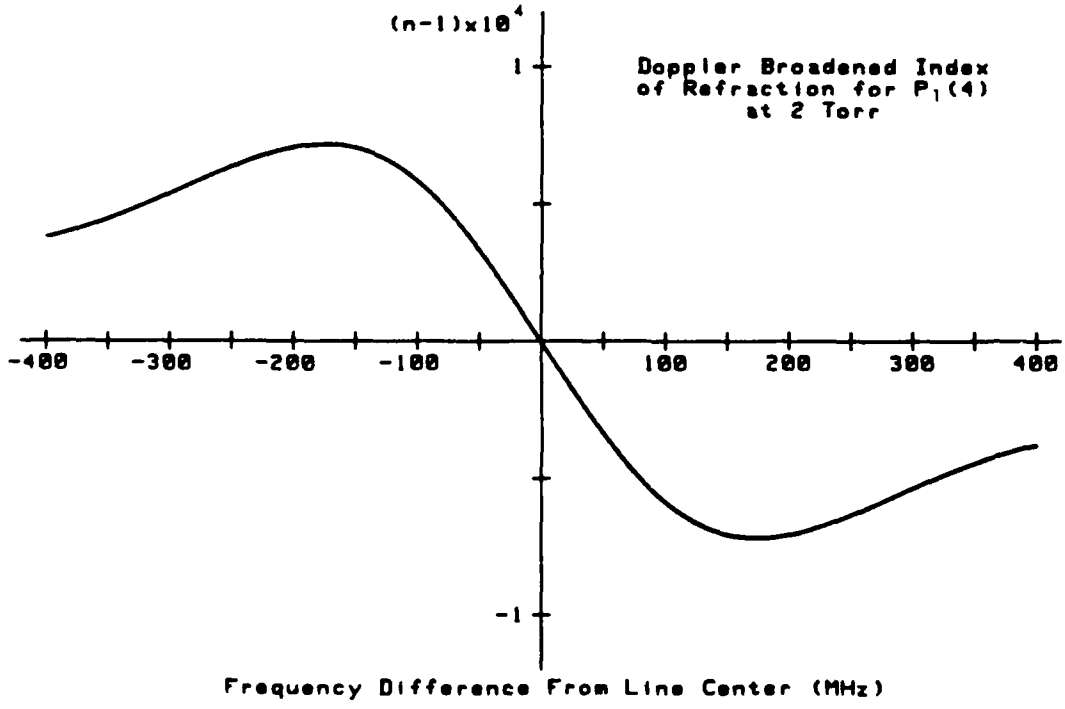

Figure 12. Computer-Generated Index of Refraction for Pure Doppler Broadening

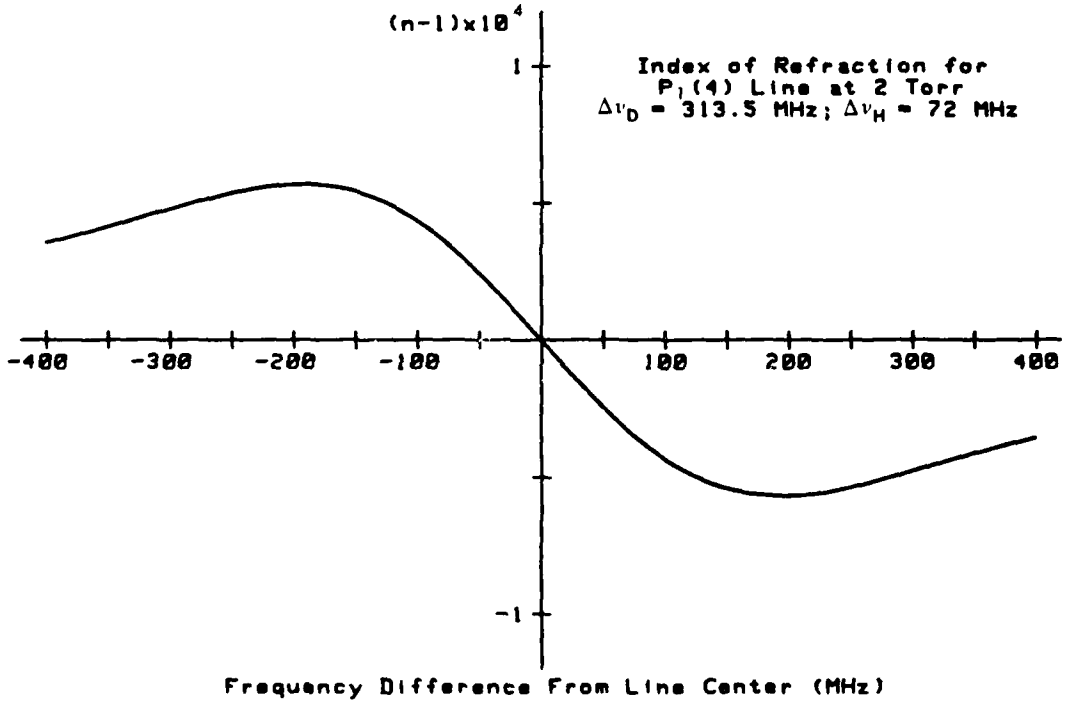

Figure 13. Computer-Generated Index of Refraction for Combined Broadening

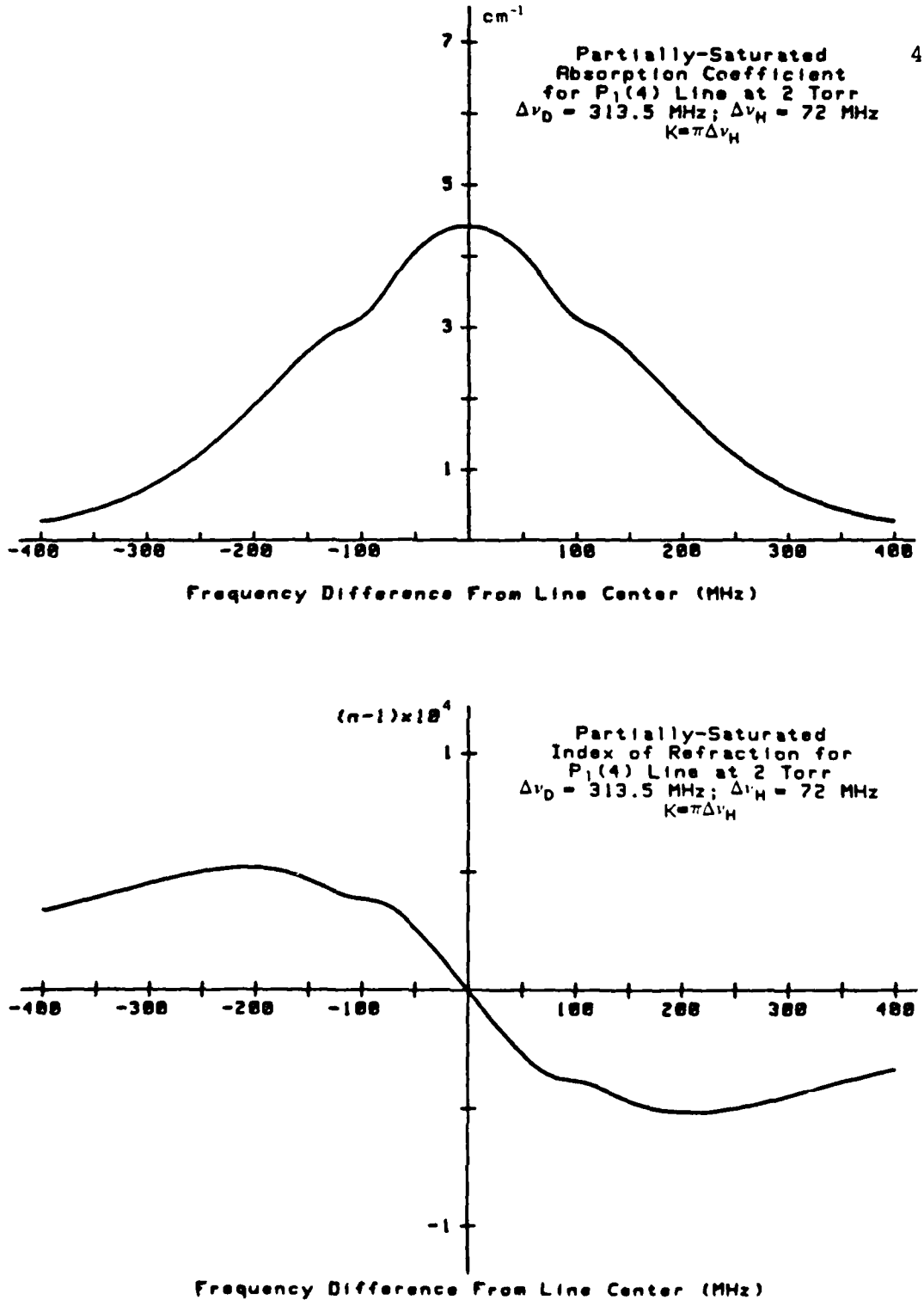

Figure 14. Saturated Absorption and Index of Refraction Curves for 75 cm Cavity ($K = \pi\Delta\nu_H = 113 \times 10^{7}$/sec-torr)

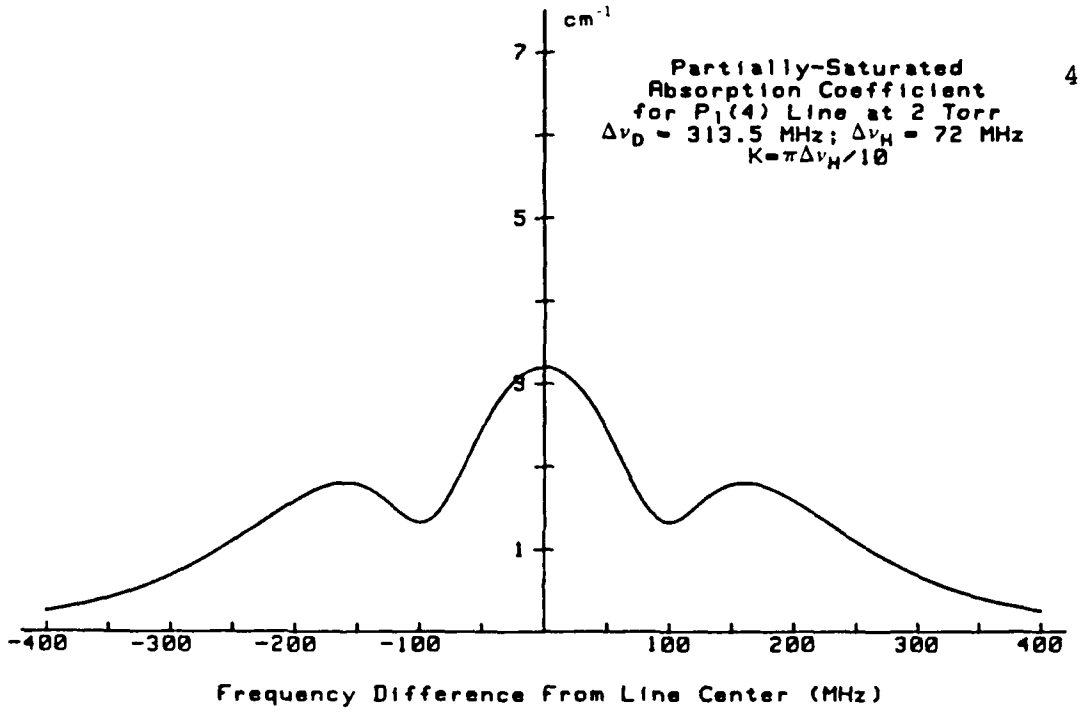

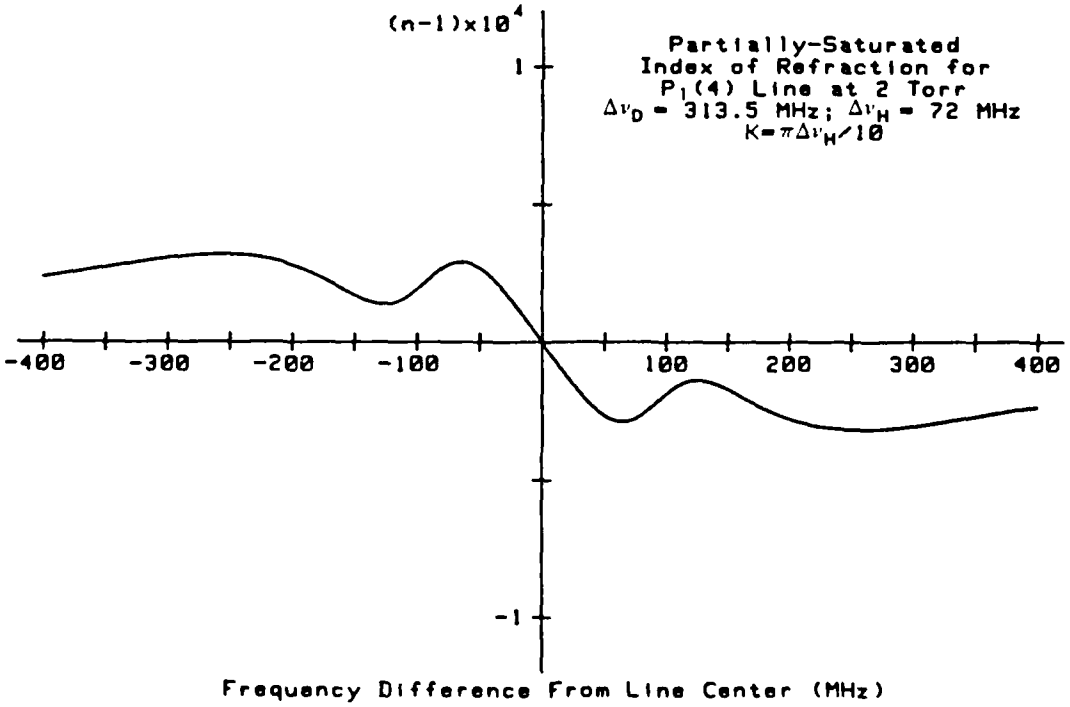

Figure 15. Saturated Absorption and Index of Refraction Curves for 75 cm Cavity ($K = \pi\Delta\nu_H/10 = 11\times10^{7}$ /sec-torr)

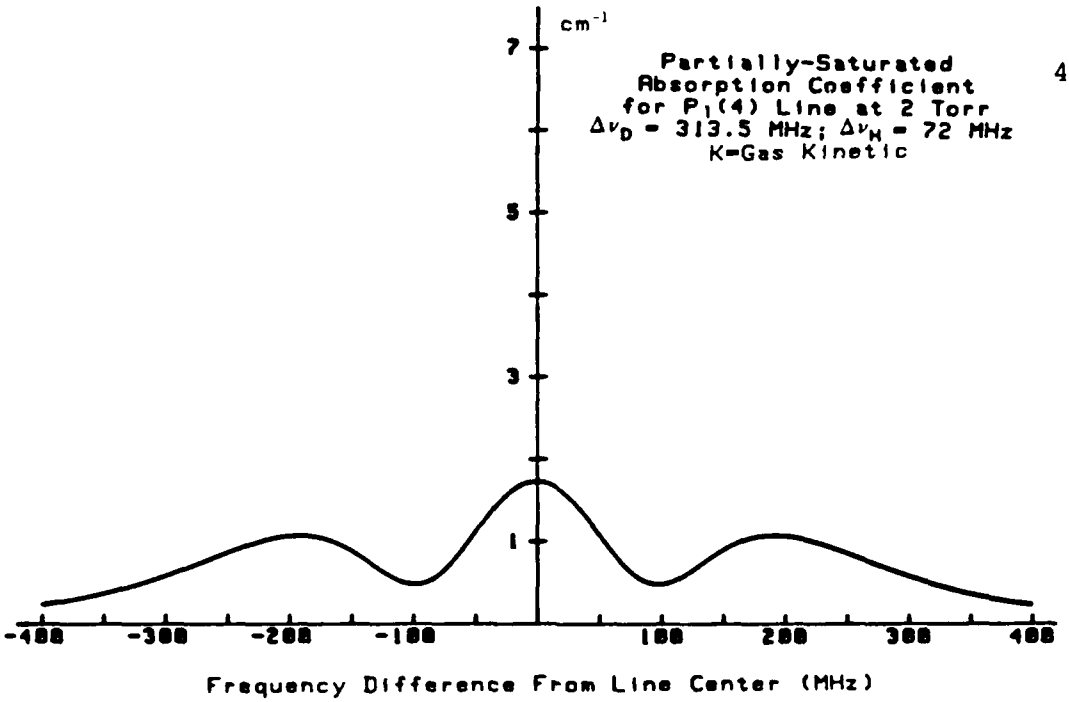

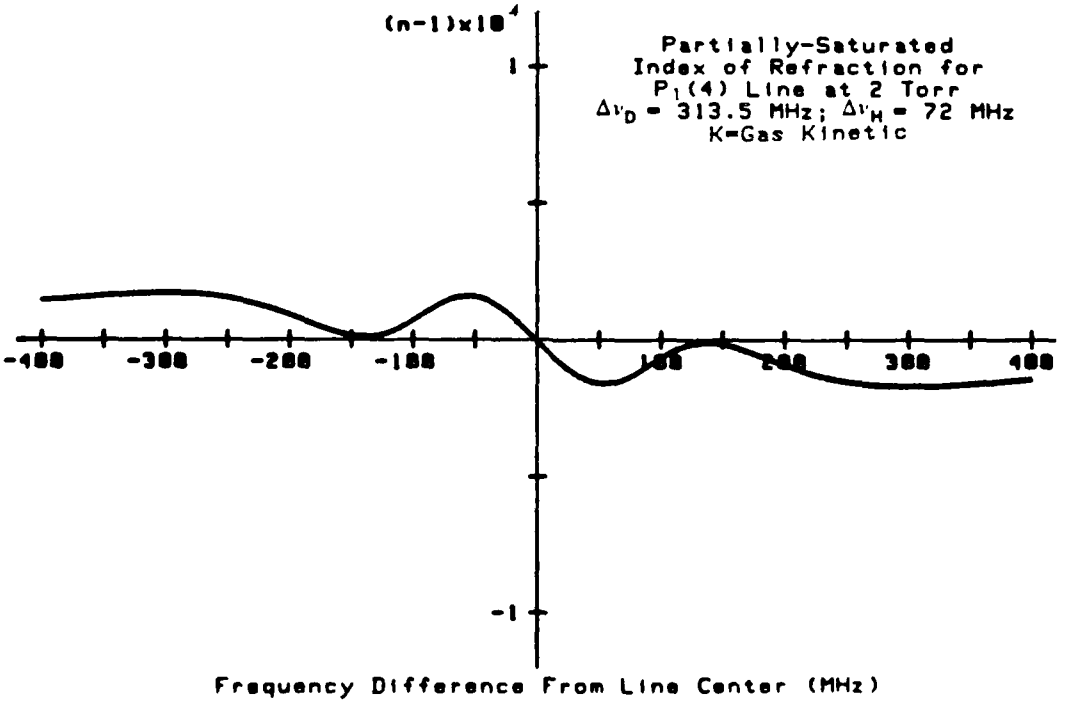

Figure 16. Saturated Absorption and Index of Refraction Curves for 75 cm Cavity (K = Gas Kinetic = $3x10^6$/sec-torr)

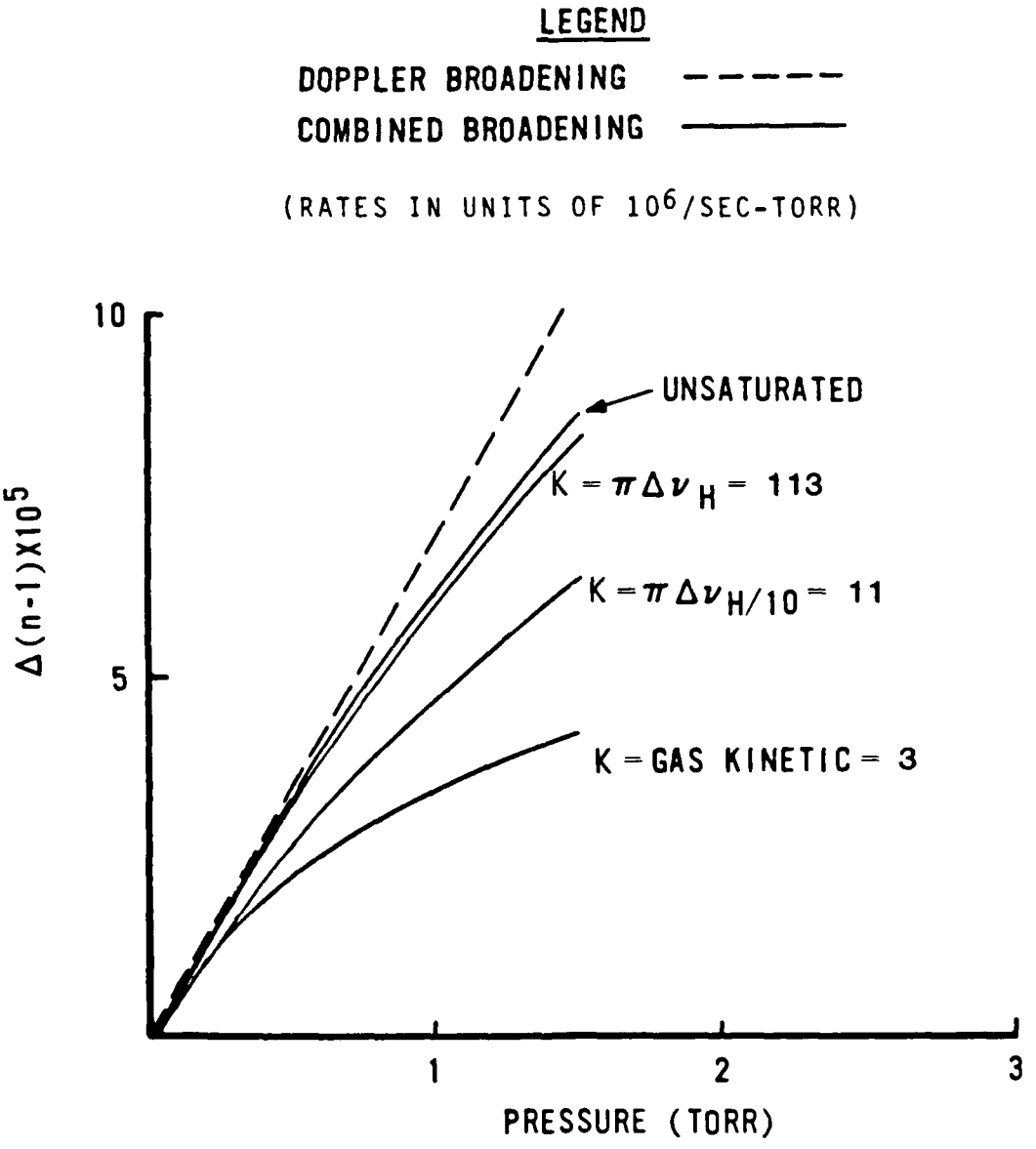

Figure 17. Theoretical Doppler and Combined Broadening Curves for 47.3 cm Cavity.

CHAPTER 4

EXPERIMENTAL APPARATUS

The Laser

A Helios CLIIIb HF/DF Chemical Laser was used for all of the experiments. This particular model is a probe laser capable of generating single-transition laser radiation by means of a Zero-Order Grating Coupler (Fig. 18). The coupler employs a 300 line/mm blazed grating that selects a line by returning the 1st order Littrow diffracted beam to the rear mirror of the laser cavity. The specular reflection of the grating is output-coupled by a copper mirror attached to the same mount as that holding the grating. The advantage of this arrangement is that, regardless of the transition selected, the output beam emerges in a constant direction.

The active medium was produced by the reactions

$$SF_6 + O_2 + He \rightarrow 6F + SO_2 + He \quad , \tag{4.1}$$

$$2F + H_2 \rightarrow 2HF^* \quad , \tag{4.2}$$

where HF^* denotes HF in an excited vibrational state. Helium, oxygen, and sulfur hexafluoride were first introduced to the discharge tube (see Fig. 19) where free fluorine was generated. The helium served as a buffer gas while the oxygen was used to scrub the sulfur. As can be

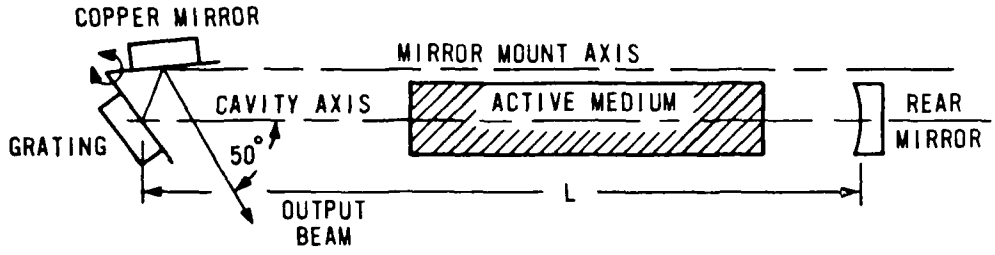

Figure 18. Laser Cavity with Zero-Order Grating Coupler

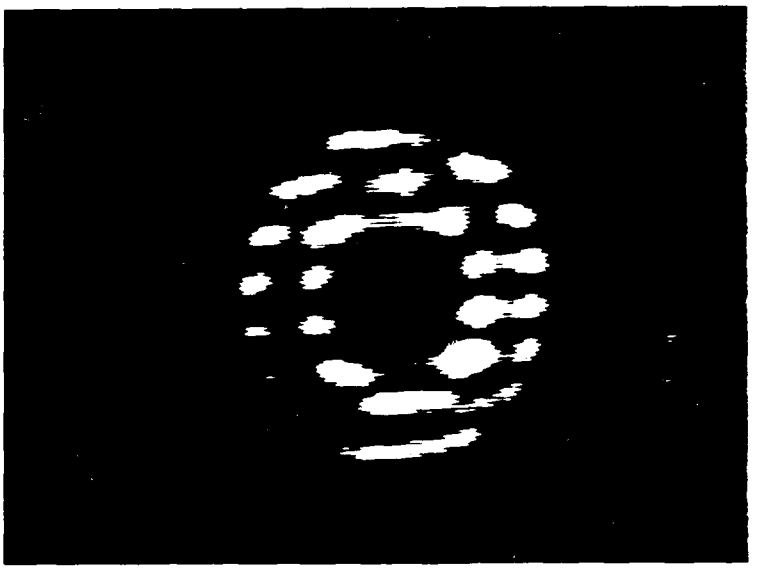

a.

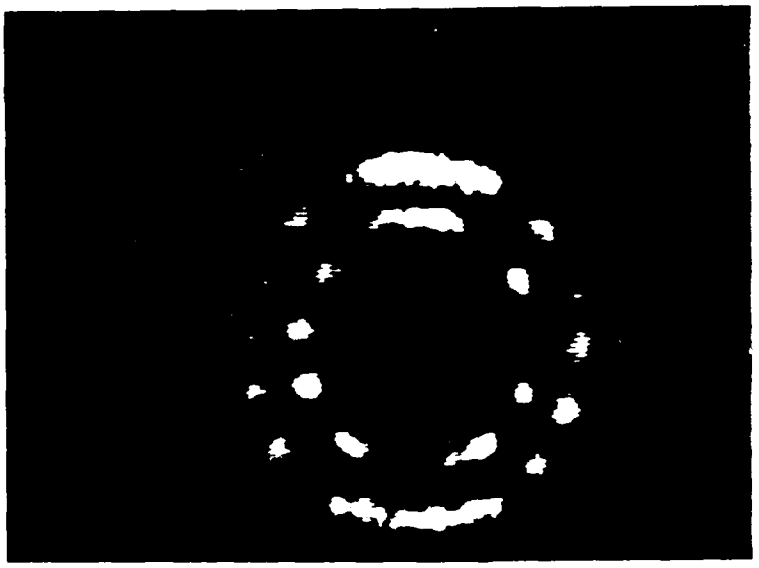

b.

Figure 26. Axially-Symmetric View of Combined Interference Pattern

a. Empty Gas Cell
b. HF in Gas Cell

Typically we repeated runs with like conditions a number of times in order to provide many independent data points for analysis.

pattern (co-located at infinity) was focussed at the camera by mirror M1 (f = 1 m), which was situated one meter from the camera.

Fringe Visualization Technique

The optical path difference between the two legs of the Michelson interferometer was intentionally made to be close to zero to ensure that any measured fringe shift was due exclusively to anomalous dispersion. The Fabry-Perot was adjusted to give well-focussed rings and the Michelson mirrors were adjusted to give horizontal fringes, as seen in Fig. 26a.

We began each experimental run by evacuating the gas cell thoroughly by pumping on it for several hours. Fresh gas was then slowly admitted into the cell until a steady pressure was achieved by properly coordinating the needle valves. With the gas pressure steady, we would then push on the laser-cavity grating mount with our fingers in order to get two modes of fairly equal intensity oscillating. Our feedback mechanism was simply the television screen that continually monitored the camera signal. Figure 26b shows a good data point in which anomalous dispersion is clearly seen. Like Fig. 26, Fig. 27 gives a qualitative comparison between the zero-pressure and nonzero-pressure cases. The difference is that Fig. 27 is a view obtained by tilting the Fabry-Perot interferometer slightly off axis. Fig. 28 shows two modes of uneven intensity (an improper point). All data were recorded for later analysis. Once we were certain that we had seen two equal-intensity modes, we noted the location on the tape and went on to the next gas pressure.

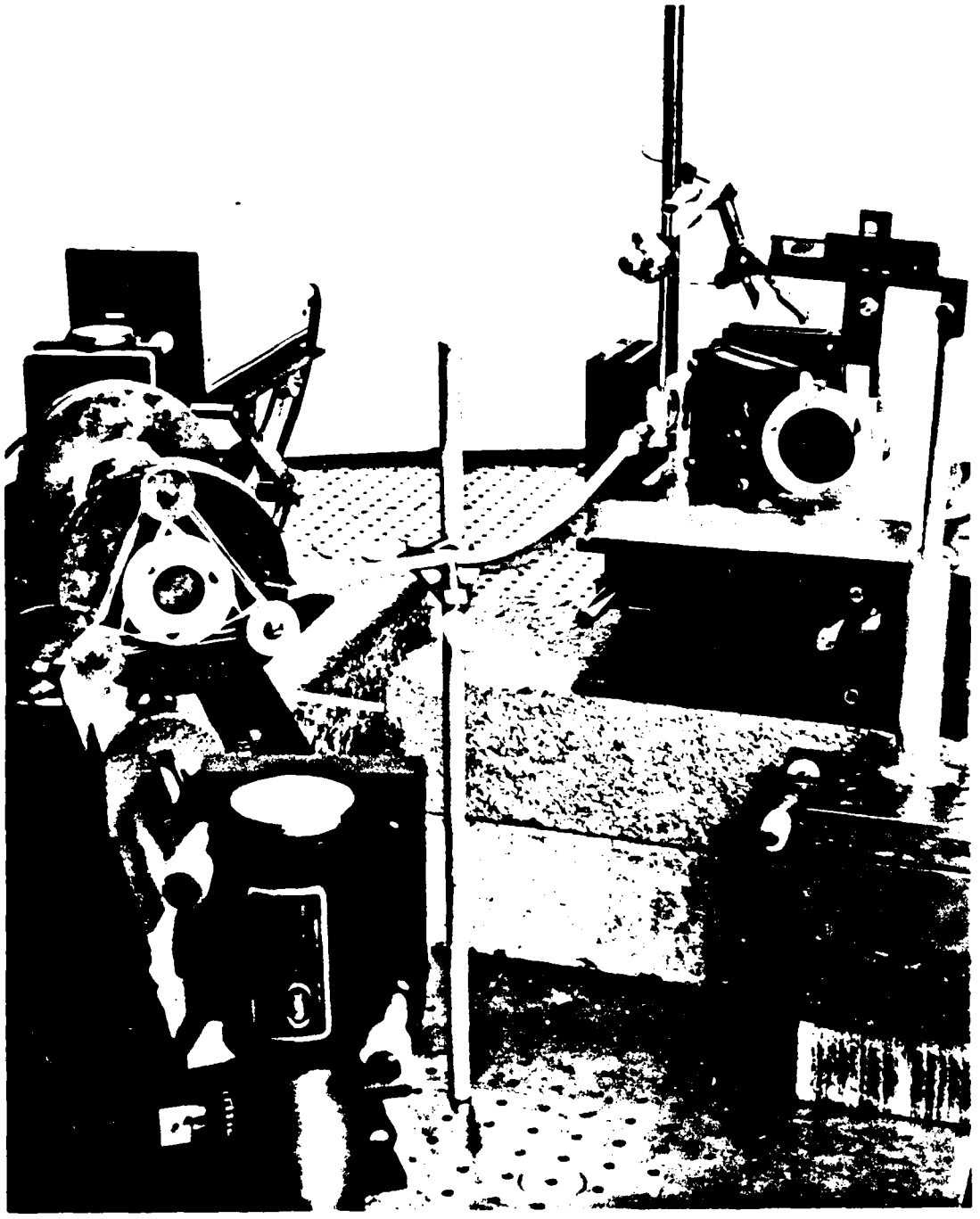

Figure 25. Optical Diagnostics for Saturated Measurements

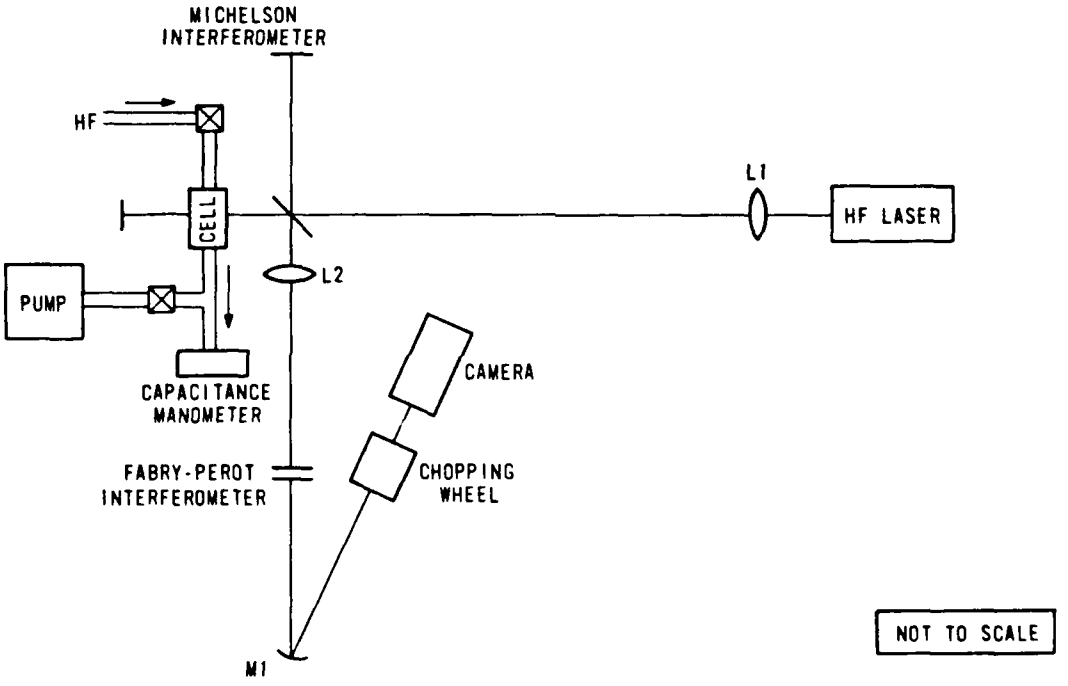

Figure 24. Optical Diagnostics Diagram for Saturated Measurements

with an MKS Instruments 170M-27E Digital Readout Unit and 170M-66 Baratron and Pressure Head.

The combined Fabry-Perot and Michelson interference patterns were imaged by an I.S.I. Group Model 86 Thermal Imaging System Camera Head and Remote Camera Control Unit. This type of camera is a pyroelectric vidicon system that responds to time-changes in temperature on the Triglycine Sulphate (TGS) target. Thus, a steady-state input must be interrupted by panning the camera or chopping the beam. We decided to chop the beam mechanically. Mirror M2 had a 40 cm focal length. We viewed our data with an RCA TC1210 Video Monitor and recorded it with a Sony VO-2610 Video Cassette Recorder/Player. A Datum 9310-100 Time Code Generator/Translator was used to imprint a time code on the audio track of the tape, thereby enabling us to accurately locate and review data.

Experimental Layout for Saturated Measurements

We were able to partially saturate the transition by changing the order of the interferometers as shown in Fig. 24. Figure 25 is a photograph of the same arrangement. Lens L1 (f = 1 m), which was located 68.5 cm from the gas cell, reduced the beam diameter (at the cell) to approximately a millimeter, a third of its original size. We measured the intensity profile by removing one of the cell windows and then sequentially measuring power through one of several different-sized holes placed just behind the cell window (see Chap. 5). Lens L2 (f = 15 cm) was placed one focal length from the Michelson back mirrors so as to image the fringes at infinity. As can be seen in Fig. 24, the Fabry-Perot interferometer followed the Michelson. The combined

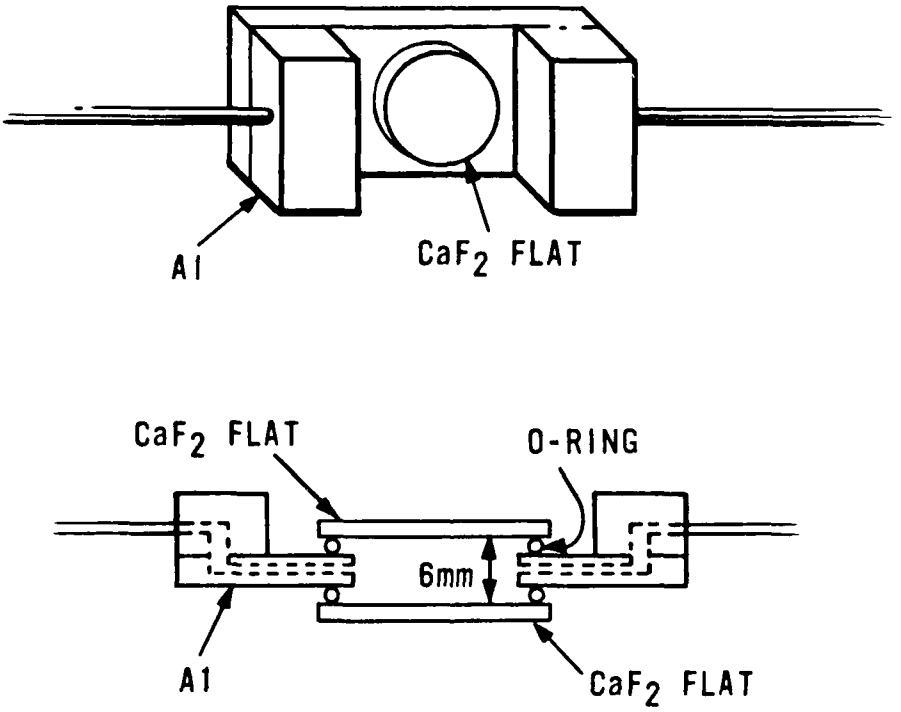

Figure 23. Gas Cell Construction

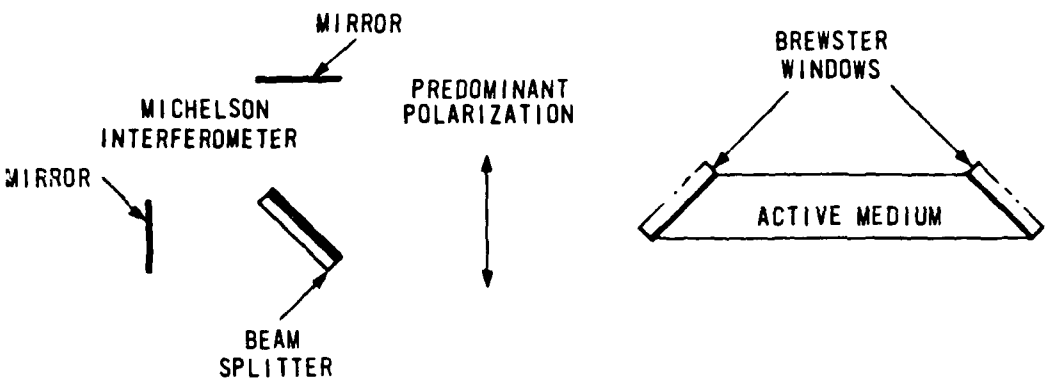

Figure 22. Relative Orientation of Brewster Windows and Michelson Beam Splitter

optical path difference (OPD) of the two legs was intentionally made to be small (see page 64). The Michelson thus served as a Fizeau interferometer in that the 100% mirrors formed a slight wedge. Accordingly, the lines of constant phase were localized at or near these mirrors (Born and Wolf, 1975). Mirror M1 (f = 1 m), then, which was placed one meter from the Michelson mirrors, focussed the Fabry-Perot pattern (originally at infinity) in the same image plane as the Michelson fringes.

The beam splitter was a CaF_2 flat specially coated on the front surface for 50% reflection at 45 degrees. The back surface had no coating (although an AR coating would have been desirable). Thus, the beam splitter was intentionally situated with the same relative orientation as the laser Brewster windows, as shown in Fig. 22. We did so in order to minimize reflection of the predominant polarization from the back surface of the beam splitter by taking advantage of the near-Brewster angle beam incidence. This simple precaution helped to eliminate unwanted interference patterns caused by an additional reflecting surface.

A schematic of the gas cell is contained in Fig. 23. It was constructed of aluminum and a pair of high optical-quality CaF_2 flats. Because passivation with HF proved difficult, we opted for a flowing gas system instead of a static system. We achieved steady pressures as low as .075 torr by using a Welch Duo-Seal Model 1402 Vacuum Pump and the needle valve arrangement shown in Fig. 21. Pressures were monitored

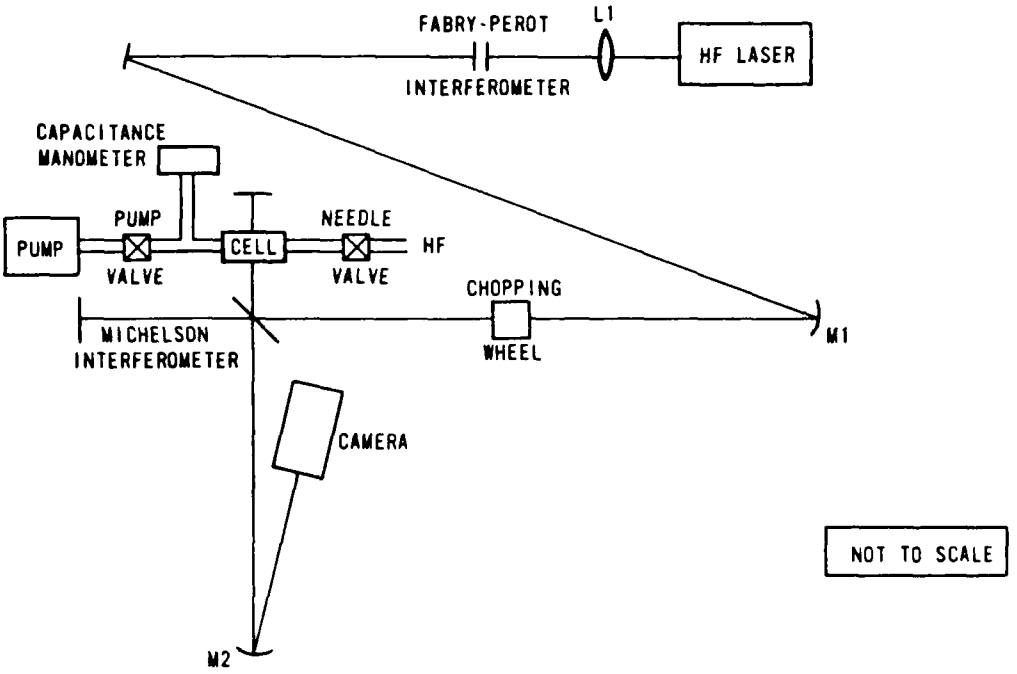

Figure 21. Optical Diagnostics Diagram for Unsaturated Measurements

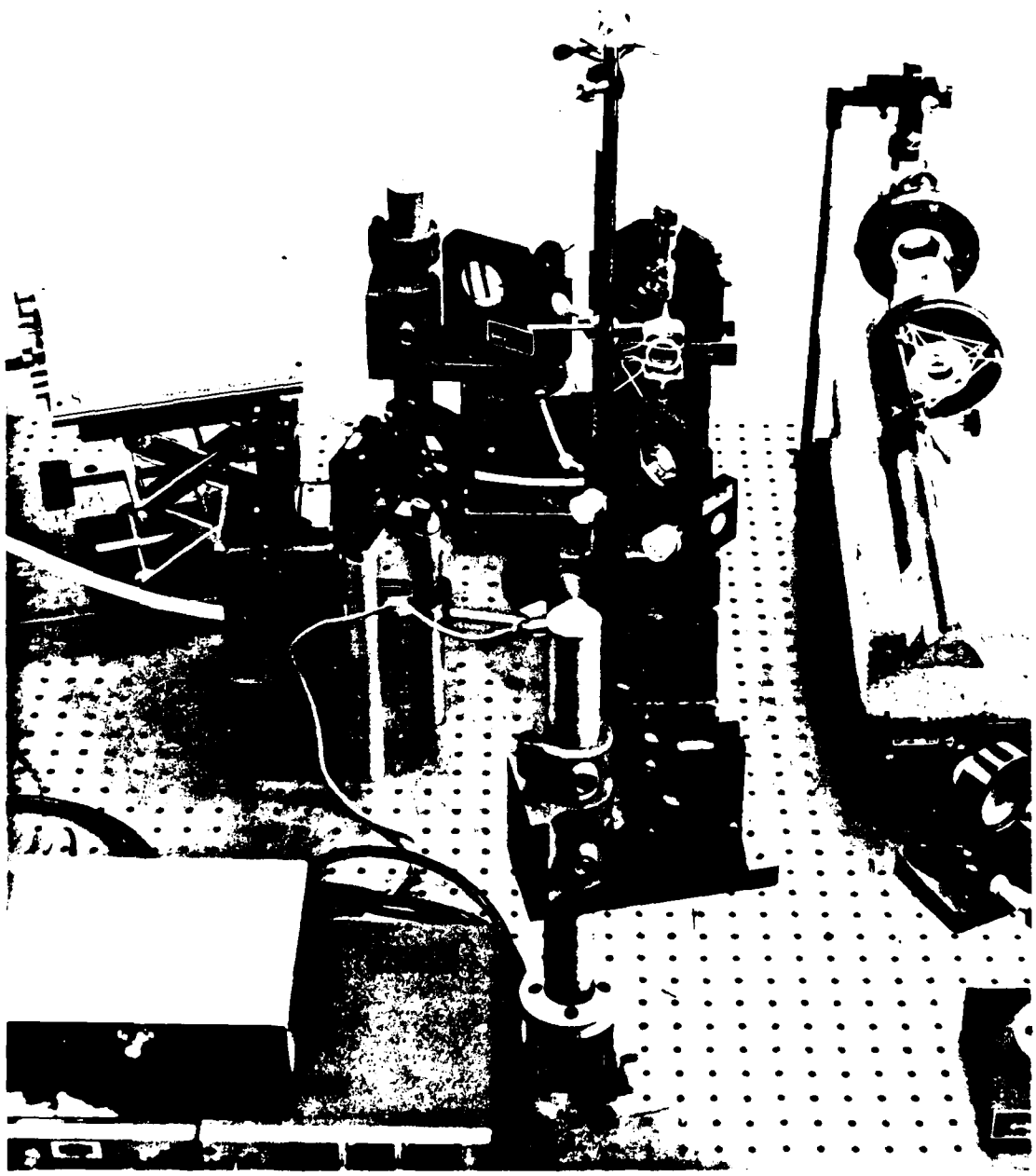

Figure 20. Optical Diagnostics for Unsaturated Measurements

The solution involved placing the laser upon an optical table suspended by four inflatable wheelbarrow innertubes. The table isolated the laser cavity from external vibrations, and mode control was attained by manually applying increasing pressure to the grating mount until two modes of fairly equal intensity appeared.

Experimental Layout for Unsaturated Measurements

We obtained all of the unsaturated data with the optical diagnostics equipment pictured in Fig. 20 and diagrammed in Fig. 21. The HF beam first went through a diverging lens and then through a Fabry-Perot interferometer with one-inch calcium fluoride (CaF_2) plates. These plates were 98% reflective on one side and anti-reflection (AR) coated on the other. The purpose of lens L1 (f = 3 cm) was to enable us to obtain the maximum resolution possible by completely filling the interferometer plates (see Chap. 6). The interferometer itself consisted of two mounts separated rigidly by a quartz tube. Each mount was machined of a single piece of steel using a design created by machinist Carl Pelander of the Joint Institute for Laboratory Astrophysics (JILA). Appendix B contains a close-up photograph and a copy of the blueprint used in the mount's construction. A distinct advantage of this particular design is stability; it was not uncommon for us to leave the interferometer alone for a week or two and return to find the plates still aligned. The three lever-arms allowed for very fine plate adjustments with comparatively course set-screw adjustments.

The Fabry-Perot pattern was sent, via focussing mirror M1, into a Michelson interferometer, one leg of which contained a gas cell. The

Table 2. Laser Lines and Powers

		Maximum Power (Watts)		
Line	λ (μm)	47.3 cm Cavity	75 cm Cavity	87 cm Cavity
$P_1(2)$	2.58	-	.4	.5
$P_1(3)$	2.61	.8	.7	.7
$P_1(4)$	2.64	1.3	1.3	1.4
$P_1(5)$	2.67	1.1	.6	.5
$P_2(2)$	2.70	-	-	.3
$P_1(6)$	2.71	1.7	1.4	1.1
$P_2(3)$	2.73	.8	1.1	1.9
$P_1(7)$	2.74	1.7	.6	1.6
$P_2(4)$	2.76	1.2	1.3	1.3
$P_1(8)$	2.78	1.1	.8	-
$P_2(5)$	2.80	1.6	2.1	2.2
$P_2(6)$	2.83	2.0	2.3	2.3
$P_2(7)$	2.87	1.8	2.1	2.0
$P_2(8)$	2.91	1.2	1.2	1.3

for available gain was high, and without any cavity stabilization, mode jumping occurred regularly with one mode being favored at any particular time. Lowering the cavity pressure to five torr allowed two-mode oscillation, but the modes still raced through the gain curve while power dropped to an unacceptable level.

seen in Fig. 19, the gas flowed transverse to the laser cavity. Hydrogen was injected just upstream of the cavity where it combined with the fluorine to produce the upper lasing state.

The discharge was powered by a Universal Voltronics Corporation Model BAM-13-200H High Voltage Power Supply, and the spent gases were evacuated by a Kinney KT-500 Triplex Vacuum Pump. Because of the pump's excellent operating capacity (> 500 cfm), we were able to extract single-line powers up to two watts on some transitions. Power was measured with a Coherent Model 210 Power Meter, and was maximized at cavity pressures around nine torr. We used three cavity lengths for the experiments: 47.3 cm, 75 cm, and 87 cm. Each cavity included a two-meter-radius rear mirror. Table 2 is a listing of the lines and maximum powers attainable with each cavity.

Since the experiments involved absorption in HF at room temperature, a v(1-0) transition was desired. We chose the $P_1(4)$ and $P_1(6)$ lines because of their good output powers for each of the three cavities.

We naturally needed to generate two or more axial (longitudinal) modes in order to measure fringe shift. It was difficult at times, however, to get two stable modes oscillating and virtually impossible to get three, even on the longest cavity. There were two reasons for this. First, the laser was subject to a lot of vibration coming through the floor of the laboratory, causing modes to race through the gain curve. The second reason involved mode competition caused by pressure-broadening effects. Even at cavity pressures as low as seven torr, competition

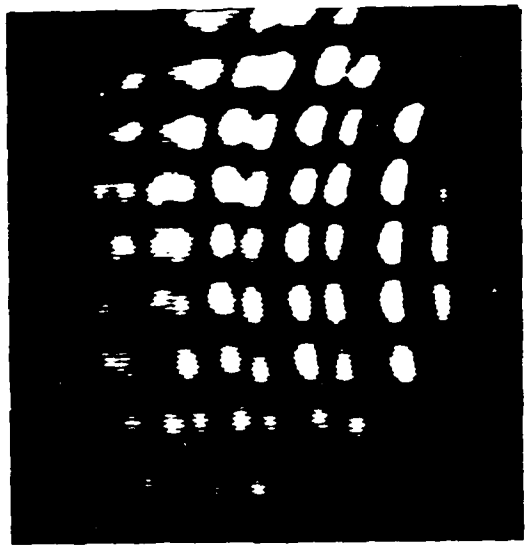

a.

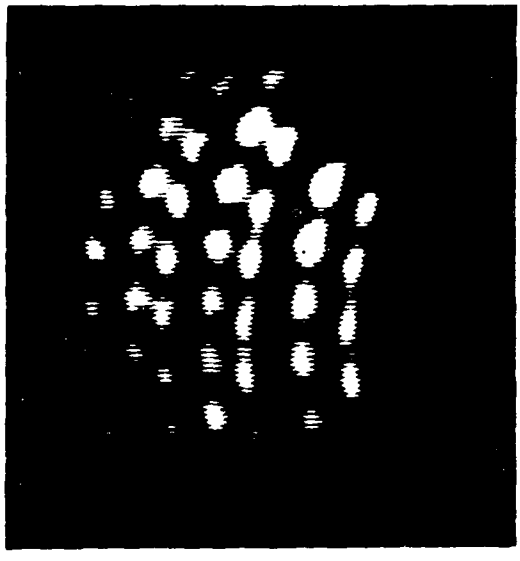

b.

Figure 27. Off-Axis View of Combined Interference Pattern

a. Empty Gas Cell
b. HF in Gas Cell

a.

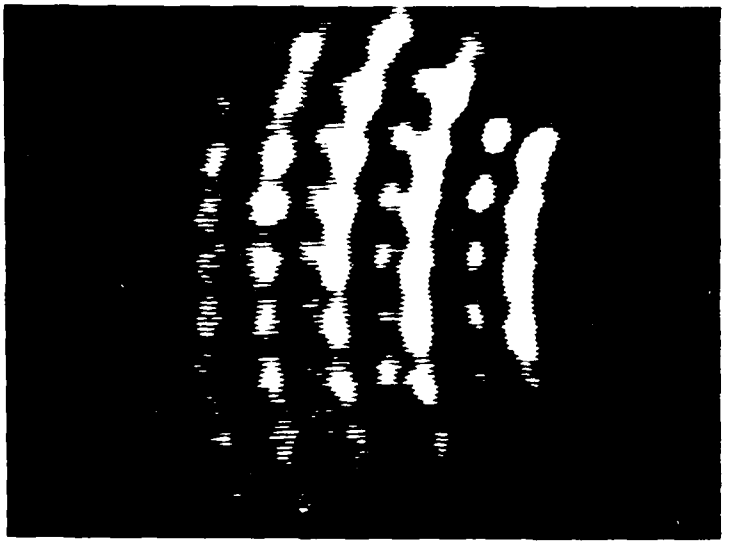

b.

Figure 28. Modes of Unequal Intensity

a. Axially-Symmetric View
b. Off-Axis View

CHAPTER 5

EXPERIMENTAL RESULTS

Data Reduction

Most of the data taken looked like Fig. 26b. Some, however, resembled Fig. 27b, in which the Fabry-Perot interferometer was moved slightly off axis. We originally thought that this side view was better in that the increased number of dots would enable us to draw better lines for measuring fringe shift. We quickly found, though, that aberrations in the optical system often prevented us from drawing straight lines at all. Therefore, we abandoned this approach early in the experiment, and, with the exception of a few sets of "readable" data of this kind, all are like Fig. 26b.

Each data point was read by first marking the center (high-intensity point) of each dot with a scribing tool. Since this involved subjective judgment, three people read pictures and the results were averaged. Once the centers were determined, lines were drawn between dot pairs as shown in Fig. 29. A single vertical line was drawn down the center. Then, using a binocular microscope, we measured (along this center line) an average Michelson spacing and an average fringe displacement between the two modes. The ratio of the two numbers gave us a percent fringe shift for that picture. All such numbers for the same pressure and cavity length were then averaged and a standard deviation was computed. It should be noted here that each average value typically

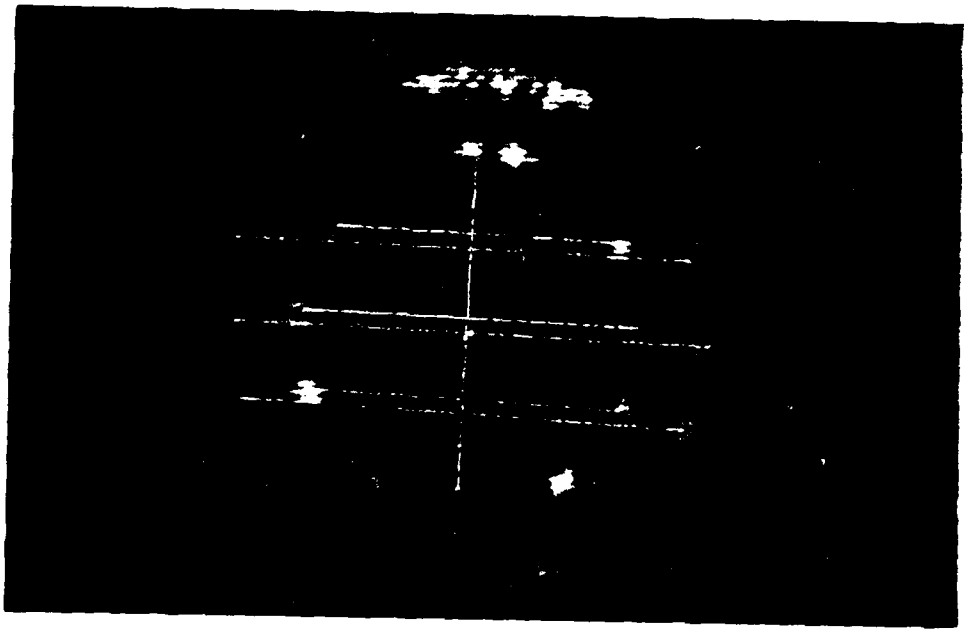

Figure 29. Data Point Prepared for Measuring Fringe Shift

included over 20 different data points (accumulated at different times) for the same pressure and cavity configuration. Using three readers gave us independent measurements of the same data points. Thus, the computed error bars represent not only the scatter in the various readings, but a measure of the experimental reproducibility as well.

We converted a percent fringe-shift value to a difference in refractive index "seen" by the two modes by using

$$\Delta(n-1) = (\lambda/2\ell)(\%\text{shift}) \ , \tag{5.1}$$

where ℓ represents the length of the gas cell. Note that the factor of two in the denominator appears because the beam passes through the cell twice. The experiment could be performed with a Mach Zehnder interferometer and the factor of two would be absent.

Tabulated results for both the unsaturated and saturated experiments are contained in Appendix C. Figures 30 through 37 contain plots of those results along with the theoretical curves.

Determining the Mode Spacing

An accurate determination of the frequency separation between modes was necessary in constructing the theoretical plots shown in Figs. 30 through 35. We did this both by calculation and by two experimental methods. Each is now briefly described.

Calculating the Mode Pulling

Frequency pulling is a direct result of the anomalous refractive index of the gain medium. Modes which are oscillating away from line

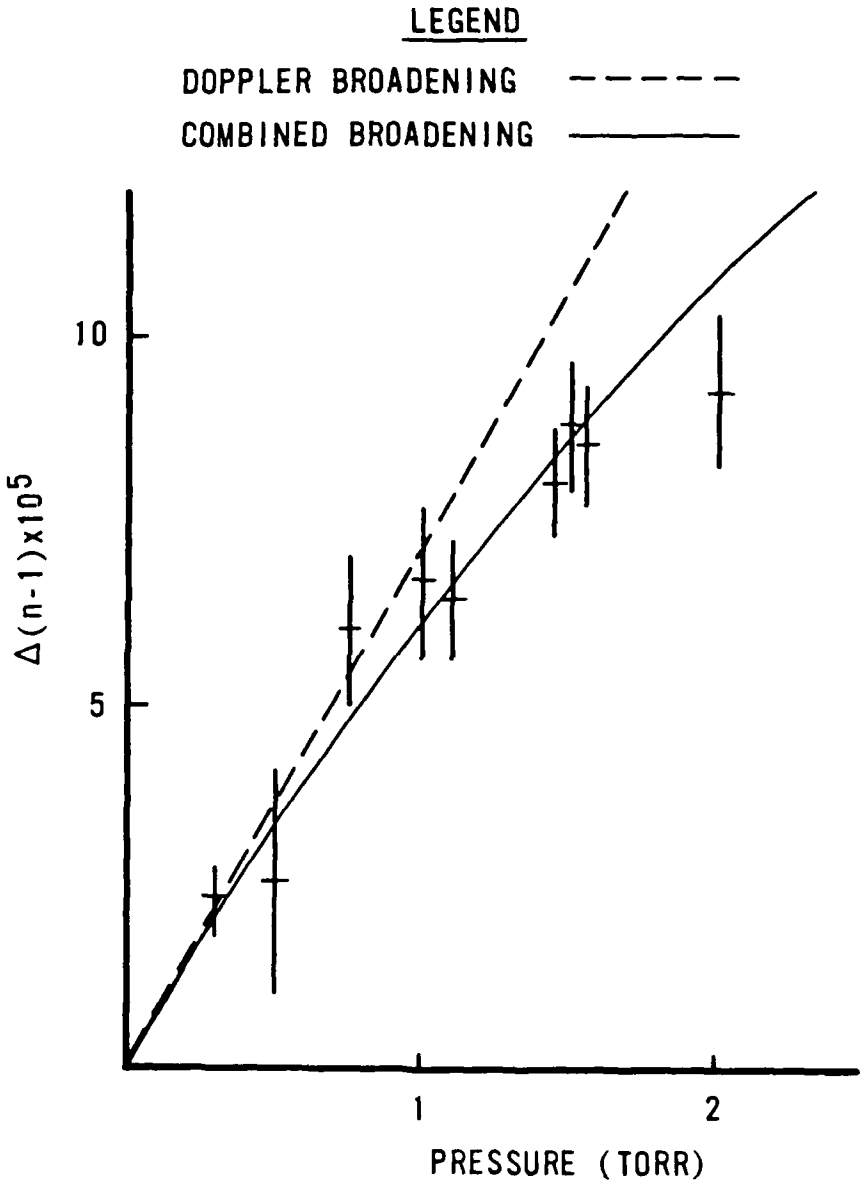

Figure 30. Theoretical and Experimental Unsaturated Results for $P_1(4)$ Line, 47.3 cm Cavity

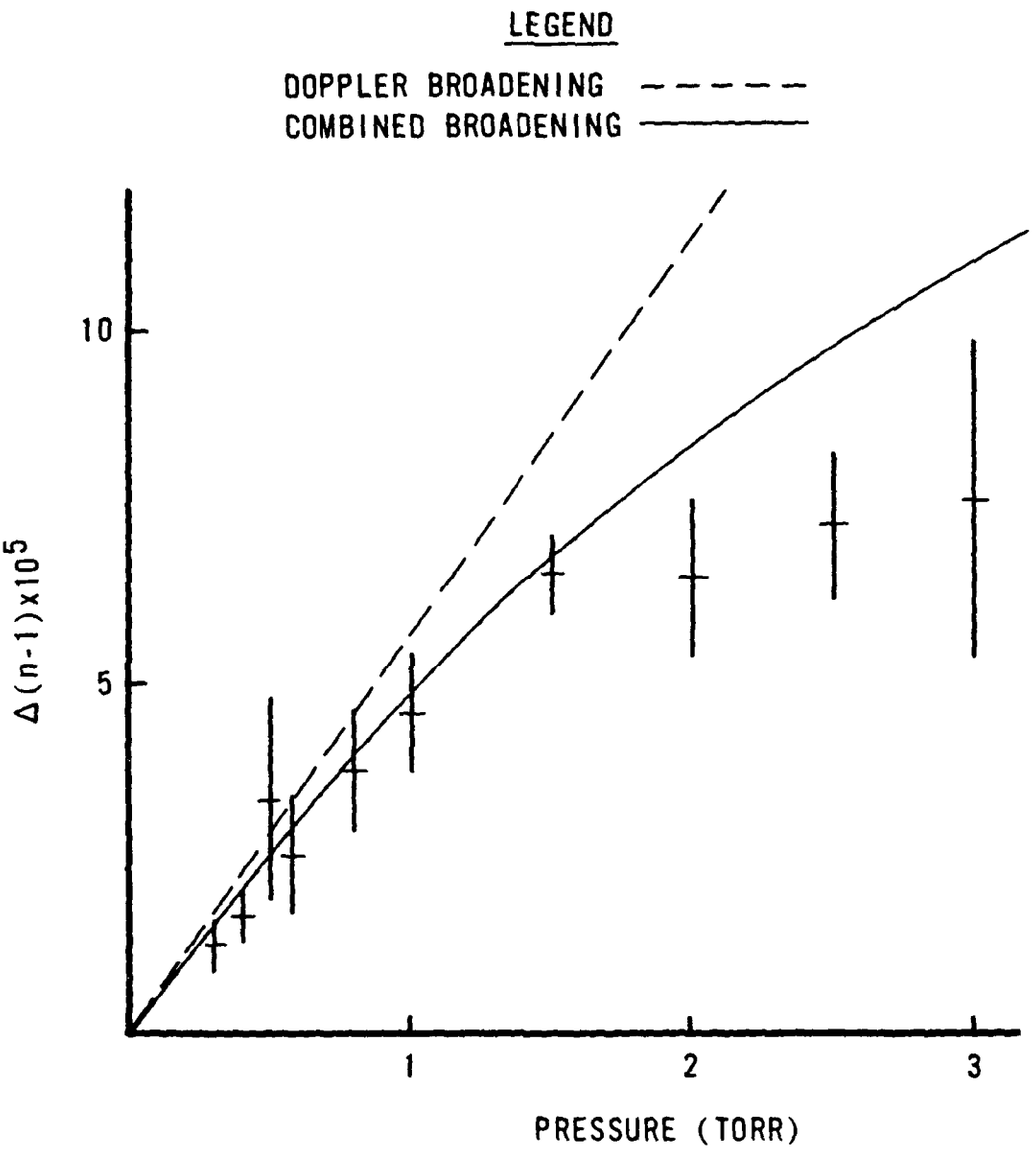

Figure 31. Theoretical and Experimental Unsaturated Results for $P_1(4)$ Line, 75 cm Cavity

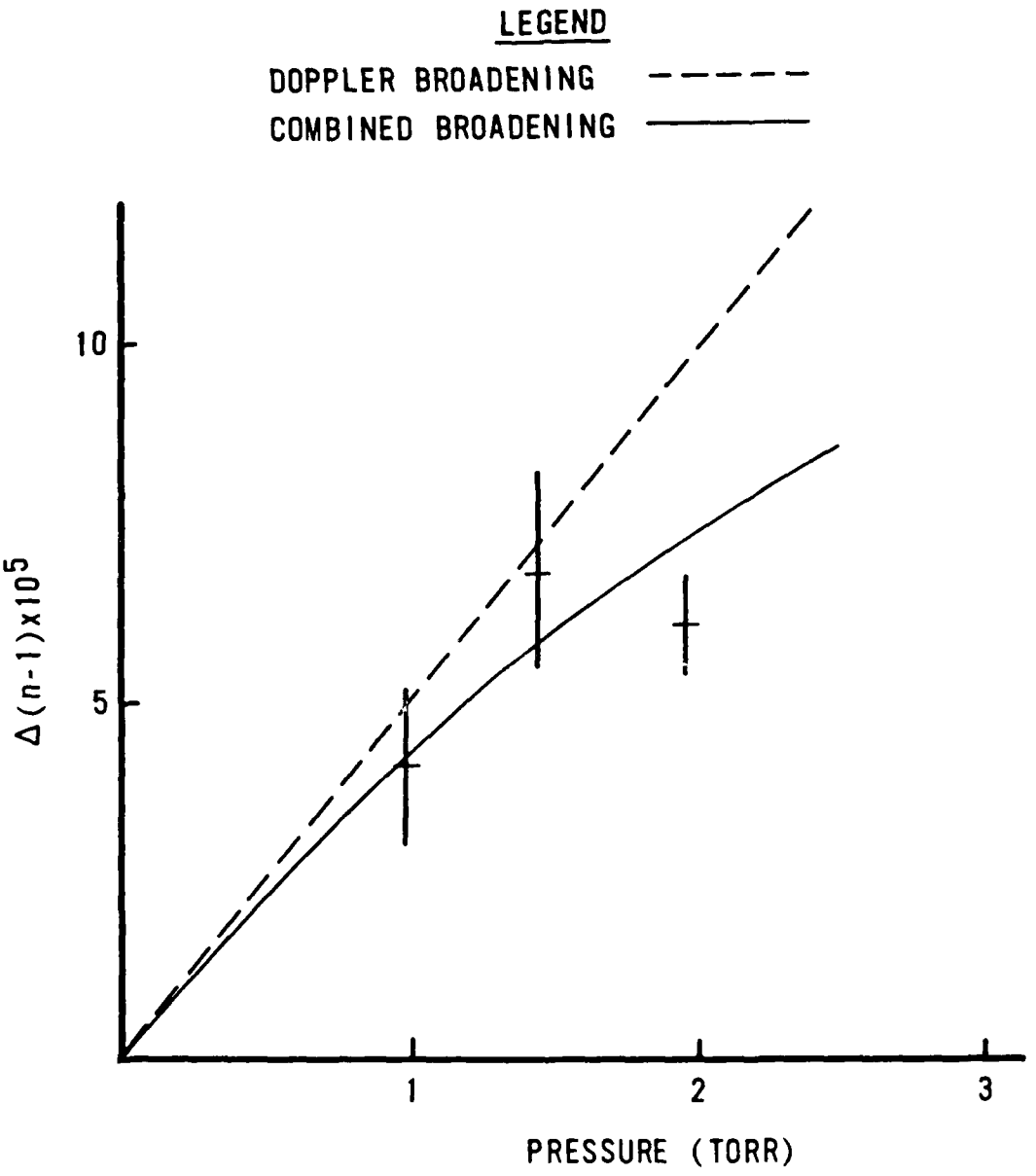

Figure 32. Theoretical and Experimental Unsaturated Results for $P_1(4)$ Line, 87 cm Cavity

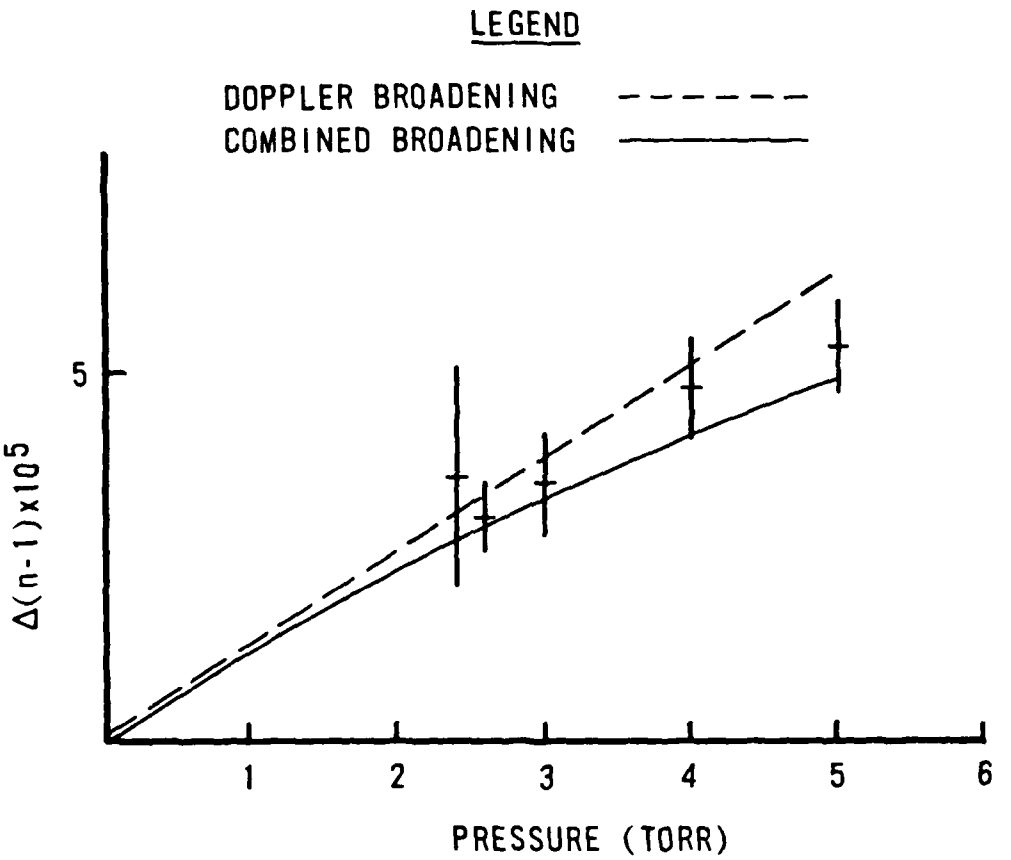

Figure 33. Theoretical and Experimental Unsaturated Results for $P_1(6)$ Line, 47.3 cm Cavity

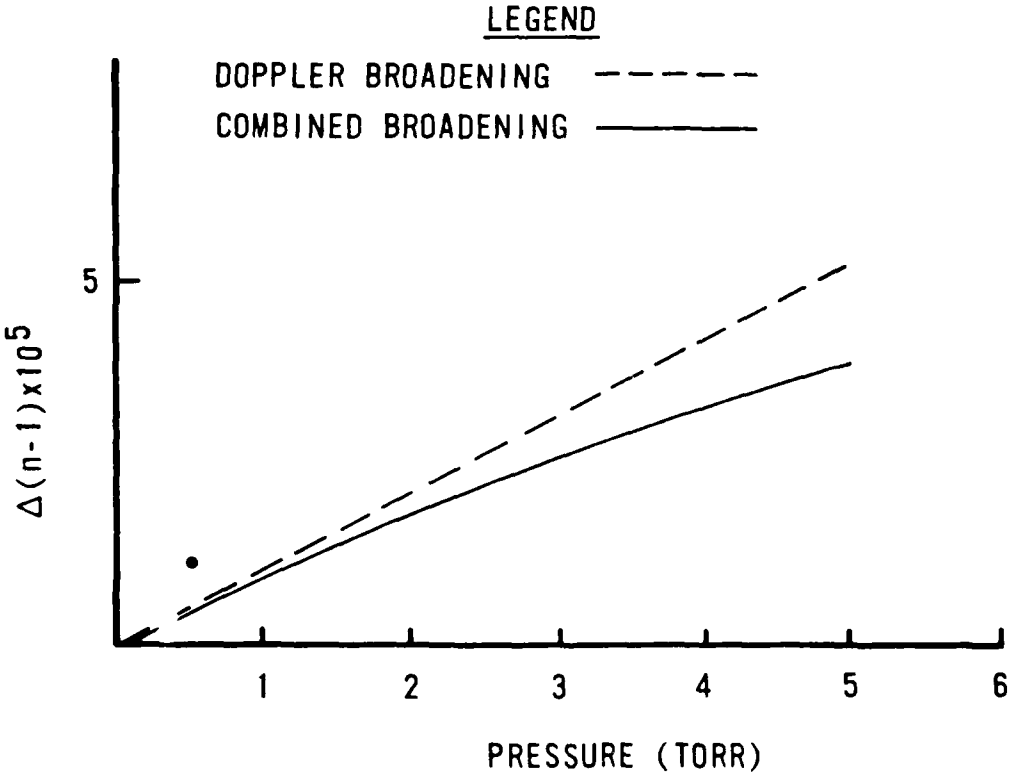

Figure 34. Theoretical and Experimental Unsaturated Results for $P_1(6)$ Line, 75 cm Cavity

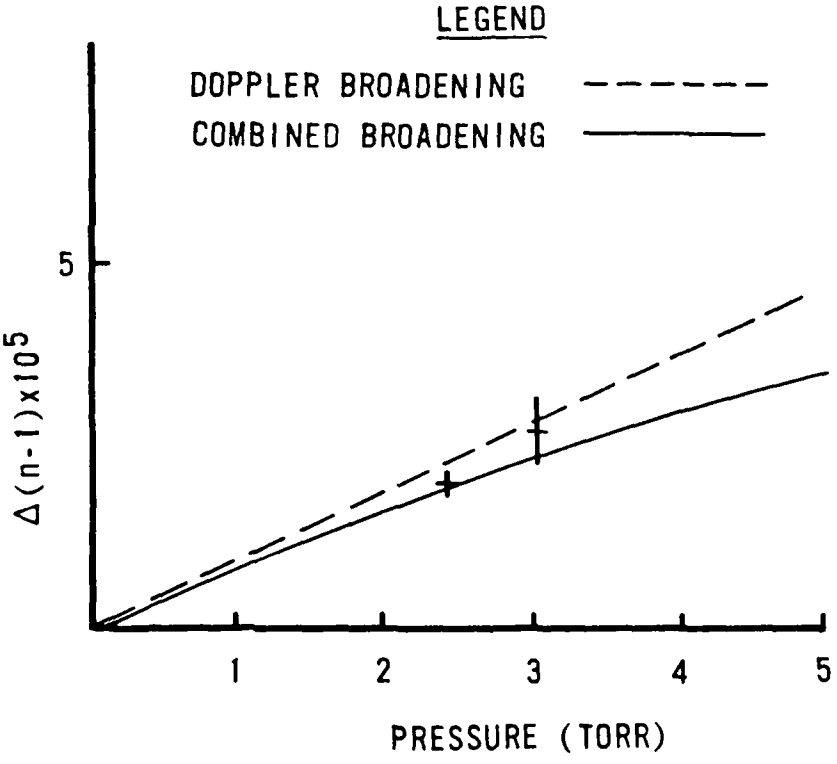

Figure 35. Theoretical And Experimental Unsaturated Results for $P_1(6)$ Line, 87 cm Cavity

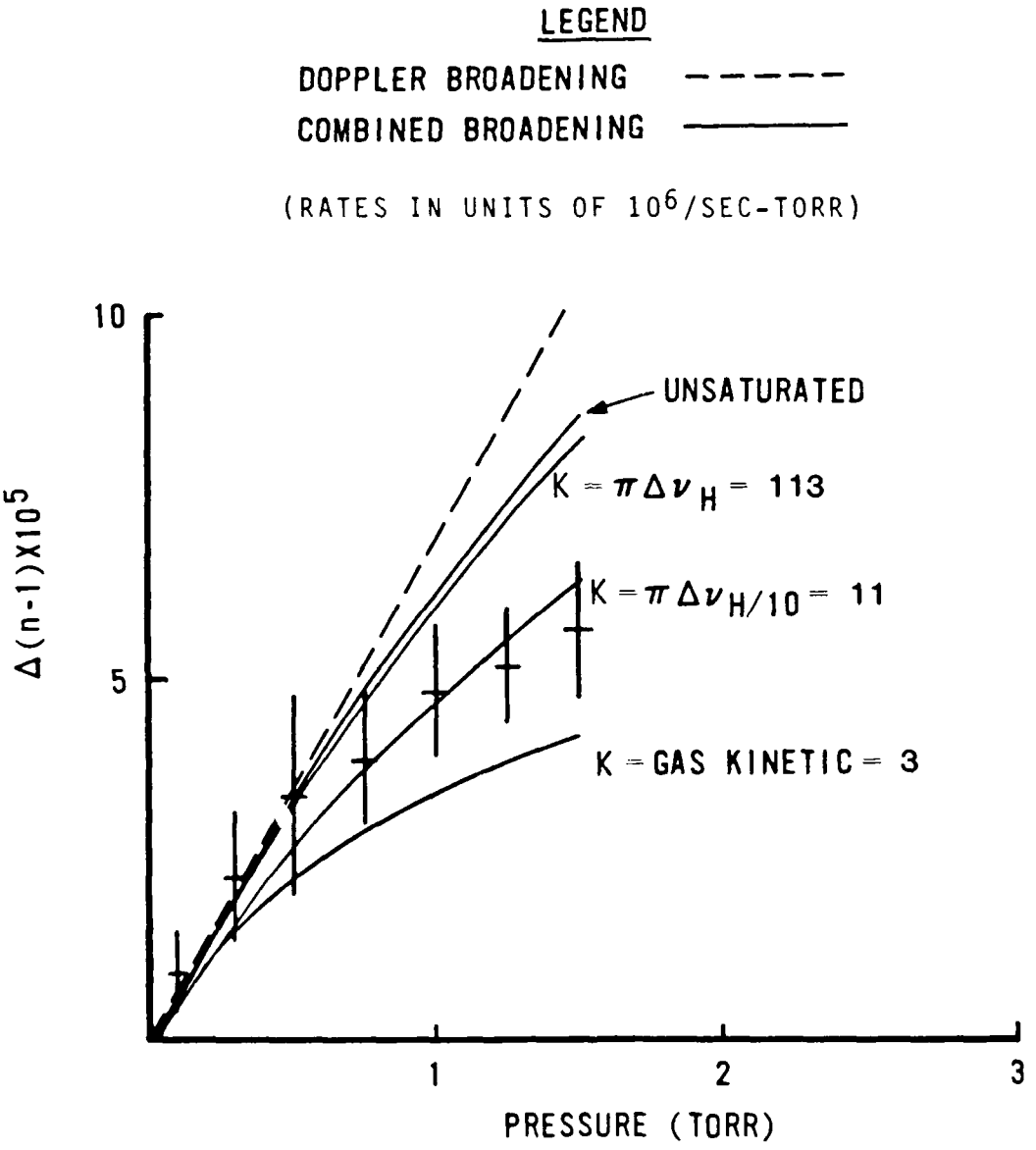

Figure 36. Theoretical and Experimental Saturated Results for $P_1(4)$ Line, 47.3 cm Cavity

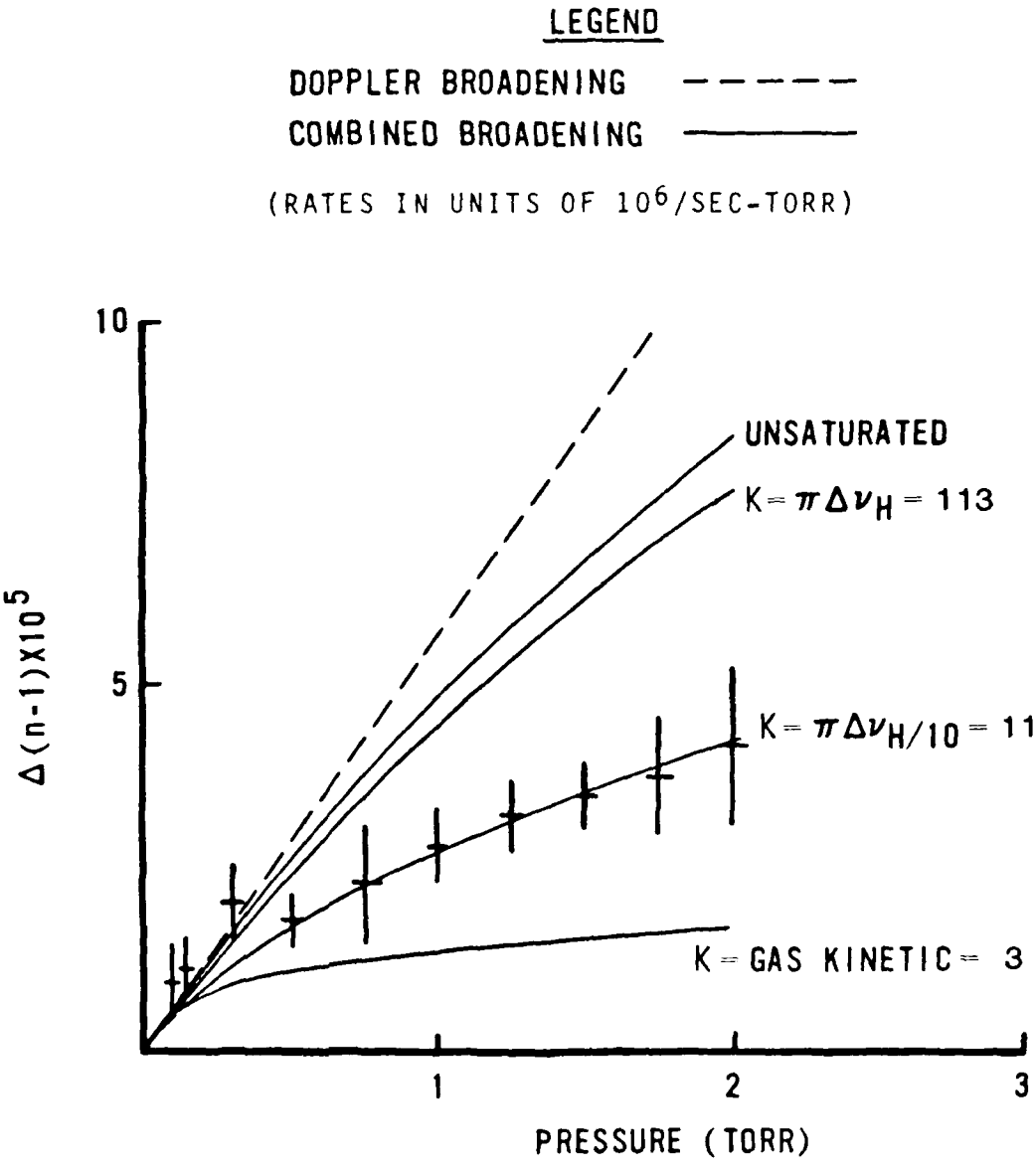

Figure 37. Theoretical and Experimental Saturated Results for $P_1(4)$ Line, 75 cm Cavity

center are "pulled" from their passive cavity position ν_m to a frequency closer to line center, implying a reduction from the passive-cavity free spectral range, $\Delta\nu_m = c/2L$, to a slightly smaller value.

For a cavity of length L containing a gain medium of length ℓ, the round-trip phase condition necessary for a mode to oscillate is

$$2\pi m = \frac{2\pi}{\lambda}(OPL) = \frac{2\pi\nu}{c}[n(\nu)2\ell + 2L - 2\ell], \tag{5.2}$$

where OPL is the optical path length, $n(\nu)$ is the index of refraction of the gain medium, and m is an integer. This can be written

$$\frac{mc}{2L} = \nu_m = \nu\left\{1 + \frac{\ell}{L}[n(\nu) - 1]\right\} . \tag{5.3}$$

Using Lamb's model, Donald Close (1967) developed the following equation for the frequency-dependent index of refraction of a Doppler-broadened amplifying medium

$$n(\nu) = 1 + \frac{cg_0 F(x)}{2\pi\nu_0}, \tag{5.4}$$

where

$$F(x) = e^{-x^2}\int_0^x e^{t^2}dt , \tag{5.5}$$

$$x = \left[\frac{2(\nu - \nu_0)}{\Delta\nu_D}\right]\sqrt{\ln 2} , \tag{5.6}$$

AD-A156 937 INTERFEROMETRIC MEARUREMENTS OF ANOMALOUS DISPERSION IN 2/2
HYDROGEN FLUORIDE(U) AIR FORCE INST OF TECH
WRIGHT-PATTERSON AFB OH J M RABINS MAY 85
UNCLASSIFIED AFIT/CI/NR-85-3D F/G 7/4 NL

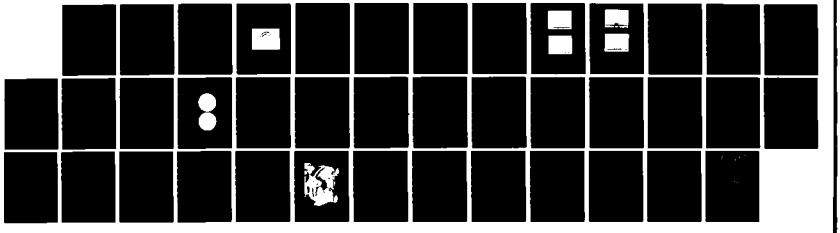

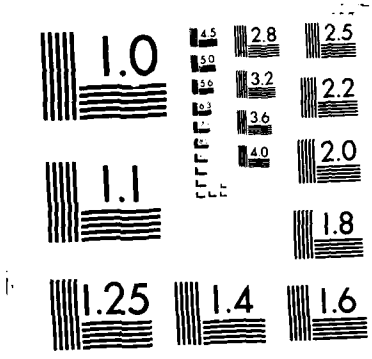

MICROCOPY RESOLUTION TEST CHART
NATIONAL BUREAU OF STANDARDS-1963-A

and g_0 is the small-signal gain coefficient at line center. Note that this equation is valid only when: (a) the homogeneous linewidth is negligible compared with the Doppler linewidth, or $\Delta\nu_H << \Delta\nu_D$; and (b) saturation is unimportant (Casperson and Yariv, 1970). Since neither of these conditions is clearly the case for our laser, the utility of this equation lies exclusively in the fact that it provides us a maximum possible mode-pulling value.

Using Eq. (5.4) for the index, Eq. (5.3) becomes

$$\nu_m - \nu = \frac{\ell}{L} \frac{cg_0 F(x)}{2\pi^{3/2}} \quad . \tag{5.7}$$

In non-dimensional form,

$$x_m - x = \beta F(x) \quad , \tag{5.8}$$

where

$$\beta \equiv \frac{\ell}{L} \frac{cg_0\sqrt{\ln 2}}{\pi^{3/2}\Delta\nu_D} \tag{5.9}$$

and for two modes equidistant from line center,

$$x_m \equiv \frac{\sqrt{\ln 2}}{\Delta\nu_D} \Delta\nu_m \tag{5.10}$$

and

$$x \equiv \frac{\sqrt{\ln 2}}{\Delta\nu_D}\,\Delta\nu \quad . \tag{5.11}$$

Using a cavity temperature of 400°K, we solved Eq. (5.8) with an iterative approach, using tabulated values for F (Mitchell and Zemansky, 1971). The results are contained in Table 3.

Table 3. Theoretical Mode-Pulling Corrections

			$P_1(4)$		$P_1(6)$	
ℓ (cm)	L (cm)	$\Delta\nu_m$ (MHz)	β	$\Delta\nu$ (MHz)	β	$\Delta\nu$ (MHz)
15	47.3	317	.117	292	.120	291
15	75	200	.074	188	.076	188
15	87	172	.064	163	.065	162
	$\Delta\nu_D$ (MHz)		364		355	

We observe from these results that, even with no saturation in the laser cavity, mode pulling accounts for a reduction in mode spacing of less than 10% of the passive spacing.

Measuring Mode Spacing From the Fabry-Perot Pattern

With the beam bypassing the Michelson interferometer, the Fabry-Perot pattern displays the two axial laser modes as in Fig. 38. We may use this picture to measure mode spacing by first considering the

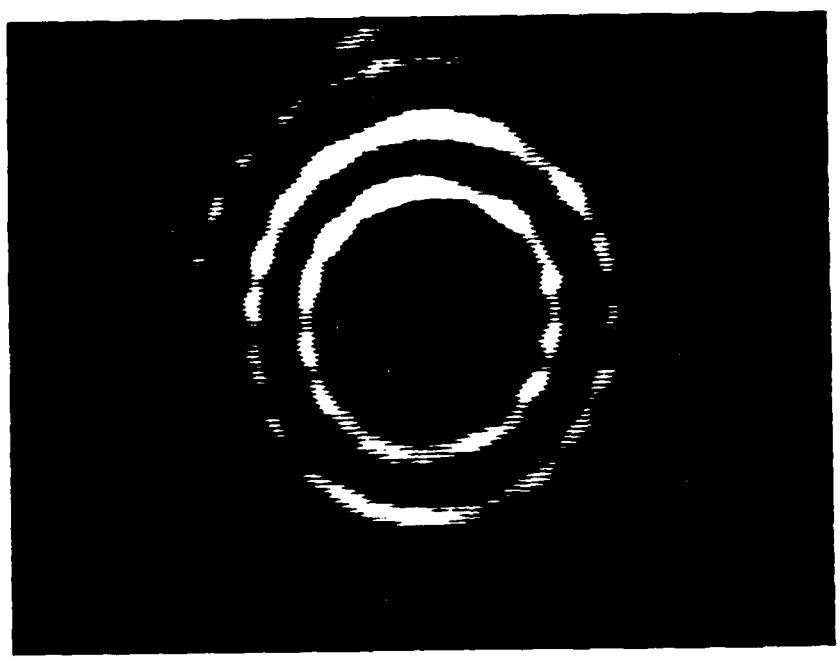

Figure 38. Fabry-Perot Pattern

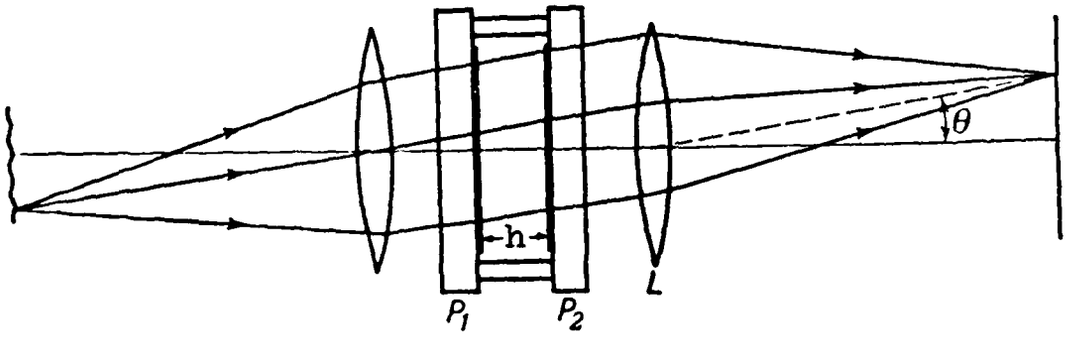

Figure 39. Fabry-Perot Interferometer

arrangement shown in Figure 39. For monochromatic light, a bright ring will appear at an angle θ satisfying

$$\cos\theta = \frac{m\lambda}{2h} \quad , \tag{5.12}$$

where m is an integer. For θ small, this may be written

$$1 - \frac{\theta^2}{2} \cong \frac{m\lambda}{2h} \quad , \tag{5.13}$$

or

$$\theta^2 \cong \frac{\lambda}{h}\left(\frac{2h}{\lambda} - m\right) = \frac{\lambda}{h}\,(m_{max} - m) \quad , \tag{5.14}$$

where here m_{max} is the fractional order at the center of the pattern. The square of the radius for a bright ring in the image plane is just

$$r^2 \cong (D\theta)^2 = D^2\,\frac{\lambda}{h}\,(m_{max} - m) \quad , \tag{5.15}$$

where D is the distance to the image plane. The important thing to note about this result is that the area between successive rings is a constant. Thus, for a pattern containing two frequencies, such as shown in Fig. 38, mode spacing is determined simply by dividing the area between two adjacent modes by the area between two consecutive orders of the same mode, and multiplying by the free spectral range of the interferometer

$$\Delta\nu = \frac{\pi(r_2^2 - r_1^2)}{\pi(r_3^2 - r_1^2)} \Delta\nu_{FSR} \quad . \tag{5.16}$$

Here, r_1, r_2 and r_3 are the radii of the first three rings, respectively.

The plate separation for the Fabry-Perot was 20.7 cm, corresponding to a free spectral range (724.6 MHz) large enough to prevent overlapping of orders.

Since the pattern was not perfectly round, we measured ring diameters both horizontally and vertically, and then averaged the results. These are contained in Table 4. The standard deviation represents the scatter in the measurements.

Table 4. Fabry-Perot Mode-Spacing Measurements

	$P_1(4)$		$P_1(6)$	
L(cm)	$\Delta\nu$(MHz)	σ(MHz)	$\Delta\nu$(MHz)	σ(MHz)
47.3	292	17.1	251	14.5
75	119	15.3	107	16.9
87	130	14.6	123	9.8

There are several reasons that the $P_1(4)$ short-cavity results are much more reliable than the others. First, we took many more pictures to analyze for this configuration. Second, the pictures were

much sharper (had better contrast). Finally, we encountered intermittent oscillation of transverse modes (particularly on the longer cavities but also for the $P_1(6)$ line on the short cavity) which tended to smear out the rings radially.

Measuring Mode Spacing by Beats

We successfully measured the beat frequency between modes by using a Santa Barbara Research Center Model 40742 Ge-Au Infrared Detector and a Tektronix 7L13 Spectrum Analyzer. Figure 40 contains calibration pictures for the spectrum analyzer, while Fig. 41 shows the beats for the $P_1(4)$ line on both the 47.3 cm and 75 cm cavities. Measuring several pictures like Fig. 41 yielded a measured mode spacing of 289.4 MHz for the 47.3 cm cavity and 190.2 MHz for the 75 cm cavity. Similar measurements for the $P_1(6)$ line gave essentially identical results.

Of the three methods for determining mode separation, measuring the beats was most reliable. It is interesting that these results match closely those calculated earlier for an unsaturated laser. Thus, we decided to use the following values for our theoretical calculations:

$$\Delta\nu(47.3\text{ cm}) = 290\text{ MHz} \tag{5.17}$$

$$\Delta\nu(75\text{ cm}) = 190\text{ MHz} \tag{5.18}$$

$$\Delta\nu(87\text{ cm}) = 160\text{ MHz} \tag{5.19}$$

Determining the Saturation Intensity

As mentioned earlier, we sequentially measured power through various-sized holes placed just behind the front window of the gas cell.

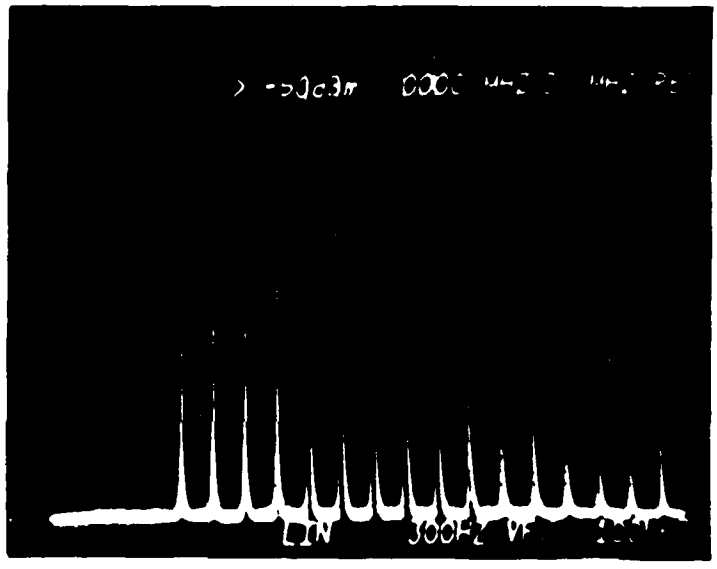

a.

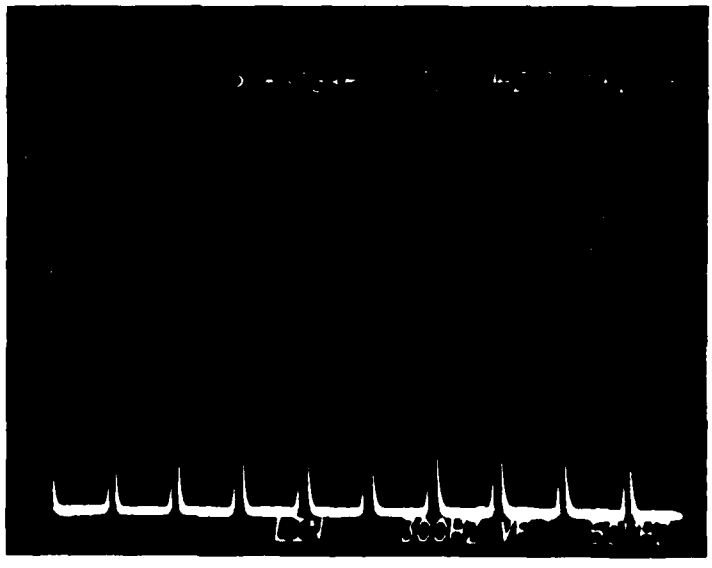

b.

Figure 40. Spectrum Analyzer Calibration

a. 100 MHz/Division
b. 50 MHz/Division

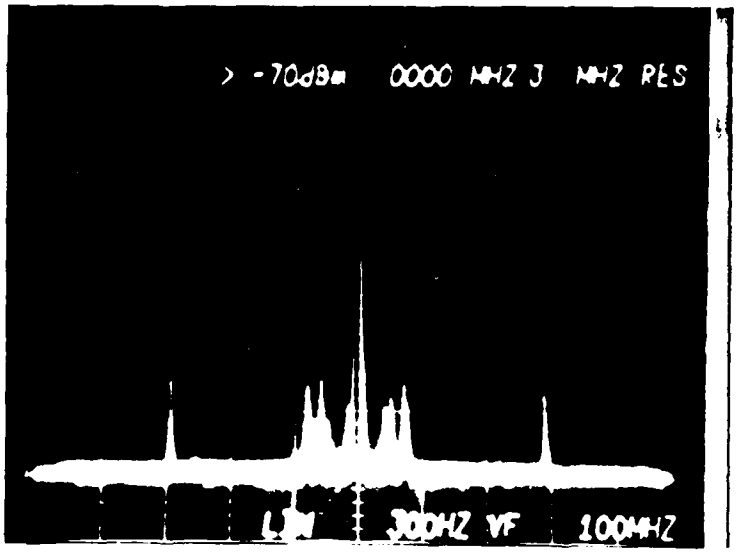

a.

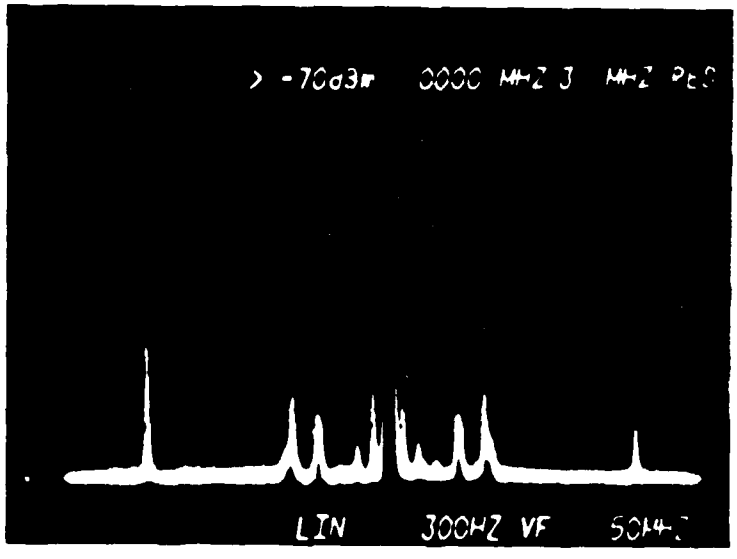

b.

Figure 41. Beat Measurements for $P_1(4)$ Line

a. 47.3 cm Cavity
b. 75 cm Cavity

We thus obtained a picture of the beam intensity profile (Fig. 42), which is Gaussian for TEM_{00}. We calculated a value for saturation intensity from the linear portion of the curve, yielding

$$I(47.3 \text{ cm}) = 17.6 \text{ W/cm}^2 , \tag{5.20}$$

$$I(75 \text{ cm}) = 26.1 \text{ W/cm}^2 , \tag{5.21}$$

where each value represents the total intensity of the beam (including both axial modes).

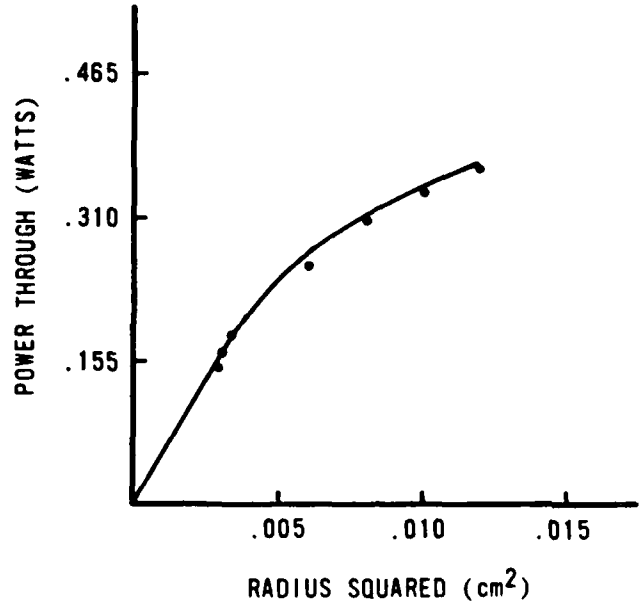

a.

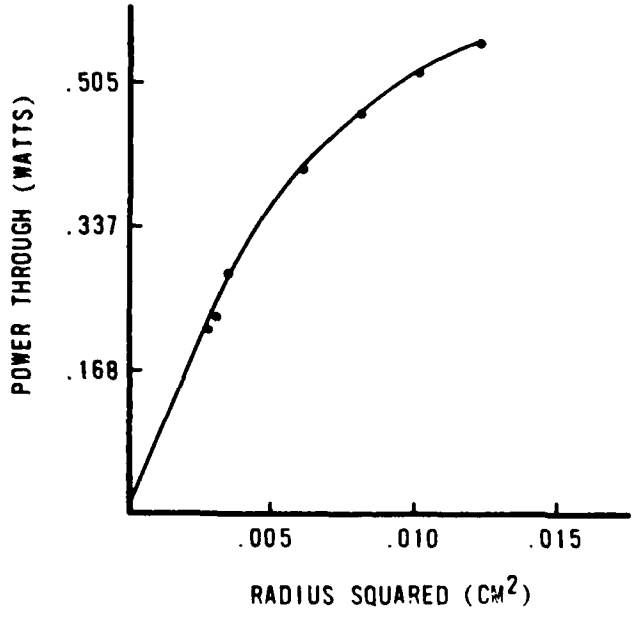

b.

Figure 42. Intensity Profiles for $P_1(4)$ Line

a. 47.3 cm Cavity
b. 75 cm Cavity

CHAPTER 6

DISCUSSION

We see in Figs. 30 through 32 that the experimental data for the $P_1(4)$ line match closely the theoretically-predicted curves for combined Doppler and pressure broadening. It is clear that pressure-broadening effects cannot be neglected, even for pressures as low as one torr. Beyond 1 1/2 torr, the experimental values fall slightly below the theoretical curve for reasons not fully understood. However, the fact that the error bars generally grow as the pressure increases is not surprising since the fringe contrast decreases as the pressure increases (see next section).

The trends are not as well established for the $P_1(6)$ line because of the comparatively small amount of data points. We see, though (especially for the short cavity), that the experimental values follow the combined-broadening curve, with no drop-off at higher pressures.

With the $P_1(4)$ transition partially saturated, the experimental values depart from the unsaturated theoretical curve at noticeably lower pressures than for the unsaturated experimental values. This departure occurs at about .75 torr for the 47.3 cm cavity and .5 torr for the 75 cm cavity (Figs. 36 and 37). We see also that the line broadening rate $\pi\Delta\nu_{II}$ is too high, whereas the gas kinetic rate is too low. However, the intermediate rate $\pi\Delta\nu_{II}/10$ offers a nice fit of the experimental

```
1050  LABEL I
1060  I=I+100
1070  IF I=0 THEN I=100
1080  GOTO 1030
1090  LORG 8
1100  FOR I=-1.E-4 TO 1.E-4 STEP 1.E-4
1110  IF I=0 THEN I=1.E-4
1120  MOVE 0,I
1130  H=I*1.E+4
1140  LABEL H
1150  NEXT I
1160  LORG 3
1170  MOVE -125,1.2E-4
1180  LABEL "(n-1)x10 "
1190  MOVE 0,-1.265E-4
1200  LORG 5
1210  LABEL "  Frequency Difference From Line Center (MHz)"
1220  INPUT "Enter the pressure:",B
1230  INPUT "Enter the Doppler broadened linewidth:",C
1240  INPUT "Enter the pressure broadening per torr:",D
1250  IF W=2 THEN INPUT "Enter the wavelength:",F
1260  S=D*B !Pressure Broadened Linewidth
1270  IF K=1 THEN MOVE 220,1.08E-4
1280  IF K=1 THEN LABEL "Partially-Saturated"
1290  MOVE 220,1.0E-4
1300  LABEL "Index of Refraction for"
1310  MOVE 220,9.2E-5
1320  LABEL "P1(4) Line at",B;"Torr"
1330  MOVE 220,8.4E-5
1340  LABEL "    =";C,"MHz;    =";S;"MHz "
1350  IF W=1 THEN GOTO 1910
1360  IF L=2 THEN PRINT "Type the name of the"
1370  IF L=2 THEN INPUT "absorption file:",N$
1380  IF L=2 THEN ASSIGN @F TO N$
1390  IF L=2 THEN ENTER @F;Z(*)
1400  G=F/(4*(PI)^2)
1410  V=-400
1420  Y=0
1430  FOR X=1 TO 1201 STEP 1
1440  IF ABS(Z(X,1)-V)>2.1 THEN Y=Y+G*5*Z(X,2)*1/(Z(X,1)-V)
1450  IF ABS(Z(X,1)-V)<2.1 THEN Y=Y
1460  NEXT X
1470  MOVE V,Y
1480  PRINT TABXY(1,1),"Do you wish to compute a data file?"
1490  INPUT "Yes (1), No (2)",P
1500  PRINT TABXY(1,1),"                                        "
1510  IF P=1 THEN GOTO 1610
1520  Y=0
1530  FOR X=1 TO 1201 STEP 1
1540  IF ABS(Z(X,1)-V)>2.1 THEN Y=Y+G*5*Z(X,2)*1/(Z(X,1)-V)
1550  IF ABS(Z(X,1)-V)<2.1 THEN Y=Y
1560  NEXT X
```

```
530   MOVE 0,-.75
540   LABEL " Frequency Difference From Line Center (MHz)"
550   INPUT "Enter the pressure:",B
560   INPUT "Enter the Doppler broadened linewidth:",C
570   INPUT "Enter the pressure broadening per torr:",O
580   S=O*B !Pressure Broadened Linewidth
590   IF K=1 THEN MOVE 220,6.81
600   IF K=1 THEN LABEL "Partially-Saturated"
610   MOVE 220,6.54
620   LABEL "Absorption Coefficient"
630   MOVE 220,6.27
640   LABEL "for P1(4) Line at";B;"Torr"
650   MOVE 220,6
660   LABEL "    =";C;"MHz;    =";S;"MHz "
670   MOVE Z(521,1),Z(521,2)
680   FOR T=522 TO 681 STEP 1
690   DRAW Z(T,1),Z(T,2)
700   NEXT T
710   R=0
720   FOR T=1 TO 1201 STEP 1
730   R=R+Z(T,2)
740   NEXT T
750   S=5*R
760   PRINT TABXY(1,1),"The area under the curve          "
770   PRINT "is";S;"units.                               "
780   PRINT "Would you like to run                        "
790   PRINT "a dispersion curve?                          "
800   INPUT "Yes(1), No(2)",U
810   PRINT TABXY(1,1),"                                  "
820   PRINT TABXY(1,2),"                                  "
830   PRINT TABXY(30,2),"                                 "
840   PRINT TABXY(1,3),"                                  "
850   PRINT TABXY(1,4),"                                  "
860   ASSIGN @F TO *
870   IF U=2 THEN GOTO 2220
880   INPUT "After inserting fresh paper, enter a 1.",W
890   GCLEAR
900   !Dispersion Curve
910   PRINT TABXY(1,1),"Have you computed                 "
920   PRINT TABXY(1,2),"a dispersion curve?               "
930   INPUT "Yes(1), No(2)",W
940   PRINT TABXY(1,1),"                                  "
950   PRINT TABXY(1,2),"                                  "
960   WINDOW -480,480,-1.5E-4,1.6E-4
970   CLIP -420,420,-1.2E-4,1.2E-4
980   AXES 50,5.E-5,0,0
990   CLIP OFF
1000  CSIZE 3
1010  LORG 6
1020  I=-400
1030  IF I>400 THEN GOTO 1090
1040  MOVE I,-3.5E-6
```

```
10    !Program Title: ABDIS4
20    !Program Function A: Anomalous Dispersion Computation
30    !                    for P1(4) Line
40    !Program Function B: Absorption and Dispersion Plots
50    !                    for P1(4) Line
60    GINIT
70    PLOTTER IS 705,"HPGL"
80    GRAPHICS ON
90    INPUT "Are we saturated (1) or unsaturated (2)?",K
100   PRINT "Insert data disk                                "
110   PRINT "in right-hand drive.                            "
120   INPUT "Enter a 1.",J
130   PRINT TABXY(1,1),"                                     "
140   PRINT TABXY(1,2),"                                     "
150   OPTION BASE 1
160   DIM Z(1205,2)
170   DIM E(165,2)
180   MASS STORAGE IS ":HP82901,700,1"
190   PRINT TABXY(1,1),"Do you want absorption               "
200   PRINT TABXY(1,2),"or dispersion?                       "
210   INPUT "Absorption (1), Dispersion (2)",L
220   PRINT TABXY(1,1),"                                     "
230   PRINT TABXY(1,2),"                                     "
240   IF L=2 THEN GOTO 910
250   !Absorption Curve
260   PRINT TABXY(1,2),"                                     "
270   PRINT TABXY(1,1),"Type the name of the file            "
280   PRINT "to be accessed:                                 "
290   INPUT N$
300   PRINT TABXY(1,1),"                                     "
310   PRINT TABXY(1,2),"                                     "
320   ASSIGN @F TO N$
330   ENTER @F;Z(*)
340   WINDOW -480,480,-1.5,8.8
350   CLIP -420,420,-.001,7.5
360   AXES 50,1,0,0
370   CLIP OFF
380   CSIZE 3
390   LORG 6
400   I=-400
410   IF I>400 THEN GOTO 470
420   MOVE I,0
430   LABEL I
440   I=I+100
450   IF I=0 THEN I=100
460   GOTO 410
470   LORG 8
480   FOR I=1 TO 7 STEP 2
490   MOVE 0,I
500   LABEL I
510   NEXT I
520   LORG 5
```

```
530   PRINT "Insert data disk in right-hand drive.          "
540   INPUT "Enter a 1.",J
550   PRINT TABXY(1,3),"                                    "
560   PRINT "Type the name of the file you wish to store:   "
570   INPUT U$
580   MASS STORAGE IS ":HP82901,700,1"
590   CREATE BDAT U$,1210,16
600   ASSIGN @F TO U$
610   OUTPUT @F;E(*)
620   S=(2*M-E(601,2))*5
630   MASS STORAGE IS ":HP82901,700,0"
640   END
```

```
10    !Program Title: ABSAT
20    !Program Function: Saturated Absorption Curve
30    !                  Computation for Impure Broadening
40    GINIT
50    OPTION BASE 1
60    DIM Z(1205,6)
70    DIM E(1205,2)
80    PRINT "Enter the Doppler broadened                    "
90    PRINT "absorption coefficient per torr:               "
100   INPUT A
110   PRINT TABXY(1,1),"                                    "
120   PRINT TABXY(1,2),"                                    "
130   INPUT "Enter the pressure:",B
140   INPUT "Enter the Doppler broadening:",C
150   INPUT "Enter the pressure broadening per torr:",D
160   F=A*B                    !Old Ko
170   G=D*B           !Total Pressure Broadening
180   R=PI*G*1.E+6
190   H=SQR(LOG(2))
200   L=-95
210   O=95
220   I=26.09
230   T=1
240   FOR X=-3000 TO 3000 STEP 5
250   N=5.632E+13*B*EXP((-1)*(.0053*X)^2)
260   Z(T,1)=X
270   Z(T,2)=N
280   W=(1/(1+(2*(X-L)/G)^2)+1/(1+(2*(X-O)/G)^2))
290   Z(T,3)=F*EXP((-1)*(2*X*H/C)^2)/N*W
300   Z(T,4)=N/(2.286+R/(1.33E+19*Z(T,3)*I))
310   Z(T,5)=Z(T,2)-Z(T,4)
320   Z(T,6)=F*Z(T,5)/Z(T,2)*(1-9*Z(T,4)/(7*Z(T,5)))
330   T=T+1
340   NEXT X
350   V=-3000
360   M=0
370   T=1
380   Y=0
390   Q=2/(PI*G)
400   FOR X=-3000 TO 3000 STEP 5
410   P=Q*Z(T,6)
420   Y=Y+5*P*EXP((-1)*(2*X*H/C)^2)/(1+(2*(V-X)/(B*D))^2)
430   NEXT X
440   E(T,1)=V
450   E(T,2)=Y
460   E(1202-T,1)=-V
470   E(1202-T,2)=Y
480   T=T+1
490   M=M+Y
500   V=V+5
510   IF V>0 THEN GOTO 530
520   GOTO 380
```

```
10     !Program Title: ABUNSAT
20     !Program Function: Unsaturated Absorption Curve
30     !                  Computation for Impure Broadening
40     GINIT
50     OPTION BASE 1
60     DIM Z(1205,2)
70     PRINT "Enter the Doppler broadened                    "
80     PRINT "absorption coefficient per torr:               "
90     INPUT A
100    PRINT TABXY(1,1),"                                    "
110    PRINT TABXY(1,2),"                                    "
120    INPUT "Enter the pressure:",B
130    INPUT "Enter the Doppler broadening:",C
140    INPUT "Enter the pressure broadening per torr:",D
150    P=2*A/(PI*D)
160    M=SQR(LOG(2))
170    V=-3000
180    R=0
190    T=1
200    Y=0
210    FOR X=-3000 TO 3000 STEP 5
220    IF ABS(V-X)>3000 THEN GOTO 240
230    Y=Y+5*P*EXP((-1)*(2*(V-X)*M/C)^2)/(1+(2*X/(B*D)))^2)
240    NEXT X
250    Z(T,1)=V
260    Z(T,2)=Y
270    Z(1202-T,1)=-V
280    Z(1202-T,2)=Y
290    T=T+1
300    R=R+Y
310    V=V+5
320    IF V>0 THEN GOTO 340
330    GOTO 200
340    PRINT "Insert data disk in right-hand drive.          "
350    INPUT "Enter a 1.",J
360    PRINT TABXY(1,3),"                                    "
370    PRINT "Type the name of the file you wish to store    "
380    INPUT N$
390    MASS STORAGE IS ":HP82901,700,1"
400    CREATE BDAT N$,1210,16
410    ASSIGN @F TO N$
420    OUTPUT @F;Z(*)
430    S=(2*R-Z(601,2))*5
440    MASS STORAGE IS ":HP82901,700,0"
450    END
```

APPENDIX A

COMPUTER PRINTOUT

Contained here are the computer programs used to generate absorption and dispersion profiles, from which the theoretical curves found in Figs. 30 - 37 were obtained.

CONCLUSION

A crossed interferometer technique has been successfully used to measure the anomalous dispersion of two ground-state HF transitions in absorption. Results were in close agreement with theoretically predicted values. The method also gave meaningful results when the transition was partially saturated.

A distinct advantage of the technique over the many other attempts at measuring anomalous dispersion is the spatial resolution of the axial modes by a Fabry-Perot interferometer. The implication is that the entire anomalous dispersion curve can be sampled at the same time, limited only by the number of axial modes. It is realistic to expect the technique to successfully work for a saturated gain medium. In principle, the technique offers the potential for measuring the time-evolution of the anomalous dispersion in a pulsed laser.

Our theory used a constant value for the intensity distribution of the saturating beam, which, of course, is only a crude approximation, since at best, the laser beam had a Gaussian intensity profile. Consequently, the medium saturated spatially in a nonuniform fashion, thereby complicating the picture.

Assuming throughout the experimental runs that the HF gas was pure was probably reasonable since, before using the lecture-grade gas, we froze it with liquid nitrogen and pumped on the system to remove any impurities. Also, even though HF is highly polymerized at temperatures below 70°C (Meredith, 1972), the presence of dimers was insignificant for the low pressures at which we operated.

Finally, the measurement technique itself was subjective, and, hence, open to error. This is why three of us read data and averaged the results. An improvement of any of the previously mentioned limitations would serve to eliminate some of this subjectivity. We considered, at one point in the experiment, making a digital readout of the data points, but the large volume of data to be read made this an impractical option.

difficult to eliminate and made it impossible to obtain meaningful data. So we removed the lens and proceeded with less intensity.

Another limitation was the simple fact that one leg of the Michelson interferometer contained an absorbing cell. At higher gas pressures, the intensities in the two interferometer legs were unequal, and so the fringes had less contrast. A compensator plate inserted in the other leg improved contrast, but diminished overall intensity to an unacceptable level. Thus, we accomplished all readings without the plate. The larger error bars at higher pressures reflect this increasing loss of contrast. Since absorption is proportional to the product of pressure and length of the absorbing layer, one way to make more accurate readings at higher pressures would be to shorten the cell.

Ensuring equal intensity for both axial modes was another area subject to error. The theoretical curves (Figs. 30-35) were computed based on the assumption that the modes were equidistant from line center. Practically, we applied pressure to the grating mount until two modes of equal intensity appeared on the television monitor. This was a subjective evaluation and could likely have been improved upon by using detectors. However, the utility of a more elaborate arrangement is questionable since axial modes generally fall on a fairly linear portion of the refractive index curve.

Transverse modes other than TEM_{00} were evident at times, particularly for the two longer cavities. While not terribly bothersome, they tended to exaggerate the mode width and interfered with an accurate determination of the high-intensity spot of a fringe.

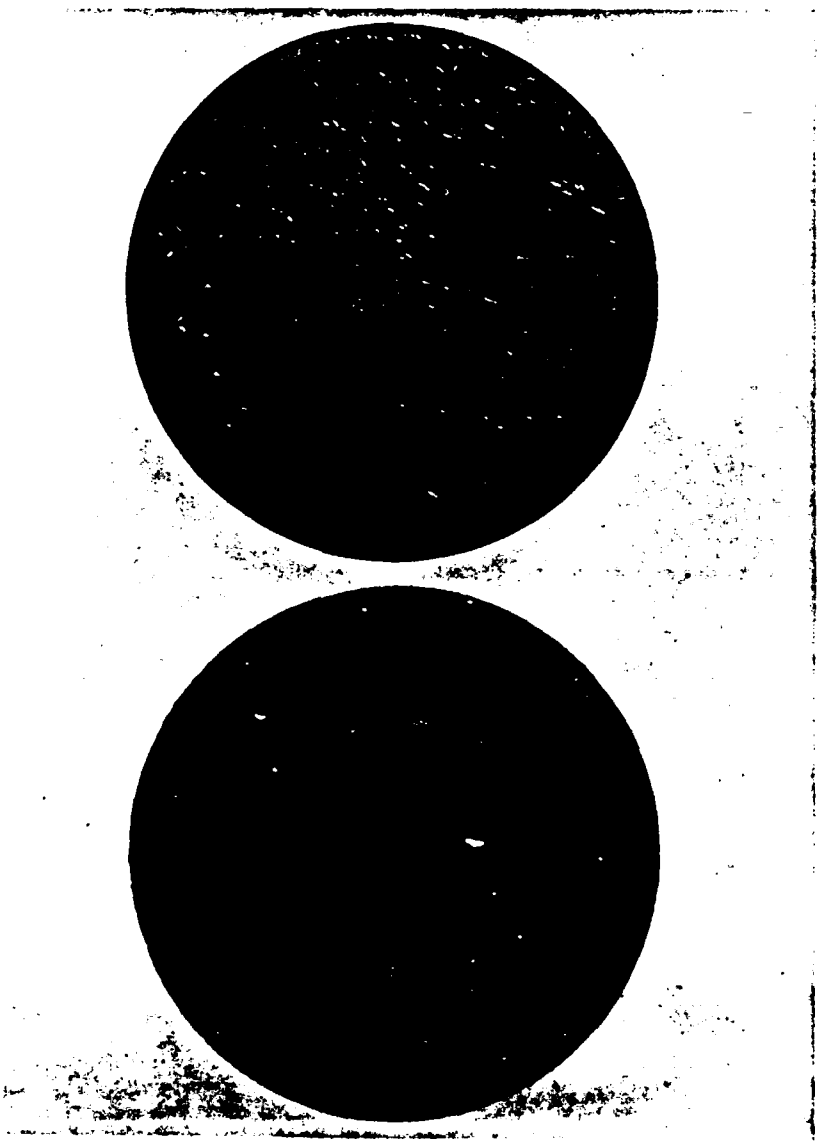

Figure 43. Improperly Coated Fabry-Perot Plates

This number agrees well with the standard deviations of our measurements. The way to improve resolution, of course, is to use larger plates. For example, standard two-inch plates would reduce the above figure by a factor of two. However, large pieces of calcium fluoride are exceedingly difficult to coat, as evidenced in Fig. 43. We had ordered these two-inch plates from a company that specializes in coating substrates, but the coatings were detached from the plates on their arrival.

Optical aberrations proved to be another obstacle to accurate measurements, and are particularly evident in Fig. 38, where we notice that the Fabry-Perot pattern is not perfectly round, as it should be. The slight oval shape is possibly due to strain in one or both of the interferometer plates. The possible range of error due to the lack of roundness is just the difference between the horizontal and vertical axis measurements. This difference corresponds to approximately 35 MHz. The mode-spacing measurements (Table 4) arising from the pattern are rightly suspect, and consequently were not considered in determining the actual mode spacing.

Other aberrations occurred as well. At one point during the nonsaturated measurements, we inserted a CaF_2 lens just prior to the Fabry-Perot interferometer to reduce the divergence of the light entering the interferometer (it served as the output lens of a telescope). The lens acted to illuminate a smaller portion of the pattern and offer more intensity to the portion illuminated. It also, however, created aberrations (seen in the crossed interferometer pattern) that were

$$\Delta\nu_{res} = \frac{\lambda\nu}{2\mathcal{F}L} = \frac{c}{2\mathcal{F}L} \quad , \tag{6.3}$$

and, ignoring for now the diffraction limit, the best resolution we could expect with our 20.7 cm interferometer would be just under 5 MHz.

Now, the angular separation of adjacent orders near the center of a Fabry-Perot pattern is on the order of $\sqrt{\lambda/L}$. Following Rayleigh's criterion, the minimum angular separation that can be resolved through a circular diffracting aperture is

$$.61\,\frac{\lambda}{a} \cong \frac{\lambda}{D} \quad , \tag{6.4}$$

where a and D are, respectively, the radius and diameter of the diffracting aperture. We thus have an imposed upper bound on finesse

$$\mathcal{F} \leqslant \frac{\sqrt{\lambda/L}}{\lambda/D} = \frac{D}{\sqrt{\lambda L}} \quad , \tag{6.5}$$

even for perfectly reflecting mirrors. If we assume that the entire one-inch diameter of the plates is filled with light, then for our interferometer,

$$\mathcal{F} \leqslant \frac{2.5}{\sqrt{2.7\text{x}10^{-4}(20.7)}} = 33.4 \tag{6.6}$$

and

$$\Delta\nu_{res} \leqslant \frac{3\text{x}10^{10}}{2(33.4)(20.7)} = 21.7 \text{ MHz.} \tag{6.7}$$

data. Hence, at the low pressures and saturation levels at which we are operating, for which the model appears to be valid, the experimentally-determined state-altering, velocity-changing collision rate is seen to be $K = \pi\Delta\nu_H/10 = 11\text{x}10^6/\text{sec-torr}$.

Experimental Limitations

There were a number of limitations that kept us from realizing the best accuracy possible. These are briefly discussed here.

Probably the most important physical limitation was the small-diameter plates of the Fabry-Perot interferometer (only a 2 cm open aperture). Although we endeavored to fill the entire plate area with light, the physical size imposed a diffraction limit on the resolution attainable with the instrument.

For infinitely large and perfectly flat plates, the finesse is limited only by the reflectance (R) of the mirror surfaces

$$\mathcal{F} = \frac{\pi\sqrt{R}}{1 - R} , \tag{6.1}$$

which, for R = .98, is about 156. Now, the finesse relates to the resolution ($\mathcal{R}$) by

$$\mathcal{R} = \frac{\nu}{\Delta\nu_{res}} = \frac{2L}{\lambda}\ \mathcal{F} , \tag{6.2}$$

where $\Delta\nu_{res}$ is the minimum resolvable frequency difference and L is the Fabry-Perot mirror separation. So,

```
1570  DRAW V,Y
1580  V=V+5
1590  IF V)400 THEN GOTO 2120
1600  GOTO 1520
1610  T=1
1620  Y=0
1630  FOR X=1 TO 1201 STEP 1
1640  IF ABS(Z(X,1)-V))2.1 THEN Y=Y+G*5*Z(X,2)*1/(Z(X,1)-V)
1650  IF ABS(Z(X,1)-V)(2.1 THEN Y=Y
1660  NEXT X
1670  E(T,1)=V
1680  E(T,2)=Y
1690  DRAW V,Y
1700  IF T=52 THEN PRINT V
1710  IF T=52 THEN PRINT Y
1720  IF T=62 THEN PRINT V       !Index of Refraction Values
1730  IF T=62 THEN PRINT Y       !for the Three Cavities
1740  IF T=65 THEN PRINT V
1750  IF T=65 THEN PRINT Y
1760  T=T+1
1770  V=V+5
1780  IF V)400 THEN GOTO 1800
1790  GOTO 1620
1800  PRINT TABXY(1,1),"Insure data disk                    "
1810  PRINT TABXY(1,2),"is in right-hand drive.             "
1820  INPUT "Enter a 1.",0
1830  PRINT TABXY(1,2),"                                    "
1840  PRINT TABXY(1,1),"Type the name of the file           "
1850  PRINT TABXY(1,2),"you wish to store.                  "
1860  INPUT N$
1870  CREATE BDAT N$,170,16
1880  ASSIGN @F TO N$
1890  OUTPUT @F;E(*)
1900  GOTO 2120
1910  PRINT TABXY(1,1),"Insure data disk                    "
1920  PRINT TABXY(1,2),"is in right-hand drive.             "
1930  INPUT "Enter a 1.",0
1940  PRINT TABXY(1,2),"                                    "
1950  PRINT TABXY(1,1),"Type the name of the file           "
1960  PRINT TABXY(1,2),"to be accessed                      "
1970  INPUT N$
1980  PRINT TABXY(1,1),"                                    "
1990  PRINT TABXY(1,2),"                                    "
2000  ASSIGN @F TO N$
2010  ENTER @F;E(*)
2020  MOVE E(1,1),E(1,2)
2030  FOR T=1 TO 161 STEP 1
2040  DRAW E(T,1),E(T,2)
2050  IF T=52 THEN PRINT TABXY(1,7),E(T,1)
2060  IF T=52 THEN PRINT E(T,2)
2070  IF T=62 THEN PRINT E(T,1) !Index of Refraction Values
2080  IF T=62 THEN PRINT E(T,2) !for the Three Cavities
```

```
2090  IF T=65 THEN PRINT E(T,1)
2100  IF T=65 THEN PRINT E(T,2)
2110  NEXT T
2120  PRINT TABXY(1,1),"Do you wish to run                    "
2130  PRINT TABXY(1,2),"an absorption curve?                  "
2140  INPUT "Yes (1), No (2)",M
2150  PRINT TABXY(1,1),"                                      "
2160  PRINT TABXY(1,2),"                                      "
2170  IF M=1 THEN PRINT TABXY(1,1),"After inserting fresh     "
2180  IF M=1 THEN PRINT TABXY(1,2),"paper, enter a 1          "
2190  IF M=1 THEN INPUT N
2200  IF M=1 THEN GCLEAR
2210  IF M=1 THEN GOTO 250
2220  MASS STORAGE IS ":HP82901,700,0"
2230  END
```

```
10    !Program Title: DISPURE4
20    !Program Function: Dispersion Curve Computation & Plot
30    !                  for P1(4) Line with Pure Broadening
40    GINIT
50    PLOTTER IS 705,"HPGL"
60    GRAPHICS ON
70    WINDOW -480,480,-1.5E-4,1.6E-4
80    CLIP -420,420,-1.2E-4,1.2E-4
90    AXES 50,5.E-5,0,0
100   CLIP OFF
110   CSIZE 3
120   LORG 6
130   I=-400
140   IF I>400 THEN GOTO 200
150   MOVE I,-3.5E-6
160   LABEL I
170   I=I+100
180   IF I=0 THEN I=100
190   GOTO 140
200   LORG 8
210   FOR I=-1.E-4 TO 1.E-4 STEP 1.E-4
220   IF I=0 THEN I=1.E-4
230   MOVE 0,I
240   H=I*1.E+4
250   LABEL H
260   NEXT I
270   LORG 3
280   MOVE -125,1.2E-4
290   LABEL "(n-1)x10 "
300   MOVE 0,-1.265E-4
310   LORG 5
320   LABEL "  Frequency Difference From Line Center (MHz)"
330   PRINT "Are we Doppler or pressure broadened?          "
340   INPUT "Doppler (1), Pressure (2)",S
350   PRINT TABXY(1,1),"                                    "
360   IF S=1 THEN M=3.018E+6
370   IF S=2 THEN M=2.045E+6
380   INPUT "Enter the A Coefficient:",A
390   INPUT "Enter the pressure:",B
400   IF S=1 THEN INPUT "Enter the Doppler linewidth:",C
410   IF S=2 THEN INPUT "Enter the pressure linewidth.",C
420   INPUT "Enter the upper J:",D
430   INPUT "Enter the lower J:",H
440   INPUT "Enter the wavelength:",F
450   MOVE 220,1.E-4
460   IF S=1 THEN GOTO 490
470   IF S=2 THEN LABEL "Pressure Broadened Index"
480   GOTO 500
490   LABEL "Doppler Broadened Index"
500   MOVE 220,9.2E-5
510   LABEL "of Refraction for P1(4)"
520   MOVE 220,8.4E-5
```

```
530   LABEL "at";B;"Torr"
540   G=M*B*A*(2*D+1)*(F^3)*EXP(-.10144*H*(H+1))/C
550   IF S=1 THEN GOTO 780
560   V=-400
570   Y=0
580   FOR X=-1500 TO 1500 STEP 5
590   IF ABS(X-V))2.1 THEN Y=Y+G*5/(1+4*(X)^2/C^2)*1/(X-V)
600   IF ABS(X-V)(2.1 THEN Y=Y
610   NEXT X
620   MOVE V,Y
630   Y=0
640   FOR X=-1500 TO 1500 STEP 5
650   IF ABS(X-V))2.1 THEN Y=Y+G*5/(1+4*(X)^2/C^2)*1/(X-V)
660   IF ABS(X-V)(2.1 THEN Y=Y
670   NEXT X
680   DRAW V,Y
690   IF V=-145 THEN PRINT V
700   IF V=-145 THEN PRINT Y
710   IF V=-95 THEN PRINT V
720   IF V=-95 THEN PRINT Y
730   IF V=-80 THEN PRINT V
740   IF V=-80 THEN PRINT Y
750   V=V+5
760   IF V)400 THEN GOTO 1020
770   GOTO 630
780   V=-400
790   Y=0
800   FOR X=-400 TO 400 STEP 5
810   W=EXP((-1)*(2*X*SQR(LOG(2))/C)^2)
820   IF ABS(X-V))2.1 THEN Y=Y+G*5*W*1/(X-V)
830   IF ABS(X-V)(2.1 THEN Y=Y
840   NEXT X
850   MOVE V,Y
860   Y=0
870   FOR X=-400 TO 400 STEP 5
880   W=EXP((-1)*(2*X*SQR(LOG(2))/C)^2)
890   IF ABS(X-V))2.1 THEN Y=Y+G*5*W*1/(X-V)
900   IF ABS(X-V)(2.1 THEN Y=Y
910   NEXT X
920   DRAW V,Y
930   IF V=-145 THEN PRINT V
940   IF V=-145 THEN PRINT Y
950   IF V=-95 THEN PRINT V
960   IF V=-95 THEN PRINT Y
970   IF V=-80 THEN PRINT V
980   IF V=-80 THEN PRINT Y
990   V=V+5
1000  IF V)400 THEN GOTO 1020
1010  GOTO 860
1020  END
```

APPENDIX B

FABRY-PEROT INTERFEROMETER MOUNT

Figure 44 is a close-up view of the Fabry-Perot mount, in which details can be seen. Figure 45 is a copy of the blueprint used in its construction. This mount was designed by Carl Pelander of the Joint Institute for Laboratory Astrophysics.

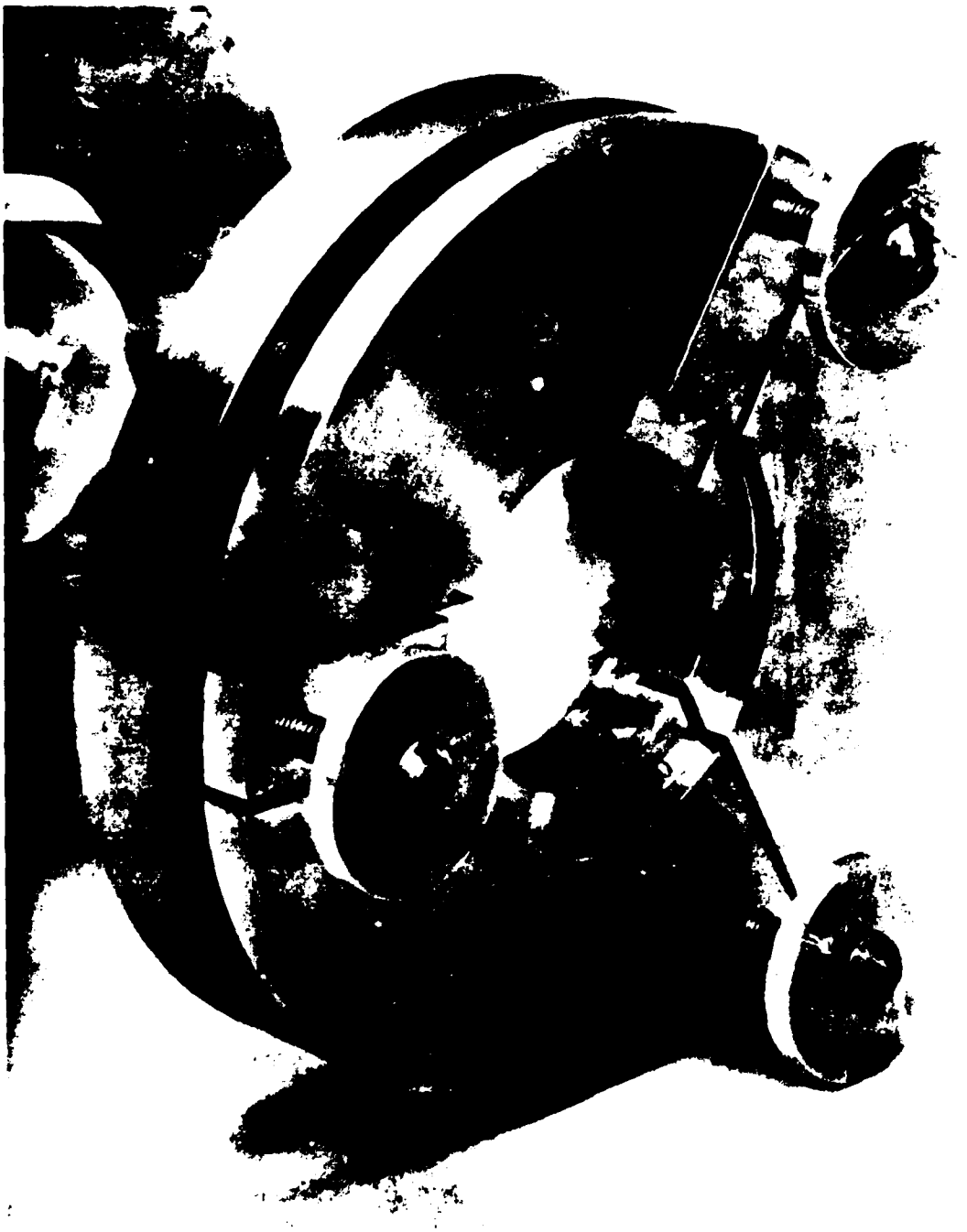

Figure 44. Close-Up Photograph of Fabry-Perot Mount

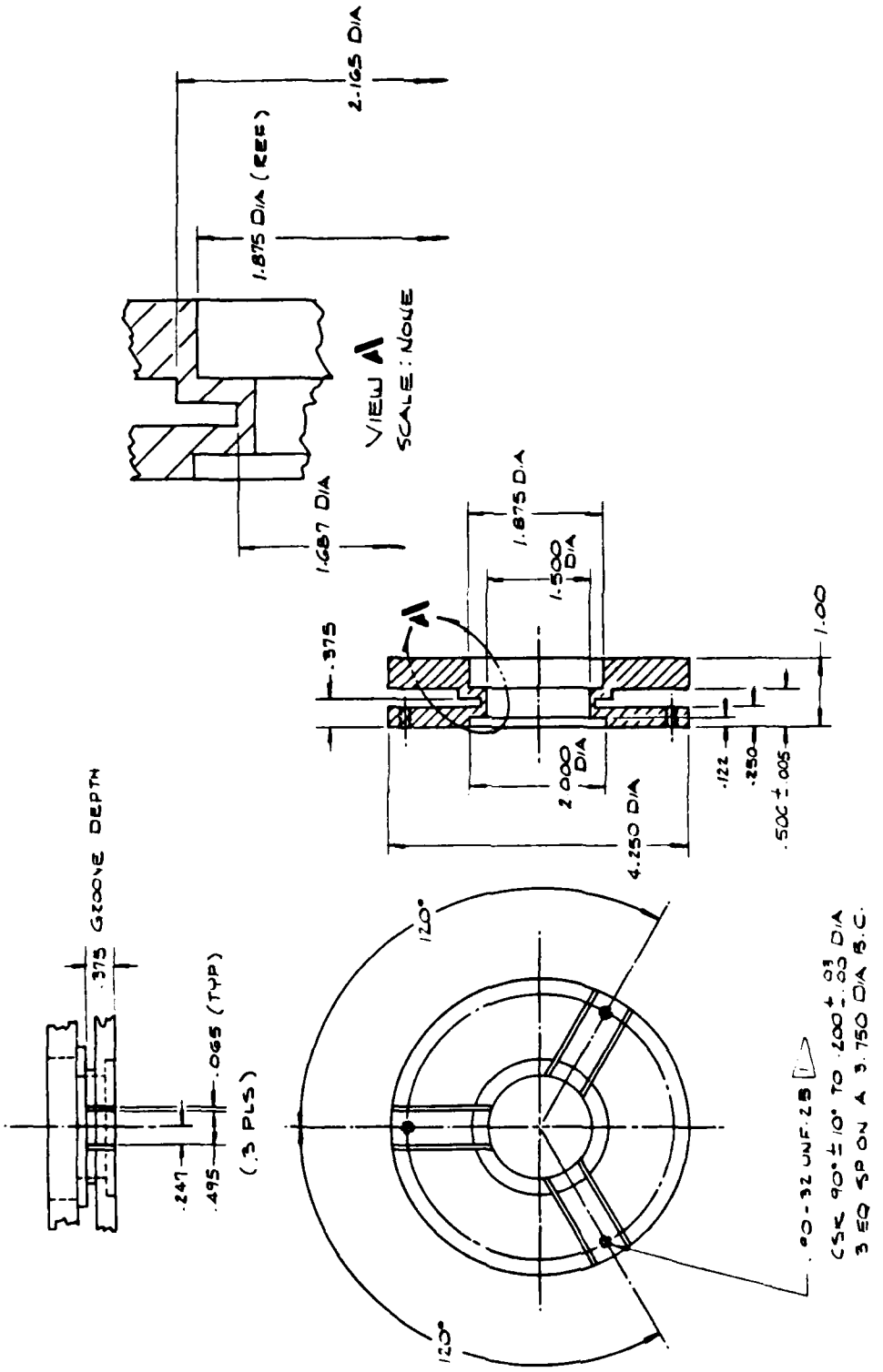

Figure 45. Blueprint of Fabry-Perot Mount

APPENDIX C

TABULAR DATA

Following are the experimental data from which Figures 30 through 37 were constructed. Each data point represents an average of all measurements for the same cavity and pressure, and typically includes more than 20 samplings performed at different times. The standard deviation, then, indicates not only the scatter in the subjective measurement process, but also provides a measure of the experimental reproducibility.

Non-Saturation Results for $P_1(4)$ Line

L(cm)	p(torr)	%Shift	$\Delta(n-1)x10^5$	$\sigma x10^5$
47	.30	.119	2.38	.44
47	.50	.130	2.60	1.54
47	.75	.302	6.04	1.10
47	1.00	.336	6.72	1.06
47	1.10	.324	6.48	.80
47	1.45	.402	8.04	.70
47	1.50	.441	8.82	.94
47	1.55	.427	8.54	.84
47	2.00	.464	9.28	1.06
75	.30	.065	1.30	.40
75	.40	.085	1.70	.32
75	.50	.169	3.38	1.42
75	.58	.126	2.52	.88
75	.80	.188	3.76	.88
75	1.00	.228	4.56	.84
75	1.50	.329	6.58	.60
75	2.00	.325	6.50	1.14
75	2.50	.361	7.22	1.06
75	3.00	.380	7.60	2.24
87	1.00	.207	4.14	1.04
87	1.50	.343	6.86	1.36
87	2.00	.305	6.10	.70

Non-Saturation Results for $P_1(6)$ Line

L(cm)	p(torr)	%Shift	$\Delta(n-1)x10^5$	$\sigma x10^5$
47	2.40	.180	3.60	1.50
47	2.60	.153	3.06	.46
47	3.00	.176	3.52	.72
47	4.00	.243	4.86	.70
47	5.00	.270	5.40	.64
75	.50	.056	1.15	-
87	2.40	.100	2.00	.14
87	3.00	.134	2.68	.42

Saturation Results for $P_1(4)$ Line

L(cm)	p(torr)	%Shift	$\Delta(n-1)x10^5$	$\sigma x10^5$
47	.10	.045	.91	.52
47	.30	.112	2.24	.90
47	.50	.169	3.38	1.38
47	.75	.194	3.88	.94
47	1.00	.240	4.80	.94
47	1.25	.259	5.18	.81
47	1.50	.284	5.69	1.00
75	.10	.046	.92	.40
75	.14	.056	1.12	.24
75	.30	.101	2.02	.46
75	.50	.090	1.80	.38
75	.75	.115	2.30	.74
75	1.00	.141	2.82	.46
75	1.25	.161	3.22	.50
75	1.50	.175	3.50	.42
75	1.75	.189	3.78	.86
75	2.00	.210	4.20	1.04

REFERENCES

Anderson, P. W., "Pressure Broadening in the Microwave and Infra-Red Regions," Phys. Rev. 76:647-661 (1949).

Benedict, William S., Robert Herman, Gordon E. Moore, and Shirleigh Silverman, "The Strengths, Widths, and Shapes of Infrared Lines; I. General Considerations," Can. J. Phys. 34:830-849 (1956a).

Benedict, William S., Robert Herman, Gordon E. Moore, and Shirleigh Silverman, "The Strengths, Widths, and Shapes of Infrared Lines; The HCl Fundamental," Can. J. Phys. 34:850-875 (1956b).

Bennett, Jr., W. R., "Gaseous Optical Masers," Appl. Opt. Supp. 1:24-61 (1962a).

Bennett, Jr., W. R., "Hole Burning Effects in a He-Ne Optical Maser," Phys. Rev. 126:580-593 (April 1962b).

Booth, D. J., and G. J. Troup, "Wavefront Distortion Caused by Saturated Anamalous Dispersion in Laser Amplifiers," Australian Defence Scientific Service Report 347 (October 1969).

Born, Max, and Emil Wolf, Principles of Optics, Oxford: Pergamon Press (1975).

Casperson, Lee, and Amnon Yariv, "Longitudinal Modes in a High-Gain Laser," App. Phys. Lett. 17:259-261 (September 1970).

Chodzko, R. A., C. P. Wang, and H. Mirels, "Effect of Anomalous Dispersion on CW Chemical Laser Performance," presented at Tri-Service Chemical Laser Conference, Silver Spring, Maryland (May 1978).

Close, Donald H., "Strong Field Saturation Effects in Laser Media," Phys. Rev. 153:360-371 (January 1967).

Drummond, David L., "Refractive Index of HF From 2.5 μm to 2.9 μm," Appl. Opt. 21:4331-4334 (December 1982).

Emanuel, George, "Computer-Generated A Coefficients for Hydrogen Fluoride," Aerospace Corporation, unpublished (1971).

Emanuel, G., W. D. Adams, and E. B. Turner, "RESALE-1: A Chemical Laser Computer Program," Aerospace Corporation Report TR-0172(2776)-1 (July 1971).

Gross, R. W. F., R. A. Chodzko, E. B. Turner, and J. G. Coffer, "Measurements of the Anomalous Dispersion of HF in Absorption," Aerospace Corporation Report SAMSO-TR-79-44 (June 1979).

Gross, R. W. F., and J. G. Coffer, "Saturation Processes in Doppler-Broadened HF Vibrational Transitions," Aerospace Corporation Report SD-TR-83-64 (September 1983).

Herzberg, Gerhard, Molecular Spectra and Molecular Structure, I. Spectra of Diatomic Molecules, New York: Van Nostrand Reinhold Company (1950).

Hough, J. J. T., "Lorentz Broadening in the Modeling of the HF Chemical Laser," Appl. Opt. 16:2297-2307 (August 1977).

Jackson, John D., Classical Electrodynamics, 2nd Ed., New York: John Wiley and Sons, Inc. (1975).

Ladenburg, Rudolf, "Untersuchungen Über die Anomale Dispersion Angeregter Gase," Zeitschrift für Physik 48: 15-25 (1928).

Lengyel, Bela A., Lasers, 2nd Ed., New York: John Wiley and Sons, Inc. (1971).

Lorentz, H. A., "The Width of Spectral Lines," Proc. Amst. Acad., 18:134-150 (1915).

Marion, Jerry B., Classical Electromagnetic Radiation, New York: Academic Press (1965).

Meredith, R. E., "Strengths and Widths in the First Overtone Band of Hydrogen Fluoride," J. Quant. Spect. and Rad. Trans. 12: 485-503 (1972).

Meredith, R. E., T. S. Chang, F. G. Smith, and D. R. Woods, "Investigations in Support of High Energy Laser Technology," Science Applications, Inc., Report SAI-73-004-AA(I), Volume 1 (1973).

Meredith, Robert E., and Frederick G. Smith, "Computation of Electric Dipole Matrix Elements for Hydrogen Fluoride," J. Quant. Spect. and Rad. Trans. 13:89-114 (1973).

Mirels, Harold, "Inhomogeneous Broadening Effects in CW Chemical Lasers," AIAA Journ. 17:478-489 (May 1979).

Mitchell, Allan C. G., and Mark W. Zemansky, Resonance Radiation and Excited Atoms, London: Cambridge at the University Press (1971).

Siegman, A. E., An Introduction to Lasers and Masers, New York: McGraw-Hill Book Company (1971).

Tsao, C. J., and B. Curnette, "Line-Widths of Pressure-Broadened Spectral Lines," J. Quant. Spect. and Rad. Trans. 2:41-91 (1963).

Wang, C. P., "Frequency Stability of a CW HF Chemical Laser," J. Appl. Phys. 47:221-223 (1976).

Wang, C. P., and R. L. Varwig, "Competition of Longitudinal and Transverse Modes in a CW HF Chemical Laser," Aerospace Corporation Report SD-TR-79-16 (December 1979a).

Wang, C. P., and R. L. Varwig, "Frequency Stabilization of HF Lasers by Means of Beat Signals and Anomalous Dispersion," J. Appl. Phys. 50:3838-3840 (1978b).

Wang, C. P., and R. L. Varwig, "Direct Measurement of Anomalous Dispersion by Beam Steering and a Wavefront Sensor," Aerospace Corporation Report ATR-81(8408)-1 (May 1981).

END

FILMED

8-85

DTIC